

NUMERICAL SIMULATION OF MULTIPHASE DYNAMICS IN DROPLET MICROFLUIDICS

Mesuli Bonani Mbanjwa

A thesis submitted to the Faculty of Engineering and the Built Environment, University of
the Witwatersrand, Johannesburg, in fulfilment of the requirements for the degree of
Doctor of Philosophy

Johannesburg, 2019

“Great things are done by a series of small things brought together.”

Vincent Van Gogh (1853-1890)

Declaration

I, Mesuli Bonani Mbanjwa, declare that this thesis is my own unaided work. It is being submitted to the Degree of Doctor of Philosophy to the University of the Witwatersrand, Johannesburg. It has not been submitted before for any degree or examination to any other University.

.....

..... day of,

Numerical simulation of multiphase dynamics in droplet-based microfluidics

Candidate: Mesuli Bonani Mbanjwa **Degree:** Doctor of Philosophy

Supervisor: Prof I.M.A. Gledhill

Co-supervisor: Prof K. Harding

Abstract

This work aimed to investigate dynamics involving mass transport in droplet flowing in microchannels system using numerical modelling and simulation. Droplet-based microfluidics or droplet microfluidics is a branch of microfluidics that deals with generation, manipulation and control of droplets in microchannels. Droplets flowing in microfluidic channels are effective self-contained micro-reactors for use in biological and chemical applications. The ability to generate multitudes of droplets with narrow size distribution and to control reagent volumes within individual droplets, allows for parallelisation of chemical processes in microfluidic channels. Droplet microfluidics is, thus, an exceptional tool for manufacturing and analysis in biological, chemical and nanotechnology applications.

Mixing processes in droplet microfluidics often involve three-way coupled physics of two-phase flow and mass transport (convection and diffusion) of chemical species, governed by a set of partial differential equations which require simultaneous solution. For two-phase flow, the equations for the movement and evolution of the interface are coupled to the Navier-Stokes of flow. In the case of transport of chemical species, the scalar mass transport equation is coupled to two-phase flow. The effects experienced in these systems are both multiscale and multiphase. Finite Element and Level Set simulations have been investigated and validated for modelling mass transport in droplet microfluidics systems. A set of benchmark cases has been developed for the purpose. Using Finite Element and Level Set simulations, a 2D two-phase moving-frame-of-reference modelling approach has been introduced and has been demonstrated to be an appropriate technique for investigation of mixing within droplets travelling in straight microchannels. This approach had not been previously demonstrated for the problem of mixing in droplet microfluidics, and requires less computational resources compared to the fixed frame-of-reference approach. Key conclusions of this work are:

- A limitation of the method exists for flow conditions where the droplet mobility approaches unity due to the moving wall boundary condition which results in an untenable solution under those conditions.

- As the size of the plug increases ($L_d \gg w_d$), the efficiency of the mixing is reduced.
- The initial orientation of the droplet influences the mixing and the transverse orientation provides better mixing performance than the axial orientation.
- The recirculation inside the droplet depends on the superficial velocity and the viscosity ratio.

To Ndimakazi, Kwande and Amyoli

Acknowledgements

I am truly grateful to **Prof Igle Gledhill**, my thesis supervisor, for her perpetual patience, enthusiasm, encouragement and for believing in me from the onset of this journey. I also thank my co-supervisor, **Prof Kevin Harding** for his invaluable critique, inputs and support.

I am indebted to my wife, **Ndimakazi** and our children, **Kwande Mikhosi** and **Amyoli Joy** for their love, patience and support, especially during the many days and nights I spent away from home.

My heartfelt gratitude goes to my mother **Joyce Bulewa**, who toiled selflessly, sacrificed and endured much so that we could get a decent education. *S'khubane, Nonjonjo!*

To my brothers, **Methuli** and **Siyanda**, and their respective spouses – Thank you, for always being there to provide your support and advice. *Hukanabetz!*

I am very thankful to my late aunt, **Mrs Theodora Breakfast**, for being a constant pillar of support for my mother during our studies and many other times of distress. *Kunje ngenxa yemisebenzi yakho yobubele. Phumla ke Mahlangebeza!*

I thank all my friends and extended family who, in many different ways, have added value in my life.

I thank **Mr Riaan Coetzee** and **Dr Kevin Land** at the CSIR for the opportunity to undertake this study.

Thank you to all my former colleagues at the CSIR who gave their assistance and support in various ways.

I also thank **Profs. Ted Moss, Linda Jewell** and **David Glasser** for their support during the course of this study.

Thank you to **Prof Jan Korvink** and **Dr Andreas Greiner** at for their hospitality and valuable discussions during my short stay at IMTEK, University of Freiburg.

Thank you to **Dr Ureshnie Govender** and **Mr Louis Fourie**, who I shared a workspace with, for the many light-hearted moments and for tolerating my episodes of grumbles and occasional outbursts of frustration.

Lastly, but not least, this work is dedicated to the anonymous altruists who, through their benevolent spirit and selfless deeds, ameliorate many lives.

Contents

DECLARATION	I
ABSTRACT	II
ACKNOWLEDGEMENTS.....	VI
CONTENTS.....	VIII
LIST OF TABLES	XIII
LIST OF FIGURES	XV
LIST OF SYMBOLS.....	XXII
ABBREVIATIONS.....	XXVIII
1. INTRODUCTION.....	1
1.1 Advances in miniaturisation and emergence of microfluidics	1
1.2 Multiphase phenomena in droplet microfluidics	2
1.3 Problem statement	5
1.4 Overall aim and specific objectives.....	5
1.5 Scope.....	6
1.6 Overview of thesis	6
2. LITERATURE REVIEW	8
2.1 Preliminary concepts	8
2.1.1 Interfacial tension.....	8
2.1.2 Dimensionless numbers and scaling law	10
2.2 Transport of microfluidic droplets	13
2.2.1 Dispersion of droplets in microchannels.....	14

2.3	Mixing in microfluidic droplets.....	16
2.3.1	Mixing dynamics and mechanisms.....	16
2.4	Modelling and simulation of droplet mixing.....	19
2.4.1	Domain modelling approach for flow field	20
2.4.2	Two-dimensional versus three-dimensional modelling	23
2.4.3	Coupling of variables	24
2.4.4	Quantification of mixing.....	25
2.5	Numerical methods for CFD.....	27
2.5.1	Continuum discretisation methods.....	27
2.5.2	Implicit methods for evolving fluid interfaces	30
2.5.3	Continuum surface force (CSF).....	34
2.5.4	Validation.....	35
2.6	Closing remarks	36
3.	NUMERICAL MODELLING USING FINITE ELEMENT AND LEVEL SET METHODS ...	37
3.1	Introduction	37
3.1.1	Equations governing two-phase flow.....	37
3.1.2	Mass transport equation	40
3.2	Finite element method	43
3.2.1	Initial and boundary conditions	43
3.2.2	Weighted residual formulation.....	44

3.2.3	Spatial discretisation.....	45
3.2.4	Galerkin method	46
3.2.5	Numerical solvers	47
3.2.6	Numerical stabilisation using artificial diffusion.....	49
3.3	Conservative level set method.....	50
3.3.1	Modelling of the evolution of fluid interface.....	50
3.3.2	Interfacial tension.....	52
3.3.3	Interface re-initialisation.....	54
4.	BENCHMARK COMPUTATIONS AND VALIDATION.....	55
4.1	Introduction	55
4.2	Two-dimensional stationary droplet.....	56
4.2.1	Spatial grid resolution.....	58
4.2.2	Interface thickness	65
4.2.3	Time step.....	69
4.2.4	Ohnesorge number	70
4.3	Dispersion of a chemical species in a microchannel.....	72
4.3.1	Diffusion.....	72
4.3.2	Taylor-Aris dispersion	78
4.4	Conclusion.....	91

5. MODELLING OF DROPLET MIXING USING TWO-PHASE MOVING-FRAME-OF-REFERENCE.....	93
5.1 Introduction	93
5.2 Development of numerical model.....	94
5.2.1 Assumptions.....	94
5.2.2 Model geometry	94
5.2.3 Mesh.....	96
5.2.4 Computation of the flow field.....	96
5.2.5 Quasi-steady-state condition.....	97
5.2.6 Computation of the concentration field	100
5.2.7 Dimensionless parameters.....	101
5.3 Parametric study.....	102
5.3.1 Capillary number.....	103
5.3.2 Droplet size	103
5.3.3 Viscosity ratio	103
5.4 Numerical results for flow field and hydrodynamics	104
5.4.1 Droplet mobility.....	104
5.4.2 Plug shape and size	105
5.4.3 Film thickness.....	111
5.4.4 Velocity field.....	113

5.5 Numerical results for the concentration field and mixing performance.....	118
5.5.1 Mixing index.....	118
5.5.2 Limitation of the droplet mixing model.....	119
5.5.3 Effect of initial orientation of solute species	125
5.5.4 Nose stagnation zone	127
5.5.5 Effect of droplet size	130
5.5.6 Effect of viscosity ratio	133
5.6 Conclusion.....	138
6. CONCLUSION.....	140
6.1 General discussion.....	140
6.2 Summary of key contributions.....	141
6.3 Conclusions.....	143
6.4 Recommendations for future work	143
REFERENCES	145
APPENDIX A: VELOCITY PROFILES IN RECTANGULAR MICROFLUIDIC CHANNELS....	157
APPENDIX B: EVALUATION OF ARTIFICIAL DIFFUSION PARAMETERS	160
APPENDIX C: MODIFIED PECKET NUMBERS AS FUNCTION OF THE CAPILLARY NUMBER FOR DIFFERENT PLUG SIZES	163
APPENDIX D: A BASIC BENCHMARKING OF THE COMPUTATIONAL COST BETWEEN TWO-PHASE MFR AND THE TWO-PHASE FFR APPROACHES.....	164

List of Tables

Table 2.1 Expression of forces that exist in microfluidic two-phase flows with dimensionless numbers and scaling laws (Squires & Quake, 2005; Bruus, 2008)	13
Table 3.1 Physical interpretation of terms in the generic transport equation (Kuzmin, 2010)	41
Table 4.1 Parameters for the six different meshes evaluated.	59
Table 4.2 Performance of the different spatial meshes as determined through the parameters Er , Up and $Aloss$	65
Table 4.3 Er , Up and $Aloss$ for 100 μm droplet for different interface thicknesses a determined at $\Delta t = 10^{-5}$ and $h_{max} = 2.03 \times 10^{-6}$	66
Table 4.4 The effect of time step on Er , Up , $Aloss$	69
Table 4.5 The influence of the interfacial tension and Oh_2 on Er , Up , $Aloss$	71
Table 4.6 Properties of the different meshes used in the diffusion numerical model.	74
Table 4.7 Comparison of minimum and maximum concentration (mol/m^3) values at various solution times obtained using PARDISO and multigrid solvers.	82
Table 4.8 Number of mesh elements required to maintain $Pe_h = 2$	88

Table 5.1 Parameters for the investigations of influence of viscosity ratio.....104

List of Figures

Figure 2.1 Illustration of principal radii of curvature caused by interfacial tension on an element of a fluid-fluid interface.	9
Figure 2.2 Droplet and plug flows in microchannel (Walker, 2016)	14
Figure 2.3 Lubrication film and corner gutters in a plug transported in a rectangular microchannel (Source: Author).....	15
Figure 2.4 Techniques for mixing visualisation and characterisation in microfluidic droplets: (a) time-averaged fluorescence (Bringer, <i>et al.</i> , 2004), (b) Reaction colour change (Sarrazin, <i>et al.</i> , 2007), (c) fluorescence lifetime imaging (i Solvas, <i>et al.</i> , 2010), (d) micro-particle image velocimetry (Malsch, <i>et al.</i> , 2008).....	18
Figure 2.5 Computational domain for modelling droplet or plug transport in two-phase fixed-frame-of-reference.	21
Figure 2.6 Computational domains used for modelling of droplet/plug transport in (a) single-phase moving-frame-of-reference and (b) two-phase moving-frame-of-reference.....	22
Figure 2.7 Different types of interface methods (Wörner, 2012).....	31
Figure 2.8 Spurious currents around an interface (black line) of a stationary droplet at $Ca=0.1$ (Zahedi, Kronbichler, & Kreiss, 2012).....	35
Figure 3.1 Two-phase Newtonian incompressible flow in an arbitrary domain ($\Omega = \Omega_j, j = 1, 2$) which is divided into two by the fluid interface Γ (After Cruanyes, 2014).....	39

Figure 3.2: (a) Discretisation of 2D arbitrary domain by triangulation, (b) Node i and neighbouring triangular elements, with a linear shape function φ (Adapted from Wilkes, 2006)..... 46

Figure 3.3 Level set for a 2D droplet varying smoothly between 0 and 1. (a) In the height contour data, the interface is represented by the black line contour equal to 0.5; (b) The red line shows how the interface varies, as described in the x -direction. 53

Figure 4.1 2D computational domain of the stationary droplet consisting of two fluid sub-domains Ω_1 and Ω_2 56

Figure 4.2 Six types meshes of various sizes. 59

Figure 4.3 Surface plots of pressure (in Pa) fields corresponding to the different meshes. 60

Figure 4.4 Graphs showing relation between the number of mesh elements and the numerical pressure at the centre of the droplet. The horizontal line shows the exact analytical solution. 61

Figure 4.5 Overlays of pressure profiles across the middle of the droplet, showing variations across the interface between the different grids (a) A-C and (b) D-F 62

Figure 4.6 Cross-sections of pressure and the fluid interface along a horizontal line through the middle of the droplet computed using grid (a) A and (b) E, compared to the exact solution for pressure..... 63

Figure 4.7 Reduction in parasitic currents by mesh refinement between (a) mesh A and (b) mesh E. The computed fluid interface is indicated with the black circle. The units for velocity are m/s. 64

Figure 4.8 (a) Cross-sectional profiles of (a)-(b) pressure and (c) interface, along a horizontal line through (0,0) the middle of the droplet for different value of ε as a factor of h_{max} . The cross-sectional profile of the exact solutions and initial interface are plotted. 68

Figure 4.9 One-dimensional diffusion of a tracer species between parallel plates..... 73

Figure 4.10: Colour plot of changes in concentration where the diffusion coefficient is $10 - 7 \text{ m}^2/\text{s}$ 75

Figure 4.11 Analytical and numerical solutions of the dimensionless concentration profile across the x-axis of the channel for diffusion coefficients: (c) $10 - 11 \text{ m}^2/\text{s}$ (b) $10 - 9 \text{ m}^2/\text{s}$ and (c) $10 - 7 \text{ m}^2/\text{s}$ determined at times of 500s, 0.1s and 1s, respectively..... 76

Figure 4.12 Dimensionless concentration profile across the x-axis of the channel at increasing times for diffusion coefficients: (a) $1 \times 10 - 11 \text{ m}^2/\text{s}$ (b) $1 \times 10 - 9 \text{ m}^2/\text{s}$ and (c) $1 \times 10 - 7 \text{ m}^2/\text{s}$ 77

Figure 4.13 Taylor dispersion as a result of the parabolic flow. Adapted from Wilkes (2006). 79

Figure 4.14 Dispersion of a solute tracer at high diffusion coefficient of $10 - 7 \text{ m}^2/\text{s}$. Concentration units are in mol/m^3 83

Figure 4.15 Dispersion of a solute tracer with a diffusion coefficient of $10 - 9 \text{ m}^2/\text{s}$. Concentration units are in mol/m^3 84

Figure 4.16 Dispersion of a solute tracer with a diffusion coefficient of $10 - 10 \text{ m}^2/\text{s}$. Concentration units are in mol/m^3 85

Figure 4.17 Dispersion of a solute tracer with at low diffusion coefficient of 5×10^{-12} m²/s. Concentration units are in mol/m³. 86

Figure 4.18 Exponential increase in required number of mesh elements to maintain $Pe\hbar = 2$ 88

Figure 4.19 Instabilities in the normalised concentration profile from the Taylor-Aris dispersion solution at $Pe = 500$ 89

Figure 4.20 Instabilities in the concentration profile from the solution of the Taylor-Aris dispersion at $Pe = 500$ with streamline Petrov-Galerkin compensated (PGC) tuned to 0.5 and anisotropic (AI) diffusion set at 0.25. 90

Figure 4.21 Instabilities in the normalised concentration profile from the solution of the Taylor-Aris dispersion at $Pe = 500$ with combined isotropic (ID), streamline Petrov-Galerkin compensated (PGC) and crosswind shock capturing (CWSC) tuned to 0.05, 0.5 and 0.35, respectively. 91

Figure 5.1 Schematic representation of the 2D model geometry for the current problem. 95

Figure 5.2 Initial and boundary conditions for a droplet travelling in microchannel modelled using a two-phase moving-frame-of-reference. 96

Figure 5.3 Illustration of the interface at the initial position (blue line) and when is at quasi-steady-state (red line). 98

Figure 5.4 Flow diagram for the iteration process towards quasi-steady-state of the flow solution. 99

Figure 5.5 Illustration of the two alternative initial arrangements of the solute species: (a) Axial orientation and (b) Transverse orientation. 101

Figure 5.6 Plot of droplet mobility (\mathcal{M}) versus capillary number (Ca) for different viscosity ratios. 105

Figure 5.7 Shape of the interface of the droplet at $Ca = 0.04, 0.06$ and 0.2 106

Figure 5.8 Illustration for characterisation of the droplet length (Ld), width (wd) and minimum film thickness (δf). 107

Figure 5.9 Dependence of the non-dimensionalised droplet length (Ld/w) on capillary number (Ca) at varying viscosity ratios. 108

Figure 5.10 Dependence of the non-dimensionalised droplet width (wd/w) on capillary number (Ca) at varying viscosity ratios. 109

Figure 5.11 Dependence of the non-dimensionalised length (Ld/w) on droplet mobility (\mathcal{M}) at varying viscosity ratios. 110

Figure 5.12 Dependence of the non-dimensionalised width (wd/w) on droplet mobility (\mathcal{M}) at varying viscosity ratios. 110

Figure 5.13 Dependence of the scaled film thickness ($\delta *$) on capillary number (Ca) at different viscosity ratios. 112

Figure 5.14 Dependence of the scaled film thickness ($\delta *$) on droplet mobility (\mathcal{M}) at different viscosity ratios. 112

Figure 5.15 Wall shear rate and x-velocity along the centreline ($y = h/2$) at $\lambda = 2$ 114

Figure 5.16 Wall shear rate and the x-velocity at centreline ($y = h/2$) for $\lambda = 0.5$ 115

Figure 5.17 Wall shear rate and the x-velocity at centreline ($y = h/2$)
for $\lambda = 0.5$ 116

Figure 5.18 Wall shear rate and the x-velocity at centreline ($y = h/2$)
for $\lambda = 2$ 117

Figure 5.19 Conservation of chemical species for the convection-
dominated mixing case $Ca = 0.21, \lambda = 0.1$ 121

Figure 5.20 Conservation index for the diffusion-dominated mixing
case $Ca = 0.018, \lambda = 2$ 122

Figure 5.21 Comparison for conservation of chemical species in the
droplet between two cases in 6.5 ms mixing time; the
convection-dominated ($\lambda = 0.1, Ca = 0.21$) and the
diffusion-dominated ($\lambda = 2, Ca = 0.018$). 123

Figure 5.22 Conservation index for the diffusion only case. 124

Figure 5.23 Effect of the initial mixing orientation on the mixing index
for droplets of different sizes at $Ca = 0.21$ and $\lambda = 0.1$ 125

Figure 5.24 Relation between mixing index and of non-dimensional
mixing distance for different the initial mixing orientations
at $Ca = 0.21$ and $\lambda = 0.1$ 126

Figure 5.25 Influence of stagnation zones on poor mixing at the nose of
the droplet/plug. 127

Figure 5.26 Relation between the capillary number and the nose
recirculation length at $\lambda = 0.5$ and $L0 = 2h$ 128

Figure 5.27 Relation between the viscosity ratio and the nose
recirculation length at $Ca = 0.21$ and $L0 = 2h$ 129

Figure 5.28 Comparison of mixing indexes for droplets with initial lengths of h , $2h$ and $5h$ and transverse solute orientation at conditions of $Ca = 0.21$ and $\lambda = 0.1$ 130

Figure 5.29 Comparison of non-dimensional mixing distance for droplets with initial lengths of h , $2h$ and $5h$ and transverse solute orientation at conditions of $Ca = 0.21$ and $\lambda = 0.1$ 131

Figure 5.30 Comparison of non-dimensional mixing distance for droplets with initial lengths of h , $2h$ and $5h$ and axial solute orientation at conditions of $Ca = 0.21$ and $\lambda = 0.1$ 132

Figure 5.31 Comparison of non-dimensional mixing distance for droplets with initial lengths of h , $2h$ and $5h$ and axial solute orientation at conditions of $Ca = 0.21$ and $\lambda = 0.1$ 133

Figure 5.32 Concentration field plots of mixing at different times for $Ca = 0.21$ and $\lambda = 0.5$ 134

Figure 5.33 Concentration field plots of mixing at different times for $Ca = 0.21$ and $\lambda = 2$ 134

Figure 5.34 Comparison of mixing performances for various viscosity ratios at $Ca = 0.21$ 135

Figure 5.35 Comparison of mixing performances for various viscosity ratios at $Ca = 0.15$ 135

Figure 5.36 Influence of the viscosity ratio on mixing time (tm) and dimensionless mixing distance ($tmUdL0$) 136

List of Symbols

A	Major axis of an ellipse	[m]
A_d	Area of a droplet	[m ²]
a	Factor numerical fitting parameter	[m]
B	Minor axis of an ellipse	[m]
b	Exponent numerical fitting parameter	[m]
C	Concentration	[mol/m ³]
\bar{C}	Average concentration	[mol/m ³]
C_i	Concentration of chemical species i	[mol/m ³]
C_0	Initial concentration of solute	[mol/m ³]
\bar{c}	Amount per unit mass (mass-specific concentration)	[amount/kg]
c	Amount per unit volume ($= \rho\bar{c}$)	[amount/m ³]
Ca	Capillary number	[-]
CFL	Courant-Friedrichs-Lewy /Courant number	[-]
CFL_p	Courant number due to parasitic currents	[-]
D	Coefficient of molecular diffusion /Mass diffusivity	[m ² /s]
D_i	Coefficient of molecular diffusion of chemical species i	[m ² /s]
\mathbb{D}	Mass diffusivity tensor	[m ² /s]
d	Droplet diameter	[m]
d_h	Hydraulic diameter	[m]

d_n	Prescribed nose diameter of the droplet	[m]
d_t	Prescribed tail diameter of the droplet	[m]
E_c	Cohesive energy between molecules	[J/m ²]
\mathbb{G}	Deformation tensor	
\mathcal{H}_{sm}	Smoothed Heaviside function	
h	Height of a microchannel	[m]
h	Mesh size	[m]
h_{max}	Size of the largest mesh element	[m]
I	Intensity of segregation	[-]
\mathbb{I}	Identity tensor	
l	Length	[m]
K	Taylor-Aris dispersion coefficient.	[m ² /s]
L	Length of microchannel	[m]
L_c	Length of microchannel	[m]
L_0	Prescribed initial length of a droplet/plug	[m]
L_d	Length of a droplet/plug	[m]
La	Laplace number	[-]
ℓ	Length scale	[m]
ℓ_d	Diffusion length scale	[m]
N	Element node	
Oh	Ohnesorge number	[-]
p	Pressure	[Pa]

Pe	Peclet number	[-]
Pe_{\hbar}	Mesh Peclet number	[-]
Pe_L	Peclet number across microchannel length	[-]
Pe_m	Modified Peclet number / Peclet number for a moving droplet/plug	[-]
Q	Volumetric flowrate	[m ³ /s]
r	Droplet radius / Radius of interface curvature	[m]
r_{mix}	Mixing rate	[s ⁻¹]
Re	Reynolds number	[-]
Re_p	Reynolds number due to parasitic currents	[-]
S	Boundary surface or control surface	
\mathbb{S}	Cauchy Stress tensor	[N/m ²]
s	Source term describing creation or consumption of mass	[mol/m ³ ·s]
Sc	Schmidt number	[-]
T	Matrix transpose function	[-]
t	Time	[s]
t_c	Convection time	[s]
t_d	Diffusion time	[s]
t_m	Mixing time	[s]
t_r	Residence time	[s]
U	Average flow velocity	[m/s]

u	Arbitrary scalar variable	a.u.
\mathbf{u}	Velocity field	[m/s]
u_x	x-component of the velocity field	[m/s]
u_y	y-component of the velocity field	[m/s]
U_d	Velocity of droplet (or bubble) in two-phase flow	[m/s]
U_p	Magnitude of spurious/parasitic currents	[m/s]
U_w	Moving wall velocity	[m/s]
V	Control volume	[m ³]
w	Width of microchannel	[m]
w_0	Prescribed initial width of a droplet/plug	[m]
w_d	Width of a droplet/plug	[m]
We	Weber number	[-]
\mathbf{x}	Cartesian coordinate system (x,y,z)	[m]
x	Horizontal axis of Cartesian plane	[m]
X_n	Distance between droplet nose and the front end of the microchannel	[m]
X_t	Distance between droplet tail and the back end of the microchannel	[m]
y	Vertical axis of Cartesian plane	[m]
z	Inward axis of Cartesian plane	[m]

Greek symbols

α	Sparse (system) matrix	
β	Solution vector (matrix of unknowns)	
γ	Interface re-initialisation parameter	[m/s]
$\dot{\gamma}$	Shear rate	[s ⁻¹]
δ	Dirac delta function	[-]
δ_{sm}	Smoothed Dirac delta function	[-]
δ_f	Boundary (wetting) film thickness	[m]
Δ	Change	[-]
ε	Parameter controlling interface thickness	[m]
θ	Contact angle	[degrees]
κ	Mean interfacial curvature	[1/m]
λ	Viscosity ratio	[-]
μ	Dynamic viscosity	[Pa·s]
ρ	Density	[kg/m ³]
σ	Interfacial tension	[N/m]
τ	Interface re-initialisation time	[s]
ϕ	Level set function	[-]
Γ	Fluid-fluid interface	[m ²] or [m]
ψ	Density ratio between dispersed and continuous phase	[-]
χ	Non-dimensionalised mixing rate	

Ψ_k	Linear shape function for k node	
Ω	Computational domain	[m ³] or [m ²]
$\partial\Omega$	Boundary surface of the domain	[m] or [m ²]

Abbreviations

ALE	Arbitrary Lagrangian- Eulerian
a.u.	Arbitrary units
BC	Boundary condition
BDF	Backward Differentiation Formulas
BiCGStab	Biconjugate gradient stabilized method
CAE	Computer aided engineering
CFD	Computational fluid dynamics
CSF	Continuum surface force
CSIR	Council for scientific and industrial research
CSS	Continuum surface stress
CV	Coefficient of variation
DOF	Degrees of freedom
FDM	Finite difference method
FE	Finite element
FEM	Finite element method
FGMRES	Flexible generalized minimal residual (method)
FVM	Finite volume method
GLS	Galerkin least squares
GMRES	Generalized minimal residual (method)
GUI	Graphical user interface

LBM	Lattice-Boltzmann method
LSM	Level set method
LU	Lower, upper
MEMS	Micro-electromechanical system
o/w	Oil-in-water
OpenFOAM	Open field operation and manipulation
PARDISO	Parallel direct solver
PDE	Partial differential equation
SPOOLES	Sparse object-oriented linear equations solver
SSOR	Symmetric successive over-relaxation (method)
SUPG	Streamline upwind Petrov-Galerkin (method)
μ TAS	Micro Total Analysis Systems
TAUCS	Cholesky solver
UMFPACK	Unsymmetric multifrontal package (method)
VOF	Volume of fluid

"The beginning is the most important part of the work." -- Plato

Chapter 1

Introduction

1.1 Advances in miniaturisation and emergence of microfluidics

Since the advent of the silicon transistor in the late 1940s and the subsequent establishment of semiconductor processes, scientists and engineers have been progressively harnessing the power of miniaturisation to improve our way of life. For example, computers have evolved from the days of the room-sized machine called "The ENIAC", into more advanced gadgets that can be held in our hands. Microfabrication technologies have revolutionised the modern electronics and computer industries, such that modern computer is not only orders of magnitude smaller, but it is more powerful, faster, cheaper and consumes far less energy than its predecessors. Advances in fabrication technologies in microelectronics and micro-electromechanical systems (MEMS) have also contributed to the emergence of the field of microfluidics (Whitesides, 2006).

Microfluidics is a multidisciplinary field that pertains to methods, processes, and tools for handling and controlling fluids on a very small scale, typically in microchannels of the order of 10 μ m to 1mm. Microfluidics is generally

accepted as a relatively new discipline and has been rapidly growing since the emergence of microfluidic devices focussed on applications for analytical chemistry in the early 1990s, known as micro total analysis systems (μ TAS) (Manz, *et al.*, 1990). These early foundations of microfluidics were influenced by the well-established analytical chemistry methods, such as high-pressure liquid chromatography (HPLC), gas-phase chromatography (GC) and capillary electrophoresis (Whitesides, 2006). In subsequent years, a number of manufacturing applications in, for example, areas such as synthetic biology, chemical manufacturing and production of pharmaceutical compounds were demonstrated (Dittrich & Manz, 2006; Godin, *et al.*, 2008; Gulati, *et al.*, 2009; Sackmann, *et al.*, 2014; Vyawahare *et al.*, 2010).

1.2 Multiphase phenomena in droplet microfluidics

Droplet-based microfluidics or droplet microfluidics is a branch of microfluidics that deals with generation, manipulation and control of droplets in microchannels (Teh *et al.*, 2008). Droplets flowing in microfluidic channel are effective self-contained micro-reactors for use in biological and chemical applications (Song *et al.*, 2006). The compelling functionality of droplet microfluidics is the ability to control reagent volumes with precision, generation of droplets in a reproducible manner, and parallelisation of processes within individual droplets (Teh *et al.*, 2008). Droplet microfluidics, therefore, provides an exceptional tool for manufacturing and analysis in biological, chemical and nanotechnology applications (Mashaghi, *et al.*, 2016).

In a separate project from the current research, the author and co-workers demonstrated the application of droplet microfluidics in the preparation of proprietary self-immobilised enzyme microspheres (Mbanjwa, *et al.*, 2018).

Mixing processes in droplet microfluidics often involve three-way coupled physics of two-phase flow and mass transport (convection and diffusion) of chemical species, governed by a set of partial differential equations which require simultaneous solution. For two-phase flow, the equations for the movement and evolution of the interface are coupled to the Navier-Stokes (flow), and for transport of chemical species, the scalar mass transport equation is coupled to both of the latter. The effects experienced in these systems are both multiscale and multiphase. The length scales at which the flow, the fluid interface and the molecules in the chemical species exist are all variable, by factors which are of several orders of magnitude. The term 'multiphase' in this work refers to two-phase flow and mass transport, as a collective. The behaviour of the multiphase phenomena is both transient (unsteady) and non-linear due to evolving fluid interfaces, even though they exist in microfluidic conditions of low Reynolds numbers. Under these conditions, analytical solutions are often not implementable, leaving experimental and numerical techniques as the only means of approach in finding a solution or generating a reliable means of understanding.

Numerical modelling and simulation using computational fluid dynamics (CFD) has over the years been demonstrated as an effective and a reliable tool

for study and analysis of wide range of fluid flow problems, including single-phase and multiphase microfluidic flows. Increased computational capabilities in recent years, has also led to decreased time cost of performing numerical simulations and has made it feasible to tackle problems of increased complexity.

COMSOL Multiphysics™, Version 3.5a (Comsol AB, Sweden), a commercial software program was selected as the numerical tool for undertaking CFD modelling and simulations in this work. The compelling attribute of COMSOL Multiphysics™ (COMSOL) are its functionalities and capabilities which transcend those of a basic CFD program. COMSOL is a versatile numerical package with an advantage of being able to model a range of problems which have coupled physics, typical in many microfluidic applications. For example, numerical studies of multi-physics phenomena in microfluidics such as mixing in microdroplets, magnetophoretic DNA isolation, dielectrophoretic manipulation of biological cells, and acoustofluidic transport of microparticles, have been conducted using COMSOL (Das, *et al.*, 2014; Hale & Darabi, 2018; Jiang, *et al.*, 2012; Lei, *et al.*, 2014).

An additional determinant in the selection of COMSOL was the availability of the software licence which had been procured and purchased prior the onset of the current study. The cost considerations were also taken into account in reaching the decision for its utilisation. The work was undertaken at the

Council for Scientific and Industrial Research (CSIR) where the author was employed.

1.3 Problem statement

Reported studies on mixing within droplets in microreactors have been largely experimental. The analysis methods are confined to imaging techniques which are limited in scope and detail. Whilst numeral studies focusing on the subject also exist, there are significant gaps in theory and understanding of mixing phenomena within microfluidic droplets.

1.4 Overall aim and specific objectives

The overall aim of the study is to investigate dynamics in a droplet microfluidic system involving mass transport by numerical modelling and simulation. The specific research objectives were:

- To validate the chosen numerical tool, COMSOL, using a selected set of benchmark numerical cases.
- To determine hydrodynamic and mass transport factors influencing mixing in droplets travelling in straight microchannels using a two-phase moving-frame-of-reference approach.

- To identify the applicability and limitations of the two-phase moving-frame-of-reference approach in the case of a droplet travelling in a straight microfluidic channel.

1.5 Scope

The scope of this study is limited to pressure-driven liquid-liquid two-phase flow, consisting of Newtonian fluids. The flows are confined in rectangular microchannels and exhibit laminar behaviour, typical in microfluidic conditions. All flows are considered under isothermal conditions with no gradients in surface or interfacial tension.

1.6 Overview of thesis

This thesis is organised and structured in different chapters as follows:

- **Chapter 1** provides a background and context for the current study. The research problem, scope and objectives of this study are also articulated.
- **Chapter 2** is a literature review chapter on multiphase phenomena, droplet mixing in microfluidics, and numerical modelling and simulation of mixing using CFD.
- **Chapter 3** outlines the details of the theoretical framework for numerical modelling and simulation of multiphase phenomena in

microfluidics. Specifically, the discussion focusses on the implementation FEM and LSM in two-phase flows with mixing effects.

- **Chapter 4** presents benchmark computations which demonstrate the suitability and the limitations of the chosen numerical tools for the current study.
- **Chapter 5** deals with mixing and dispersion in microfluidic plugs. Simulations are performed using a moving-frame-of-reference using single phase flow.
- **Chapter 6**, as a concluding chapter, provides a general discussion and conclusions of the study, as well as recommendations for future work.

"All is but soap bubbles." -- Pierre-Gilles de Gennes

Chapter 2

Literature Review

2.1 Preliminary concepts

2.1.1 Interfacial tension

The origins of interfacial tension are both molecular and physical (Israelachvili, 2011; de Gennes, *et al.*, 2004). Interfaces between immiscible fluids deform in order to minimise their surface energies and this distortion is opposed by surface tension (de Gennes, *et al.*, 2004). Surface tension is present in a gas-liquid system as a result of the molecules at the interface pulling towards their own kind in the bulk fluid with cohesion energy (E_c). A molecule of length scale or size (a) that sits at the interface will experience half of the pulling energy ($E_c/2$). If a surface area (a^2) of the said molecule is exposed, the surface tension (σ) can be then expressed as $\sigma \sim E_c/2a^2$ (de Gennes, *et al.*, 2004). The presence of interfacial tension in a liquid-liquid system is analogous to surface tension. The interfacial tension is characterised by the existence of a liquid-liquid interface, while surface tension exists in the case of a gas-liquid interface (*i.e.* liquid surface).

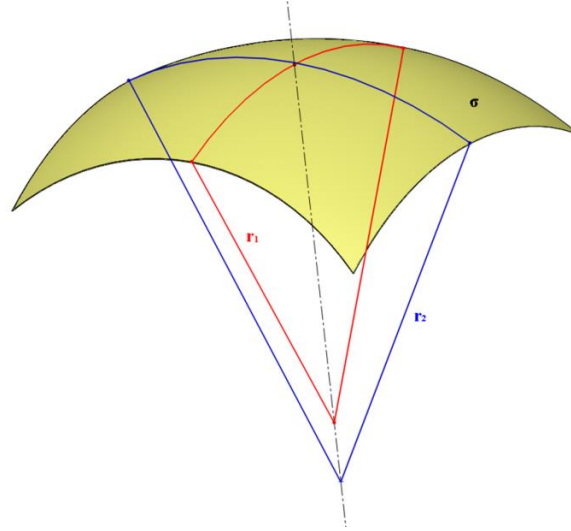


Figure 2.1 Illustration of principal radii of curvature caused by interfacial tension on an element of a fluid-fluid interface.

The pressure jump across a deformed fluid interface (Figure 2.1) can be expressed by the Young-Laplace equation, given by (de Gennes, *et al.*, 2004)

$$\Delta p = \sigma \left(\frac{1}{r_1} + \frac{1}{r_2} \right) \quad (2.1)$$

where r_1 and r_2 are principal radii of the interface curvature, $\left(\frac{1}{r_1} + \frac{1}{r_2} \right)$. In the case of an interface of a spherical droplet, with a radius $r = r_1 = r_2$, Eqn. (2.1) becomes

$$\Delta p = \frac{2\sigma}{r} \quad (2.2).$$

2.1.2 Dimensionless numbers and scaling law

Various force relations which exist in droplet microfluidic systems can be expressed in terms of the dimensionless numbers. The well-known dimensionless number in fluid dynamics is the Reynolds number (Re) which is the ratio of the inertial forces to the viscous forces. In a system with a length scale, ℓ and an average velocity U ,

$$Re = \frac{\rho U \ell}{\mu} \quad (2.3)$$

where ρ and μ represent the density and viscosity of the fluid, respectively. In microfluidic flow in rectangular microchannels, the applicable length scale is in the order of the width and the depth of the channel, expressed as hydraulic diameter d_h , such that $Re = \rho U d_h / \mu$. Typical Re values in microfluidics can be from $\mathcal{O}(10)$ down to $\mathcal{O}(0.1)$. Stokes flow (*i.e.* $Re \ll 1$) is not uncommon in droplet microfluidics where viscous fluids such as oils are handled. Inertial effects in such cases are negligible, leaving viscous effects to compete with interfacial or capillary forces. These effects often dominate over other effects. The capillary number (Ca) demonstrates the significance of the interfacial tension in relation to the viscous forces.

$$Ca = \frac{\mu U}{\sigma} \quad (2.4)$$

When $Re > 1$, the effect on inertia should not be ignored (White, 2006; Christopher & Anna, 2007). In two-phase flows, the Weber number (We) the ratio that gives the significance of inertia over interfacial tension

$$We = \frac{\rho U^2 \ell}{\sigma} \quad (2.5)$$

The Ohnesorge number (Oh) is a ratio of the viscous forces to the interfacial forces and is analogous to Re for interfacial flows (Kumacheva & Garstecki, 2011)

$$Oh = \frac{\mu}{\sqrt{\rho \sigma a_h}} \sqrt{\frac{Ca}{Re}} \quad (2.6)$$

The significance of gravity in a two-phase microfluidic flow can be demonstrated by the Bond number (Bo)

$$Bo = \frac{g \rho \ell}{\sigma} \quad (2.7)$$

Bo is often not considered in two-phase microfluidics due to negligible effects of gravity in relation to the interfacial tension, where $Bo \sim \mathcal{O}(10^{-5})$. In systems in which fluid mixing occurs, a ratio of convective transport to the diffusive transport as defined by the Peclet (Pe) number is to be considered (Kirby, 2010).

$$Pe = \frac{U \ell_d}{D} \quad (2.8)$$

where ℓ_d is the diffusion length and D is the molecular diffusivity or diffusion coefficient of the chemical species. Diffusion in a microfluidic channel is typically considered across its width w , and the Peclet number is determined from $Pe = \frac{Uw}{D}$. Schmidt number Sc which is the, ratio of viscosity to diffusivity relates Re to $Pe = Re.Sc$

$$Sc = \mu/\rho D \quad (2.9)$$

Sc is independent of flow and can, therefore, only be determined from the properties of the liquid/solution. Systems with low Pe and Sc values are preferable to due to high diffusion, which can result in efficient mixing despite laminar flow. It is possible to achieve this if the species is highly diffusive, or in the case of Pe , if the diffusion length scale is reduced through, for example, chaotic advection (Kirby, 2010; Stroock, *et al.*, 2002). A summary of the important dimensionless numbers with corresponding scaling law for two-phase microfluidics, together with typical parametric values is provided in Table 2.1. The concept of scaling laws provides insights regarding the influence of diminishing length scales on physical properties of systems (Bruus, 2008; Wautelet, 2001). Scaling law can be applied in analysis of a microsystem, whereby the variation of physical quantities is expressed with the length scale ℓ of the system, while keeping other parameters such as time, pressure and temperature remain constant (Bruus, 2008). The volume forces (gravity and inertia) and surface forces (viscosity and interfacial tension) which interplay in two-phase flows in microchannels can be expressed as ratios using the basic scaling law (Bruus, 2008)

$$\frac{\text{surface forces}}{\text{volume forces}} \propto \frac{\ell^2}{\ell^3} = \ell^{-1} \xrightarrow{\ell \rightarrow 0} \infty \quad (2.10)$$

Equation (2.16) implies that the significance of surface forces in relation volume forces will increase as the length scale decreases.

Table 2.1 Expression of forces that exist in microfluidic two-phase flows with dimensionless numbers and scaling laws (Squires & Quake, 2005; Bruus, 2008)

Dimensionless number	Significance	Scaling law	Typical value*
Bo	$\frac{\text{gravitational effects}}{\text{interfacial effects}}$	ℓ^2	10^{-5}
Ca	$\frac{\text{viscous effects}}{\text{interfacial effects}}$	ℓ	10^{-2}
Pe	$\frac{\text{convection}}{\text{diffusion}}$	ℓ^2	$10-10^7$
Re	$\frac{\text{inertial effects}}{\text{viscous effects}}$	ℓ^2	10^{-2}
Oh	$\frac{\text{interfacial effects}}{\text{viscous effects}}$	ℓ^{-1}	1
We	$\frac{\text{inertial effects}}{\text{interfacial effects}}$	ℓ^3	10^{-3}

*For typical two-phase microfluidic flow with the characteristics, $d_h \cong 10^{-4}m$, $\rho_c \cong 10^3 \text{ kg/m}^3$, $\mu_c \cong 10^{-2} \text{ Pa s}$, $\sigma \cong 10^{-2} \text{ N/m}$, $g \cong 10^{-2} \text{ m/s}^2$ and $U \cong 10^{-2} \text{ m/s}$, where the fluid properties are for the continuous phase.

2.2 Transport of microfluidic droplets

Microfluidics allows for thousands of droplets to be generated within microchannels at various frequencies ranging from low to very high frequencies. The frequencies and the size are dependent on the application but also limited by prevailing hydrodynamics. These hydrodynamic limitations often require careful consideration of the parameters such microchannel dimensions and fluid properties.

2.2.1 Dispersion of droplets in microchannels

'Plugs' are defined as large droplets which have an elongated shape form (i.e. aspect ratio greater than unity) as illustrated in Figure 2.2.

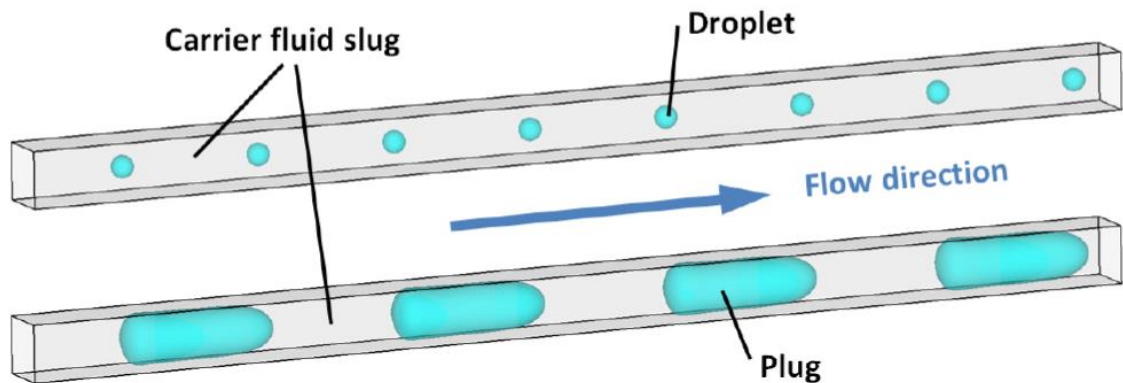


Figure 2.2 Droplet and plug flows in microchannel (Walker, 2016)

Shear effects on a fluid-fluid interface of a microfluidic droplet directly influence its interior flow dynamics. Due to various degree of confinement by the walls and resulting shear, droplets and plugs travelling in microchannels exhibit different dynamics (Bruneau, *et al.*, 2008). The source of the shear is the surrounding carrier fluid and the confining microchannel walls. Confinement is can result to both 2D and 3D flow effects within the droplet. In the case of rectangular microchannels, the 3D flow effects are most prominent when the aspect ratio $(w/h) \sim 1$. When $(w/h) \gg 1$, the x and y velocities exhibit little or no influence from the z velocities

(Tanthapanichakoon, *et al.*, 2006a). This case is typical of a slit microchannel and similar to flow between parallel plates.

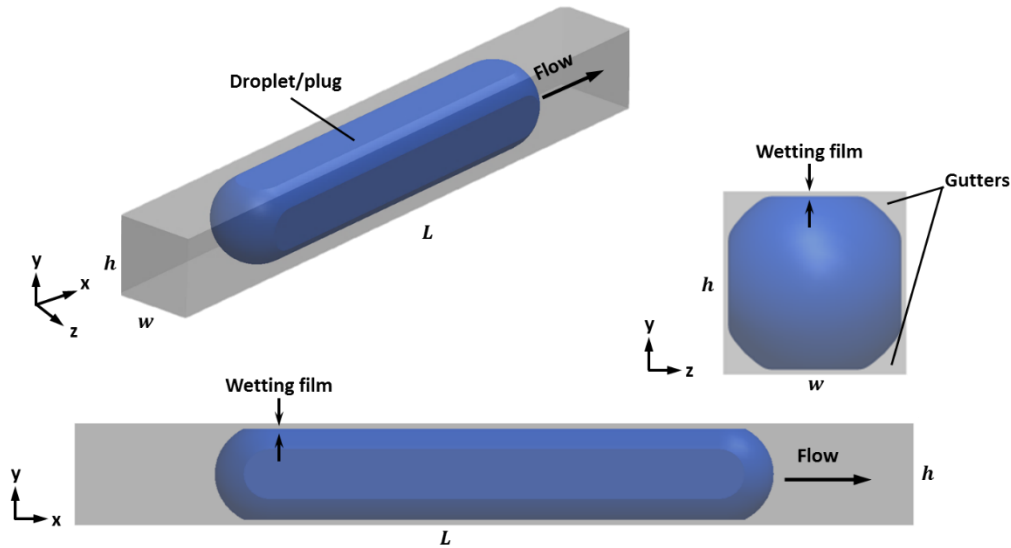


Figure 2.3 Lubrication film and corner gutters in a plug transported in a rectangular microchannel (Source: Author).

A lubrication film (Figure 2.3) can exist between the carrier fluid and the wall, as a result of the competition between viscous drag and capillary pressure (Baroud, *et al.*, 2010). The classical works by Taylor (1961) and Bretherton (1961) established the existence of the relationship between the capillary number and the lubrication film. A scaling model for a boundary film in gas-liquid flow in circular capillaries was first reported by Bretherton following on Taylor's experimental work. The model expressed the boundary film thickness δ_f as directly proportional to $Ca^{2/3}$. Aussillous & Quéré (2000) extended the scaling model and validated it empirically. Bretherton scaling

and its extensions are useful in validating numerical models for droplet and bubble flows in microchannels (Afkhami, *et al.*, 2011, Hoang, *et al.*, 2013).

Rectangular microchannels have corners which act as gutter in the as shown in Figure 2.3, where the there is flow of the carrier fluid. The profile of the wetting film square microchannel differs from that of the circular capillaries. As such, the gutters in square microchannel exhibit fluid leakage which should be taken into account when a 2D model is implemented, due to the unique hydrodynamics of the square case (Taha & Cui, 2006a). The interface can also deform into the corners such that the droplet /plug is no longer axis-symmetric (Wang & Dimitrakopoulos, 2012)

2.3 Mixing in microfluidic droplets

Due to the laminar nature of microfluidic flows, mixing of chemical species in single phase fluids are often limited by diffusion and Taylor dispersion. Droplets in microchannels offer an attractive alternative for improved mixing.

2.3.1 Mixing dynamics and mechanisms

Mixing in microfluidic droplets is dominated by convective effects which emanate shearing imparted as a result of droplet transport. Factors which influence flow dynamics within the droplet, therefore convection include:

- (i) fluid viscosity,
- (ii) droplet speed,
- (iii) droplet size relative microchannel size,
- (iv) channel geometry and
- (v) flowrates.

Microfluidic systems, mostly, rely on optically-based methods for quantification of mixing (Aubin, *et al.*, 2010). An optimal method for quantification of mixing in discrete flow in microfluidics remains a real challenge. Various works have focussed on the concept of mixing by chaotic advection in droplets, using experimental and numerical studies. For example, Song *et al.* (2003) used time-averaged fluorescence imaging to quantify mixing in microfluidic droplets. The extent of mixing was quantified by relative normalized intensity of fluorescence as a function of distance travelled by the plugs in a specific time. Sarrazin *et al.* (2007) used experimental investigations study the effect of geometry in serpentine microchannel. However, the investigations were limited to qualitative visual observations of a colour changing acid-base reaction. Tice *et al.* (2003) characterised mixing profiles in microfluidic plugs, containing aqueous reagents, through optical visualisation in a stereomicroscope fitted with a digital camera. Aqueous solutions of thiocyanatoiron complexes (inorganic dyes), were better suited for visualisation than food-grade colourants (organic dyes). Fluorescence lifetime imaging provides a means for quantifying mixing in droplets through combination of intensity and

fluorescence lifetime (i Solvas, *et al.*, 2010). This technique provides better quantification than using only the intensity. A Schieleren technique has potential for application in the quantification of droplet-confined mixing in microfluidics (Sun & Hsiao, 2013). A review by Aubin *et al.*, (2010) looks at experimental methods used in the characterisation of mixing in general microfluidics. Some of the experimental techniques used for visualisation of mixing dynamics are shown in Figure 2.4.

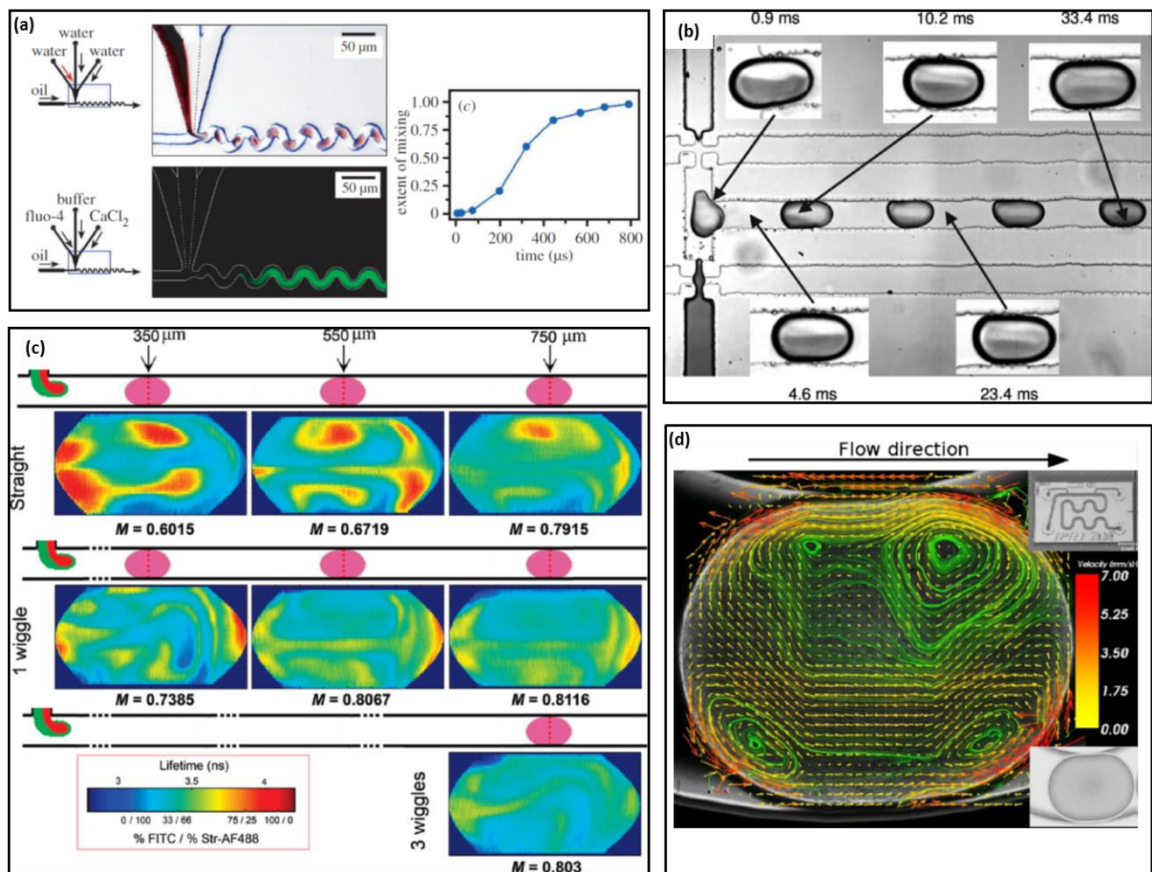


Figure 2.4 Techniques for mixing visualisation and characterisation in microfluidic droplets: (a) time-averaged fluorescence (Bringer, *et al.*, 2004), (b) Reaction colour change (Sarrazin, *et al.*, 2007), (c) fluorescence lifetime

imaging (i Solvas, *et al.*, 2010), (d) micro-particle image velocimetry (Malsch, *et al.*, 2008).

The flow field dynamics within droplets flowing in rectangular microchannels have been investigated using experimental techniques such as confocal micro particle image velocimetry (μ PIV) for 3D flow (Kinoshita, *et al.*, 2006) and micro particle shadow velocimetry (Khodaparast, *et al.*, 2014), as well as by numerical models (Sarrazin, *et al.*, 2008). The majority of work reviewed focusses on straight channels and a handful of published work considered winding microchannel (Malsch, *et al.*, 2008; Che, *et al.*, 2010). Malsch *et al.* (2008) used μ PIV technique to study the fluid dynamics within a droplet travelling a serpentine microchannel. Che, *et al.*, (2010) developed 2D analytical model for describing flow of plugs in microchannel bends. The results indicated that for shorter plugs moving with low channel curvature the vortex centres tend to be located next to the walls.

2.4 Modelling and simulation of droplet mixing

The numerical models concerned with droplet mixing in microchannels usually have two aspects of interest. The first aspect deals with the flow and the transport of the droplets in the microchannel. The second aspect relates to the mass transport aspects and mixing of the species within and across the droplets. The mixing is dependent on the nature of the prevailing flow conditions.

Some reviews focussed on the two-phase flow in microchannels (Bordbar, *et al.*, 2018; Liu & Nguyen, 2010). Studies and reviews concerned with modelling and simulation heat transfer and two-phase flow in microchannels also provide valuable insight on the flow aspect (Abdollahi, *et al.*, 2017; Bandara, *et al.*, 2015; Talimi, *et al.*, 2012). Wörner (2012) provided a comprehensive review of numerical modelling and simulation of multiphase flows in microchannels and applications.

2.4.1 Domain modelling approach for flow field

There are two main categories in the approaches in the modelling the flow field of droplets and plugs in microchannel. These are fixed-frame-of-reference and the moving-frame-of-reference.

2.4.1.1 Fixed-frame-of-reference

The schematic in Figure 2.5 shows the computational domain for a two-phase fixed-frame-of-reference. This domain approach is also used in simulations of droplet generation in systems such as the T-junction, flow focussing and mixed-phase inlets. Essentially the domain is the observation window for the droplet is fixed and the flow moving out of the domain (Eulerian approach).

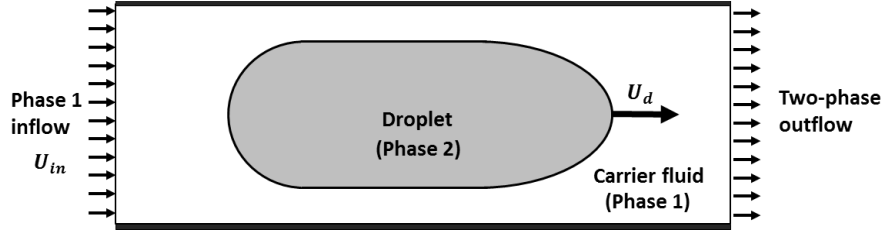


Figure 2.5 Computational domain for modelling droplet or plug transport in two-phase fixed-frame-of-reference.

Computationally, the two-phase fixed-frame-of-reference is the costliest. In addition to the fine mesh required to capture the evolving interface, larger observation window maybe required where time scales are short, for example in fast moving droplets.

2.4.1.2 *Moving-frame-of-reference*

The moving-frame-of-reference is an alternative approach for modelling moving droplets in a straight microchannel. There are two approaches in the moving-frame-of-reference; the single-phase and the two-phase. In the moving-frame-of-reference, the flow field is modelled in the frame of reference of the moving the droplet (Lagrangian approach). The single-phase moving-frame-of-reference is the simplest and least costly, of the three approaches, computationally. As illustrated in Figure 2.6 (a), the droplet or a plug is modelled as a single-phase whose flow field is driven by moving walls boundary condition.

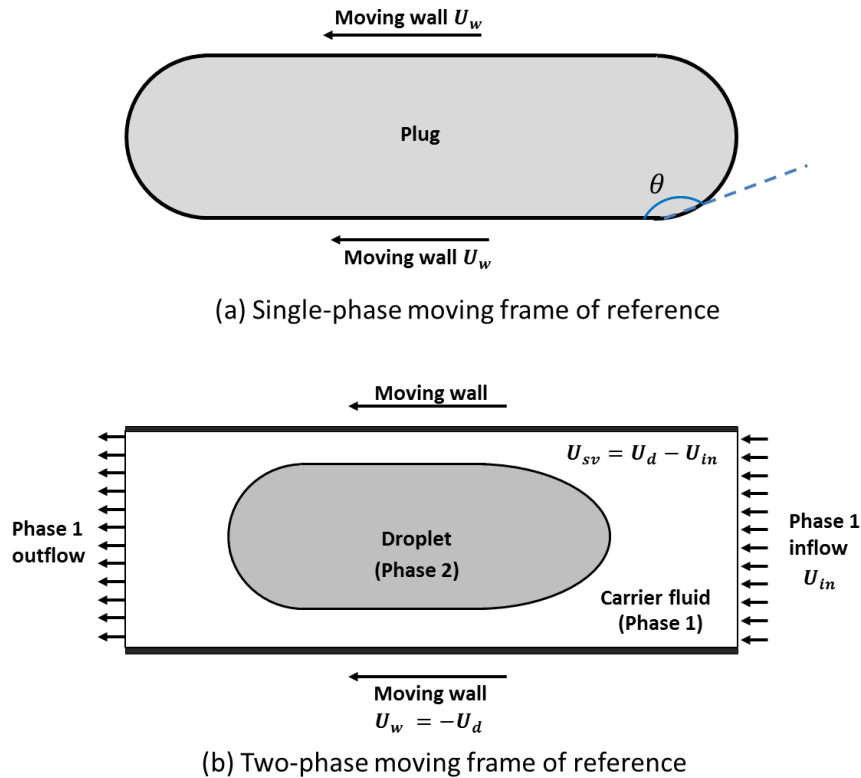


Figure 2.6 Computational domains used for modelling of droplet/plug transport in (a) single-phase moving-frame-of-reference and (b) two-phase moving-frame-of-reference.

The model focusses on a single flow field in either inside or outside the droplet or plug (Handique & Burns, 2001; Tanthapanichakoon, *et al.*, 2006a, 2006b and 2007). Consequently, fewer equations are solved than in two-phase model leading to faster results. The approach, however, requires *a priori* assumptions regarding shape of the interfaces and shear rates (Kashid, *et al.*, 2005). These parameters which influence the crucial aspects of the solution (*e.g.* recirculation) are based on existing experimental or numerical data.

Where there are gaps in literature, such foundational assumptions can be difficult to make, leading to questions regarding their plausibility. The method is also limited to cases where there is no film around the plug.

The two-phase moving-frame-of-reference (Figure 2.6 (b)) is a compromise between single phase moving-frame-of-reference and the fixed-frame-of-reference. The two-phase moving-frame-of-reference works on computational domain smaller than the two-phase fixed-frame-of-reference. It is also more versatile in application compared to the single-phase moving-frame-of-reference, especially where capturing of interface, wall shear and flow recirculation are important (Taha & Cui, 2006a, 2006b). The domain considered captures the interfaces a single plug or multiple plugs and the surrounding flow fields, including the second phase. Several studies of involving heat and mass transfer in bubble and plugs in open channel and microchannels exist (Taha & Cui, 2006a, 2006a; Talimi *et al*, 2012; Deshpande & Zimmerman, 2006). Some studies have used the two-phase fixed-frame with periodic boundary conditions (Boudreaux, 2015; Sarrazin, *et al.*, 2008).

2.4.2 Two-dimensional versus three-dimensional modelling

Two-phase flows can be modelled in two-dimension (2D) as opposed to three-dimension (3D). With appropriate assumptions modelling in 2D simplifies the problem thereby reducing the size of the model and the associated computational costs. A 2D model of flow in a straight channel

resembles that of a flow between two parallel plates. Some investigations have found results of liquid-liquid two-phase flow in square microchannel in 2D to be comparable to 3D (Cherlo, *et al.*, 2010). Appendix A provides a comparison of numerical results for velocity profiles computed for a single-phase flow in rectangular channel with aspect ratio of unity. This profile is compared to a case of flow between parallel plates which is analogous to 2D.

2.4.3 Coupling of variables

Simulations of droplet formation are often undertaken without the inclusion of the mass transport physics due to the numerical expense associated with such coupling. Droplet formation is highly non-linear and involves large changes of the interface topology. In case where two or more aqueous streams are in contact before droplet formation, similar to the study by Tice *et al.* (2003), such a model would provide insight to initial orientation. It is however, suffice to prescribe a model with a discrete droplet with species initialised in particular orientation as, for example, in Tanthapanichakoon *et al.* (2006a). Changes in interface topology when the drop deforms to flow and geometric influences often require inclusion in the model, especially in microchannels with bends or constrictions. The flow fields within moving droplets occur due to viscous drag and have an influence on the mixing inside droplets.

Simulation of mixing dynamics involves solution of the convection-diffusion equation, coupled to that of the flow equation. Mixing in droplets that are travelling in straight microchannel has been studied using CFD by Sarrazin *et al.* (2006). In these studies, a combination of finite volume method and volume-of-fluid were utilised. In other work where the finite element method was utilised, there were lacking details lacked essential details about the modelling aspects of the work (Jiang, *et al.*, 2012). The focus was placed on qualitative comparison with experiments rather than on quantitative results. There is generally sparse literature where simulation of microfluidic problems involving coupling between two-phase flow and species transport is demonstrated.

2.4.4 Quantification of mixing

In order to determine the extent of mixing during numerical simulations various approaches have been adopted. The foundations of are premised on the seminal work by Danckwerts (1952) which quantified mixing as Intensity of Segregation (I_s), expressed as

$$I_s = \frac{\sigma^2}{\sigma_0^2} = \frac{\langle (C - \bar{C})^2 \rangle}{\langle C \rangle (1 - \langle C \rangle)} \quad (2.11)$$

In the above equation, $\sigma^2 = \frac{1}{|V|} \int_V (C - \bar{C})^2 dV$, where V is the control volume, \bar{C} is the mean concentration value in the concentration field and σ_0^2 is a

reference value (Bothe, *et al.*, 2008). Various modifications have since been applied in the quantification of mixing computational fluid dynamics. The Mixing Index (I_M) is a common mixing indicator given by (Bothe, 2010; Jiang, *et al.*, 2012)

$$I_M = 1 - \sqrt{I_s} = \frac{\sigma}{\sigma_{max}} = 1 - \sqrt{\frac{1}{N} \sum_{i=1}^N \left(\frac{\bar{C}_i - \bar{C}_\infty}{\bar{C}_\infty} \right)^2} \quad (2.12)$$

where, N is the total number of sampling points, C_i is the normalised concentration and \bar{C}_∞ is the expected normalised concentration. The index ranges from 0 for no mixing to 1 for complete mixing (Chen, *et al.*, 2016).

For a case where final mixing is expected to be half of the initial concentration *i.e.* $\bar{C}_\infty = 0.5$, the mixing index can be given as (Jiang, *et al.*, 2012):

$$I_M = 1 - 2 \sqrt{\frac{1}{N} \sum_{i=1}^N (C_i - 0.5)^2} \quad (2.13)$$

The simpler approach is integrating in the control volume within the computational domain where mixing is simulated (Tung, *et al.*, 2009):

$$I_M = \left(1 - \frac{\int_V |C_i - C_\infty| dV}{\int_V |C_0 - C_\infty| dV} \right) \quad (2.14)$$

where C_0 is the initial highest concentration and C_i is the initial concentration in the control volume. This approach is simple to compute and grid independent (Muradoglu & Stone, 2005; Stone & Stone, 2005). The technique however does not provide information about the mixing patterns.

2.5 Numerical methods for CFD

2.5.1 Continuum discretisation methods

2.5.1.1 *Finite difference method*

In finite-difference-based schemes, the domain is discretised with a mesh and then a truncated Taylor series expansion is used to approximate each derivative in the governing PDEs. Although finite difference method (FDM) is simple to implement, it cannot easily handle complex geometries, such as with curvilinear boundaries (Wilkes, 2006). It is, therefore, generally not suitable for many flow problems such those involving two-phase dynamics.

2.5.1.2 *Finite volume method*

Also called the control volume method, finite volume method (FVM), is based on the formal control volume integration (Versteeg & Malalasekera, 1996). FVM-based codes have been successfully utilised in the modelling of numerous microfluidics problems, such as studies by Ong *et al.* (2007), Sang *et al.* (2009), Schneider *et al.* (2011) and Mason (2013). This observation

is in contrast to a suggestion by Erickson (2005) that the FVM was not suitable for modelling of typical microfluidic flows which are characterised by low Reynolds numbers and dominant viscous effects. FVM is implemented in several commercial CFD programs, such as Ansys Fluent, Ansys CFX, CFD-ACE+, Flo++, Flow-3D and Star-CCM, as well as Open-source codes such as Open-FOAM. Studies which have demonstrated the application of Open-FOAM in modelling and simulation of two-phase microfluidics also exist (Hoang, *et al.*, 2013).

2.5.1.3 Finite element method (FEM)

Finite element method (FEM) is a well-established discretisation method which is widely used in both structural mechanics and fluid mechanics (Zienkiewicz, *et al.*, 2005). Theoretical and mathematical foundations of FEM are associated with several classical works such as the variational methods for calculus by Lord Rayleigh in 1870 and Walther Ritz in 1909, and the method of weighted-residual by Boris Galerkin in 1915 (Zienkiewicz, *et al.*, 2005). Foundations for modern FEM techniques are attributed to separate works by J. H. Argyris and R. W. Clough and co-workers in the mid-1950s. See Zienkiewicz *et al.*, (2005) for a detailed historical account. The main disadvantage of FEM is that it has much higher requirement for computational resources than FD and FV methods (Wilkes, 2006). The FEM is well-known for being unable to handle discontinuities well. The fact that there are fewer FEM-based CFD commercial software programs, compared to

those underpinned on FVM, is perhaps an indication of the extent of difficulties associated with implementation of the FEM in fluid mechanics. COMSOL Multiphysics™ is one of the few FEM-based commercial CFD programs. An open-source FEM program called FEATFLOW has also been used in modelling multiphase microfluidics (Kashid, *et al.*, 2007).

2.5.1.4 Other methods

Lattice Boltzmann method (LBM) is based on mesoscale modelling and its use has been increasing in studying single-phase, two-phase and multiphase microfluidics (Fu, *et al.*, 2018; van der Graaf, *et al.*, 2006; Zhang, 2011).

In the realm of Lagrangian modelling, particle-based schemes which include dissipative particle hydrodynamics (DPH), smoothed particle hydrodynamics (SPH) and discrete element method (DEM) are also increasingly gaining an interest for investigating microfluidic systems (Filipovic, *et al.*, 2009; Steiner *et al.*, 2009; Shahzad, *et al.*, 2017)

Other numerical schemes in existence consider matter below the continuum limit include and utilise principles of quantum and statistical methods (e.g. molecular dynamics and Monte Carlo simulations) to quantify fluid and interface behaviour. These methods are beyond the scope of the current review.

2.5.2 Implicit methods for evolving fluid interfaces

Continuum methods can be grouped into two distinct classes; (i) the Lagrangian methods which track the interface explicitly and (ii) the Eulerian methods which track the interface implicitly. Within the Lagrangian class, there are two approaches, one of utilising moving meshes and the front tracking of the interface. In Eulerian methods fixed meshes are utilised. Another level of classification is those that use a zero-interface approach and those that have an interface of finite thickness. Figure 2.7 shows a systematic representation of the classes of interface tracking models (Wörner, 2012).

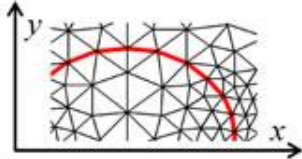
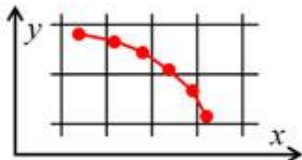
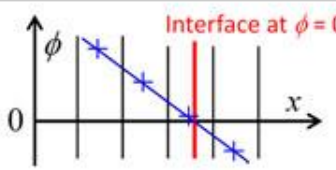
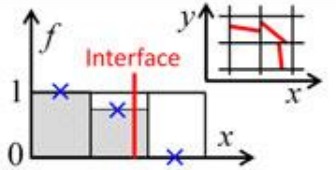
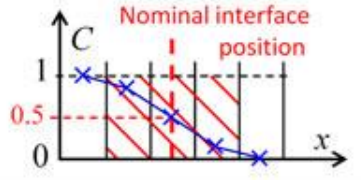
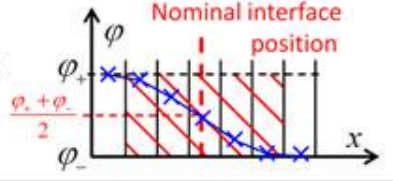
		Interface representation	Interface evolution
Lagrangian type	Moving mesh		Lagrangian movement of interface (unstructured grid)
	Zero interface thickness Front-tracking		Lagrangian movement of interface marker points (•) within structured grid
Eulerian type	Zero interface thickness Level-set		Advection equation for signed distance function ϕ
	Finite interface thickness IR-VOF		Geometric evaluation of phase fluxes across mesh cell faces
	Finite interface thickness CF-VOF and C-LS		Advection Eq. (11) for color function C (in C-LS followed by a compression step)
	Finite interface thickness Phase field		Cahn-Hilliard Eq. (14) for order parameter ϕ

Figure 2.7 Different types of interface methods (Wörner, 2012).

2.5.2.1 *Phase-field method*

In phase field (PF) models, the interface evolution is described by the Cahn-Hilliard equation. There are four possible ways to handle the modelling of the interfacial tension (Hua, *et al.*, 2014). The first method is by using the CSF technique and the other three methods are based on thermodynamic formulations. The property jump in fluid properties across the interface is handled through linear functions (Hua, *et al.*, 2014).

2.5.2.2 *Volume of fluid*

The volume of fluid (VOF) method, similarly to LS and PF, is a popular method for modelling evolution of the interface in two phase flows. Having been introduced in the early 1980s, it is one of the oldest continuum methods for modelling evolution of interface in two-phase flows (Hirt & Nichols, 1981; Youngs, 1982). Due to continued developments and attempts to improve the method, there are several variants of the VOF. The general approach in VOF, called the piecewise linear interface calculation (PLICS), follows on the work by Youngs (1982) and its extensions (Kothe & Rider, 1995). There is also a bigger proportion of commercial CFD software programs that implement VOF method compared to those that implement other competing schemes.

2.5.2.3 Level set method

The traditional level set method (LSM) is a sharp interface (zero-thickness), Eulerian method for modelling the evolution of an interface between two phases (Osher & Sethian, 1988; Sussman, *et al.*, 1994). One of the main advantages of LSM is its ability to handle topological changes and complex interfacial geometries, such as those seen during formation, deformation and splitting of droplets. In LSM, the interface is implicitly represented by the level set (LS) function ϕ and its evolution is governed by the LS transport equation (Sussman, *et al.*, 1994; Hua, *et al.*, 2014). A variant of the LSM, referred to as conservative level set method, was proposed by Olsson and Kreiss (2005). The conservative LSM follows a similar approach to the so-called colour function volume-of-fluid (Wörner, 2012). As with the general LSM, the evolution of the interface is described by a level set equation. The level set function which represents the evolution of the interface changes rapidly from 0 to 1 between the phases as a function of a smoothed Heaviside function. The interface has a nominal value of 0.5 (Olsson & Kreiss, 2005). COMSOL offers both the PF and conservative LSM for modelling two-phase flow. The LSM was chosen in study due to having lower computational demands than PF. The theoretical details of the conservative LSM which is implemented in COSMOL are provided in Chapter 3.

2.5.3 Continuum surface force (CSF)

Numerical tools for modelling two-phase microfluidic flows need to be able to account for the effect of interfacial tension, which exists at the fluid-fluid interface. The continuum surface force (CSF) method models the surface or interfacial tension as a continuum surface force (Brackbill, *et al.*, 1992). With this method, the interfacial tension appears in the Navier-Stokes equation as body force term, rather than as boundary condition. Alternatives to the CSF for modelling interfacial tension are the continuum surface stress (CSS) and the front tracking (FT) methods (Lafaurie, *et al.*, 1994; Tryggvason, *et al.*, 2001). The CSF technique is used mainly in volume of fluid (VOF) and level set (LS), although it will find used in LBM and PF method (Wörner, 2012).

Parasitic or spurious currents are unphysical velocities which can appear at the interface when modelling surface tension at the using CSF and CSS methods (Lafaurie, *et al.*, 1994). The problem of parasitic currents is experienced by most of the continuum methods such LSM, VOF, PF and FT, as well as the mesoscale LBM (Wörner, 2012). Numerical instabilities are to be expected when interfacial tension is a dominant factor is the flow (low Ca values). Factors affecting spurious currents are the capillary number, grid resolution or mesh size, time step and interface thickness (Zahedi, *et al.*, 2012).

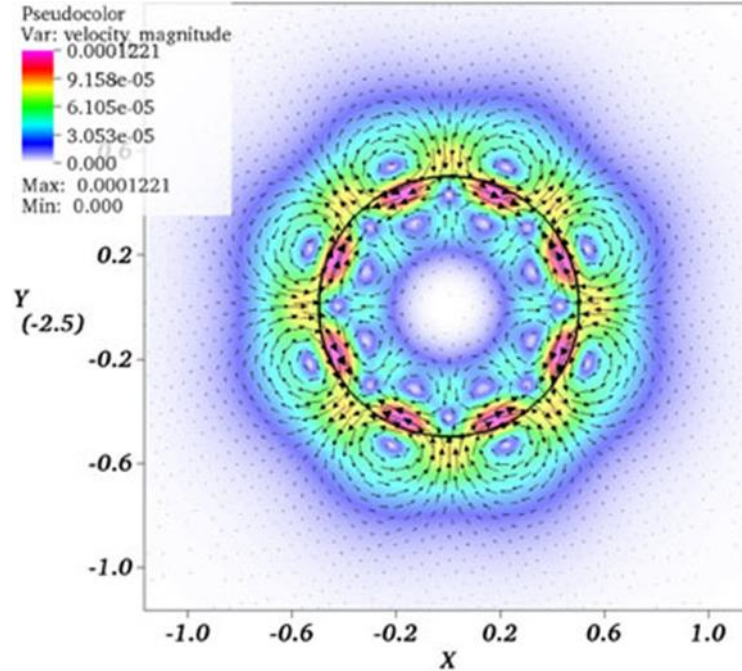


Figure 2.8 Spurious currents around an interface (black line) of a stationary droplet at $Ca=0.1$ (Zahedi, Kronbichler, & Kreiss, 2012).

2.5.4 Validation

There are currently no standardised CFD benchmarking cases for microfluidics. Cases that have been demonstrated in microfluidic studies are used on an *ad hoc* basis. Oberkampf and Trucano (2002) refer to them as ‘weak sense benchmarks’ although they recognise the absence of standard benchmark cases. Standardised benchmark cases are useful in verification and validation of numerical codes and are, generally, set as standards by engineering bodies within the field of CFD. The indication is that the latter scenario seems more prevalent the field of microfluidics.

2.6 Closing remarks

Existing experimental methods for studying and characterising multiphase phenomena in droplet microfluidics are largely based on optical methods, which can be limited due to required specialised and expensive equipment or qualitative nature of some and unsuitability for rugged industrial environments (Aubin, *et al.*, 2010). For example, in characterising microfluidic mixing, specialised techniques, such as LIFM, are required. Optical and colour-based techniques can only provide qualitative information about the mixing. Thus, numerical simulations using computational fluid dynamics (CFD) are attractive and convenient alternatives for studying the fluid and interface dynamics in droplet microfluidics. CFD has, in fact, become synonymous with computer-aided engineering (CAE) functions such as numerical prototyping in microsystems and microfluidics (Erickson, 2005). The so-called ‘in silico’ experiments allow for more flexibility than laboratory experiments and can provide further insight and detail, notwithstanding certain limitations and modelling errors which have to be taken into account, when modelling problems of interest (Zimmerman, 2006).

"God does not care about our mathematical difficulties; He integrates empirically." -- Albert Einstein

Chapter 3

Numerical Modelling Using Finite Element and Level Set Methods

3.1 Introduction

This chapter details the theoretical frameworks of the finite element method (FEM) and level set method (LSM). COMSOL Multiphysics™ employs in its numerical code, FEM as the basic discretisation technique as well as the conservative LSM. The latter applies in the numerical modelling of two-phase flows.

3.1.1 Equations governing two-phase flow

Fluid flow in microfluidic systems occurs within the continuum limit and, therefore, the laws of conservation of energy, mass and momentum are applicable (Kirby, 2010). For isothermal, single-phase Newtonian incompressible flows, the conservation equations simplify to the classical continuity and Navier-Stokes (NS) partial differential equations, given as (White, 2006)

$$\nabla \mathbf{u} = 0 \tag{3.1}$$

$$\rho \left(\frac{\partial \mathbf{u}}{\partial t} + \mathbf{u} \cdot \nabla \mathbf{u} \right) = -\nabla p + \nabla \cdot \mu [\nabla \mathbf{u} + (\nabla \mathbf{u})^T] + \rho \mathbf{g} \quad (3.2)$$

where ρ and μ are viscosity and density of the fluid, respectively; $p = p(\mathbf{x}, t)$ is pressure, \mathbf{g} is gravity, $\mathbf{u} = \mathbf{u}(\mathbf{x}, t)$ is the velocity field, $\mathbf{x} = (x, y, z)$ represents the Cartesian coordinate system and t is a time variable. The superscript T denotes a matrix transpose function. In microfluidic flows involving highly viscous fluids, such as oils, where $Re < 1$ and inertial effects are negligible, the flow is described using Stokes equation

$$\nabla p = \mu \nabla^2 \mathbf{u} \quad (3.3)$$

Consider flow involving two immiscible and incompressible Newtonian fluids (fluid 1 and fluid 2) in an arbitrary domain (Ω) which is separated by a fluid interface Γ , into two subdomains for each fluid ($\Omega = \Omega_j, j = 1, 2$), as illustrated Figure 3.1.

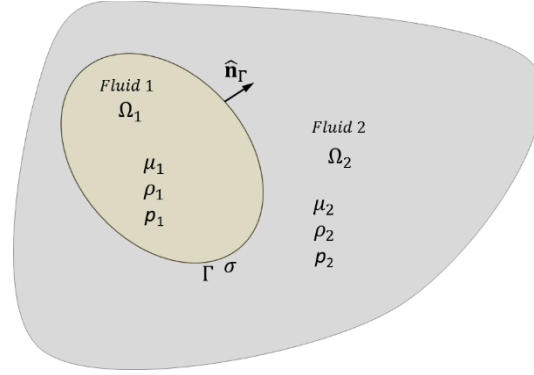


Figure 3.1 Two-phase Newtonian incompressible flow in an arbitrary domain ($\Omega = \Omega_j, j = 1, 2$) which is divided into two by the fluid interface Γ (After Cruanyes, 2014).

The equations of fluid motion for such a flow can be modified to be valid for the respective fluid subdomains as follows (Wörner, 2012):

$$\nabla \mathbf{u}_j = 0 \quad (3.4)$$

$$\rho_j \left(\frac{\partial \mathbf{u}_j}{\partial t} + \mathbf{u}_j \cdot \nabla \mathbf{u}_j \right) = \nabla \cdot \mathbb{S}_j + \rho_j \mathbf{g} \quad (3.5)$$

where $\mathbb{S}_j = -p_j \mathbb{I} + 2\mu_j \mathbb{G}_j$ is a stress tensor, $\mathbb{G}_j = \frac{1}{2} [\nabla \mathbf{u}_j + (\nabla \mathbf{u}_j)^T]$ is a deformation tensor and \mathbb{I} is an identity tensor. The fluid properties (ρ_j, μ_j) are treated as piecewise constant (Wörner, 2012). The property jump at the interface is described by the expressions

$$\llbracket \rho(\mathbf{u} - \mathbf{u}_\Gamma) \rrbracket_\Gamma \cdot \hat{\mathbf{n}}_\Gamma = 0 \quad (3.6)$$

$$\llbracket \rho \mathbf{u} \otimes (\mathbf{u} - \mathbf{u}_\Gamma) - \mathbb{S} \rrbracket_\Gamma \cdot \hat{\mathbf{n}}_\Gamma = \sigma \kappa \hat{\mathbf{n}}_\Gamma + \nabla_\Gamma \sigma \quad (3.7),$$

where \mathbf{u}_Γ is the velocity of the interface, σ is the coefficient of the interfacial tension, $\kappa = -\nabla_\Gamma \cdot \hat{\mathbf{n}}_\Gamma$ is the signed interfacial curvature, and $\nabla_\Gamma = (\mathbb{I} - \hat{\mathbf{n}}_\Gamma \cdot \hat{\mathbf{n}}_\Gamma) \cdot \nabla$ is a surface gradient operator. The symbol $\hat{\mathbf{n}}_\Gamma$ represents a unit vector

normal to the interface (Wörner, 2012). When there is no phase change and no tangential velocity at the interface, the equations become

$$[[\mathbf{u}]]_{\Gamma} = 0 \quad (3.8)$$

$$[[-\mathcal{S}]]_{\Gamma} \cdot \hat{\mathbf{n}}_{\Gamma} = \sigma \kappa \hat{\mathbf{n}}_{\Gamma} + \nabla_{\Gamma} \sigma \quad (3.9)$$

The local NS equation in each field and interface jump condition can be combined into the following set of equations, valid in the entire domain:

$$\rho \left(\frac{\partial \mathbf{u}}{\partial t} + \mathbf{u} \cdot \nabla \mathbf{u} \right) = -\nabla p + \nabla \cdot \mu [\nabla \mathbf{u} + (\nabla \mathbf{u})^T] + \rho \mathbf{g} + \mathbf{F}_{\sigma} \quad (3.10)$$

$$\mathbf{u} = 0 \quad (3.11)$$

The density $\rho = \rho(\mathbf{x}, t)$ and viscosity $\mu = \mu(\mathbf{x}, t)$ are given as piecewise constants in each phase but discontinuous at the interface (Wörner, 2012). The interfacial tension and curvature at the interface between the two fluids are boundary conditions but can be introduced in the NS equations as a body force term $\mathbf{F}_{\sigma} = (\sigma \kappa \hat{\mathbf{n}}_{\Gamma} + \nabla_{\Gamma} \sigma) \delta_{\Gamma}$, where δ_{Γ} is a Dirac delta function.

3.1.2 Mass transport equation

A generic transport equation derived from consideration of an arbitrary control volume V , bounded by a control surface S , is given by (Kuzmin, 2010)

$$\frac{\partial(\rho \bar{c})}{\partial t} + \nabla \cdot (\mathbf{u} \rho \bar{c}) - \nabla \cdot (\mathbb{D} \rho \nabla \bar{c}) = s \quad (3.12)$$

where \bar{c} is an amount per unit mass (mass-specific concentration) and \mathbb{D} is a diffusivity tensor. The physical interpretation of the terms in Equation (3.12)

is given in Table 3.1. The transport equation is coupled to the flow (Navier-Stokes) equations through the velocity field.

Table 3.1 Physical interpretation of terms in the generic transport equation (Kuzmin, 2010)

Term	Description	Physical interpretation
$\frac{\partial(\rho\bar{c})}{\partial t}$	Transient / Rate of change term	Net gain or loss per unit time of mass per unit volume
$\nabla\cdot(\mathbf{u}\rho\bar{c})$	Convective term	Transport of mass by advection due to velocity field \mathbf{u}
$-\nabla\cdot(\mathbb{D}\rho\nabla\bar{c})$	Diffusive term	Spatial dispersion or distribution of \bar{c} , driven by gradients $\nabla\bar{c}$
s	Source term	Combines effects that create or destroy $\rho\bar{c}$

When dealing with incompressible Newtonian flow, the density is constant and the velocity field is divergence free. When the \bar{c} represents the moles per unit mass of chemical species i , the mass variable is written in terms of molar concentration $\rho\bar{c} = C$, the generic transport Equation (3.13) takes the form (Kuzmin, 2010)

$$\frac{\partial C_i}{\partial t} + \mathbf{u}\cdot\nabla C_i - \nabla\cdot(\mathbb{D}_i\nabla C_i) = s \quad (3.13)$$

where C_i is the concentration of the transported chemical species i . For constant mass and spatially independent (isotropic) diffusivity, the equation becomes

$$\frac{\partial C_i}{\partial t} + \mathbf{u} \cdot \nabla C_i - D_i \nabla^2 C_i = s \quad (3.14)$$

where D_i is the mass diffusivity or diffusion coefficient of the transported chemical species i . When there are no effects contributing to the addition or consumption of the chemical species in the system such chemical reaction or phase change, the source term s is eliminated. The mass transport of chemical species is described by the passive scalar diffusion-convection equation (Kirby, 2010)

$$\frac{\partial C_i}{\partial t} + \mathbf{u} \cdot \nabla C_i - D_i \nabla^2 C_i = 0 \quad (3.15)$$

In a non-dimensionalised form, Equation (3.15) becomes

$$\frac{\partial C_i^*}{\partial t^*} + \mathbf{u}^* \cdot \nabla^* C_i^* - \frac{1}{Pe} \nabla^{*2} C_i^* = 0 \quad (3.16)$$

3.2 Finite element method

The finite element method (FEM) has a rich, in-depth mathematics behind it. Standard texts, such as by Zienkiewicz, *et al.* (2005), introduce the fundamentals of FEM while detailing the underlying mathematics with due rigour. An introduction with relevance to fluid mechanics is given by Zienkiewicz and Taylor (2000). Thus, the current discussion does not attempt to provide a comprehensive mathematical introduction to FEM, but to rather to detail its salient features. The current discussion is based, mainly, on an introductory text by Kuzmin (2010) and focusses on the Galerkin FEM. Exact solutions for PDEs describing physics in many industrial and engineering problems are nearly impossible to obtain. A system of algebraic equations can be solved with relative ease and speed using computers. FEM is a numerical technique which can be used to obtain approximate solutions.

3.2.1 Initial and boundary conditions

Consider an arbitrary domain $\Omega \subset \mathbb{R}^e, e = 1,2,3$ which is bounded by a boundary surface $\partial\Omega$. Suppose the prevailing physics is governed by convection-diffusion PDE which describes transport of an arbitrary scalar variable u

$$\frac{\partial u}{\partial t} + \nabla \cdot (\mathbf{u}u) - \nabla \cdot (\mathcal{D}\nabla u) = s \quad (3.17)$$

where \mathcal{D} is a diffusivity coefficient and s is a source term. In order for the problem to be well posed, initial and boundary conditions are imposed. The

initial condition at time zero is prescribed as $u(\mathbf{x}, 0) = u_0$. A Dirichlet boundary condition is imposed if u values can be prescribed on boundary section $\partial\Omega_D \subset \partial\Omega$, such that $u(\mathbf{x}, t) = u_D(\mathbf{x}, t)$ for $\mathbf{x} \in \partial\Omega$. The Neumann boundary condition $\mathbf{f} \cdot \mathbf{n} = g(\mathbf{x}, t)$ for $\mathbf{x} \in \partial\Omega$ may be imposed on a complementary boundary $\partial\Omega_N = \partial\Omega/\partial\Omega_D$, where \mathbf{f} is the convective or diffusive flux (Kuzmin, 2010).

3.2.2 Weighted residual formulation

Conventional Galerkin FEM approximations are based on the method of weighted residuals, a general approach for deriving a weak or integral form of a PDE (Kuzmin, 2010). Essentially, the conservation PDE is converted into an integral equation. Since there is no general solution to the PDE, an approximate solution $\hat{u} \approx u$ is then sought. The residual of the equation is

$$\mathfrak{R}(\hat{u}) = \frac{\partial \hat{u}}{\partial t} + \nabla \cdot (\mathbf{u}\hat{u}) - \nabla \cdot (\mathcal{D}\nabla \hat{u}) - s \quad (3.18)$$

where $\mathfrak{R}(\hat{u})$ is the measure of accuracy of the approximate solution. When $\mathfrak{R}(u) = 0$, the original PDE is obtained. Use of weighting functions, followed by derivation, the weak form of Equation (3.18) is expressed as (Kuzmin, 2010):

$$\begin{aligned} & \int_{\Omega} \left(w \frac{\partial u}{\partial t} - \nabla w \cdot (\mathbf{u}u - \mathcal{D}\nabla u) - ws \right) dx \\ & + \int_{\partial\Omega_N} w (\mathbf{u}u - \mathcal{D}\nabla u) \cdot \mathbf{n} ds = 0 \end{aligned} \quad (3.19)$$

where $w \in \mathcal{W}$ is a weighting or test function, to which $\mathfrak{R}(u)$ is orthogonal and \mathcal{W} is a space of weighting functions vanishing on $\partial\Omega_D$. The weak solution u resides in space function \mathcal{V} such that $u \in \mathcal{V}$, satisfying Dirichlet boundary conditions. The corresponding integral equation satisfying the Neumann boundary conditions is

$$\int_{\partial\Omega_N} w \mathbf{f} \cdot \mathbf{n} \, ds = \int_{\partial\Omega_N} w g \, ds \quad (3.20)$$

3.2.3 Spatial discretisation

The computational domain Ω is discretised by triangulation whereby its area is divided into multiple triangular subdivisions or elements Ω_k . The subdivisions are put together such that $\Omega \approx \cup_k \Omega_k$. The number of unknowns to be solved across all the nodes in a given computation of a model are referred to as degrees of freedom (DOF). In the case of a two-dimensional domain ($\Omega \subset \mathbb{R}^2$) as shown in Figure 3.2, triangular or quadrilateral elements are used. Unstructured meshes are easy to generate and are generally flexible for a wide range of geometries. The disadvantage of unstructured meshes is that they often require sophisticated algorithms to handle irregular connectivity patterns, which translates to high computational cost (Kuzmin, 2010).

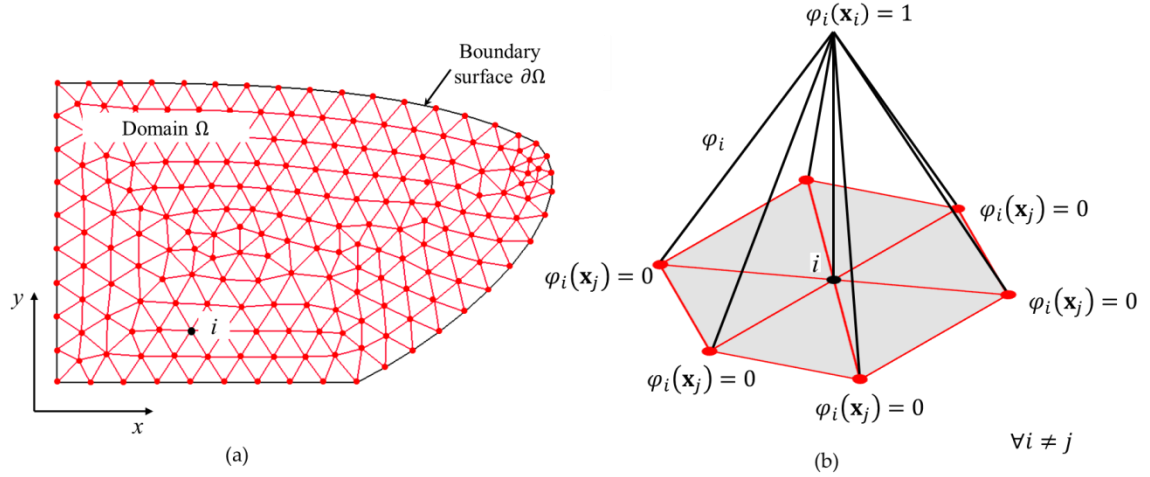


Figure 3.2: (a) Discretisation of 2D arbitrary domain by triangulation, (b) Node i and neighbouring triangular elements, with a linear shape function φ (Adapted from Wilkes, 2006).

3.2.4 Galerkin method

The approximate solution to u in discrete form is given by

$$u \approx u_h = \sum_{i=1}^n u_i(t) \varphi_i(\mathbf{x}) \quad (3.21)$$

where u_i are variables to be determined and φ_i represents basis functions in the finite dimensional space \mathcal{V}_h and determined the nodes \mathbf{x}_i which are spatially located either at the vertices of the mesh (*vertex-based method*). The restriction on nodal functions is that $\varphi_i(\mathbf{x}_i) = 1$ and $\varphi_i(\mathbf{x}_j) = 0$ and for all cases $i \neq j$. A test function ψ_i is located in the finite dimensional space \mathcal{W}_h . The key feature of the conventional Galerkin method is that trial functions and test functions are taken from the same space $\mathcal{V}_h = \mathcal{W}_h$, such that $\varphi_i = \psi_i$. Therefore, the number of equations equals the number of unknowns

(Kuzmin, 2010). The discretisation will lead to a system of algebraic equations of the form

$$\boldsymbol{\alpha}\boldsymbol{\beta} = \mathbf{b} \quad (3.22)$$

Where $\boldsymbol{\alpha}$ is a sparse matrix, $\boldsymbol{\beta}$ is a vector of unknowns and \mathbf{b} is a solution matrix computed from previously computed data.

3.2.5 Numerical solvers

In numerical analysis, physics problems can, generally, be solved in either transient (time-dependent) state or steady state. The latter case requires stationary solvers and time-dependant solvers work for transient problems. The COMSOL package provides for implementation of stationary, time-dependent and eigenvalue solvers (Comsol AB, COSMSOL Multiphysics 3.5a User's Guide, 2008a). A parametric solver is also offered for parameterised stationary and eigenvalue problems. COMSOL has several direct linear solvers for linear systems, as well as iterative solvers for more complex and memory-intensive problems.

The direct solvers include PARDISO (Parallel direct solver), SPOOLES (Sparse object-oriented linear equations solver), UMFPACK (Unsymmetric multifrontal package) and Cholesky solver (Comsol AB, COSMSOL Multiphysics 3.5a User's Guide, 2008a). Only PARDISO and UMFPACK were considered for the current work due to their efficiency in solving non-symmetric systems. PARDISO is also suitable for symmetric problems and

utilises less computer memory than UMFPACK (Comsol AB, COSMSOL Multiphysics 3.5a User's Guide, 2008a). Direct solvers are ideal for models with low number of mesh elements, typically in one or two space dimensions. Direct solvers can, however, be applied to 3D models with DOF of up to 10^6 depending on available computational resources and memory. The Gaussian elimination technique implemented in direct solvers is reliable and stable, making it also suitable for ill-conditioned problems (Comsol AB, COSMSOL Multiphysics 3.5a User's Guide, 2008a). However, the elimination process can have extensive memory requirements, particularly for 3D problems or those where the DOF exceeds 10^5 .

Iterative solvers are more memory efficient than direct solvers are better suited in cases where the latter do adequately perform. Non-symmetric problems generally require iterative solvers which also handle such systems better than the direct solvers (Comsol AB, COSMSOL Multiphysics 3.5a User's Guide, 2008a). Iterative solvers that are implemented in COMSOL are GMRES (Generalized minimal residual method), FGMRES (Flexible generalized minimal residual method), BiCGStab (Biconjugate gradient stabilized method) and Geometric multigrid. GMRES is non-symmetrical problems while FGMRES can handle more general preconditioners but uses more memory than GMRES. BiCGStab uses a fixed amount of memory regardless of number iterations. Geometric multigrid is suitable for elliptic and parabolic problems.

Iterative solvers typically require pre-conditioners although solutions can be attempted without pre-conditioning. Selection of preconditioners influences the number of iterations and the convergence of the solution (Comsol AB, COSMOSOL Multiphysics 3.5a User's Guide, 2008a). The COMSOL preconditioners include Algebraic Multigrid, Geometric Multigrid, Incomplete Cholesky (TAUCS) and Incomplete LU (lower-upper). The latter is suitable for non-symmetric problems and together with the multigrid preconditioners were considered to be useful for the current study. The multigrid preconditioners are useful for elliptic and parabolic problems and also suitable for problems with loosely-coupled physics.

3.2.6 Numerical stabilisation using artificial diffusion

FEM as discretisation method performs well when applied to elliptic and parabolic problems at low Peclet numbers (Kuzmin, 2010). However, for cases where $Pe \rightarrow \infty$, the solution becomes unstable (oscillatory) and the outcome erroneous (Zienkiewicz & Taylor, 2000). It is useful to monitor the Peclet number within the elements of computational mesh to determine the stability of the solution. The element Peclet number is given by

$$Pe_{\hbar} = \frac{\|\mathbf{u}\|\hbar}{2D} \quad (3.23)$$

where \hbar is the mesh element size in metres. Generally, when $Pe_{\hbar} \leq 2$ the solution will be resolved without a need for stabilisation (Kuzmin, 2010). Large Pe_{\hbar} values are indicative of coarse meshes, large velocities or small

diffusion. Mesh refinement can be implemented to stabilise solution. However, this can be achieved at increased computational cost. The norm is to implement artificial diffusion. The three classes of artificial diffusion implemented in COMSOL are, isotropic, crosswind and streamline diffusion. Isotropic diffusion applicable to homogenous flow-fields and is not applicable to two phase flow. The streamline methods are of three types, namely; anisotropic, streamline upwind Petrov-Galerkin (SUPG) and Galerkin least-squares (GLS). In certain problems characterised by dominance of convection, the SUPG and GLS methods can themselves cause instabilities which cannot be eliminated by mesh refinement (John & Knobloch, 2008). The selection of correct artificial diffusion and tuning often requires meticulous detail as dictated by the problem at hand.

3.3 Conservative level set method

The level set method (LSM) implemented in the current work is a conservative variant for modelling two-phase flow based on the work by Olsson and Kreiss (2005).

3.3.1 Modelling of the evolution of fluid interface

The interface between fluids evolves due to fluid mechanics, and is governed by the level set transport equation, given by (Sussman, *et al.*, 1994)

$$\frac{\partial \phi}{\partial t} + \mathbf{u} \cdot \nabla \phi = 0 \quad (3.24)$$

where the interface is represented by the level set function $\phi = \phi(\mathbf{x}, t)$, and is initialised as a certain distance from the interface which satisfies a condition of the distance function, $|\nabla\phi| = 1$. The level set equation incompressible flow can be written in the following conservative form:

$$\frac{\partial\phi}{\partial t} + \nabla \cdot (\mathbf{u}\phi) = 0 \quad (3.25)$$

where ϕ has an assigned value of 0.5 at the interface and changes rapidly from 0 to 1 between the phases as a function of a smoothed Heaviside step function (Olsson & Kreiss, 2005).

$$\phi = \mathcal{H}_{sm}(\phi_{sd}) = \begin{cases} 0, & \phi_{sd} < -\varepsilon \\ \frac{1}{2} + \frac{\phi_{sd}}{2\varepsilon} + \frac{1}{2\pi} \sin\left(\frac{\pi\phi_{sd}}{\varepsilon}\right), & -\varepsilon \leq \phi_{sd} \leq \varepsilon \\ 1, & \phi_{sd} > \varepsilon \end{cases} \quad (3.26)$$

where ϕ_{sd} is a signed distance function:

$$\phi_{sd}(x) = \min_{x_\Gamma \in \Gamma} (|x - x_\Gamma|) \quad (3.27)$$

The ε parameter represents interface thickness where ϕ smoothly transitions from 0 to 1, and is typically specified to be approximately equal to half the size of mesh (Zahedi, *et al.*, 2012). Figure 3.3 shows the implementation of the level set between two fluid phases and how $\mathcal{H}_{sm}(\phi_{sd})$ transition smoothly across the interface.

3.3.2 Interfacial tension

The interfacial tension is modelled using the continuum surface force (CSF) method (Brackbill *et al.*, 1992). The interfacial tension appears in the Navier-Stokes equation as body force, \mathbf{F}_σ , as expressed by Equation (3.10), rather than as a boundary condition. The interface normal vector and interface curvature are given as (Wörner, 2012)

$$\hat{\mathbf{n}}_\Gamma = \frac{\nabla\phi}{|\nabla\phi|} \quad (3.28)$$

$$\kappa = -\nabla \cdot \hat{\mathbf{n}}_\Gamma = -\nabla \cdot \left(\frac{\nabla\phi}{|\nabla\phi|} \right) \quad (3.29)$$

Therefore, \mathbf{F}_σ is expressed using a diffuse interface approach as

$$\mathbf{F}_\sigma = \sigma\kappa\delta_{sm}\hat{\mathbf{n}}_\Gamma \quad (3.30)$$

where δ_{sm} is a smoothed Dirac delta function, which in the current work is implemented in COMSOL Multiphysics™ as

$$\delta_{sm}(\phi) = 6|\nabla\phi||\phi(\phi - 1)| \quad (3.31)$$

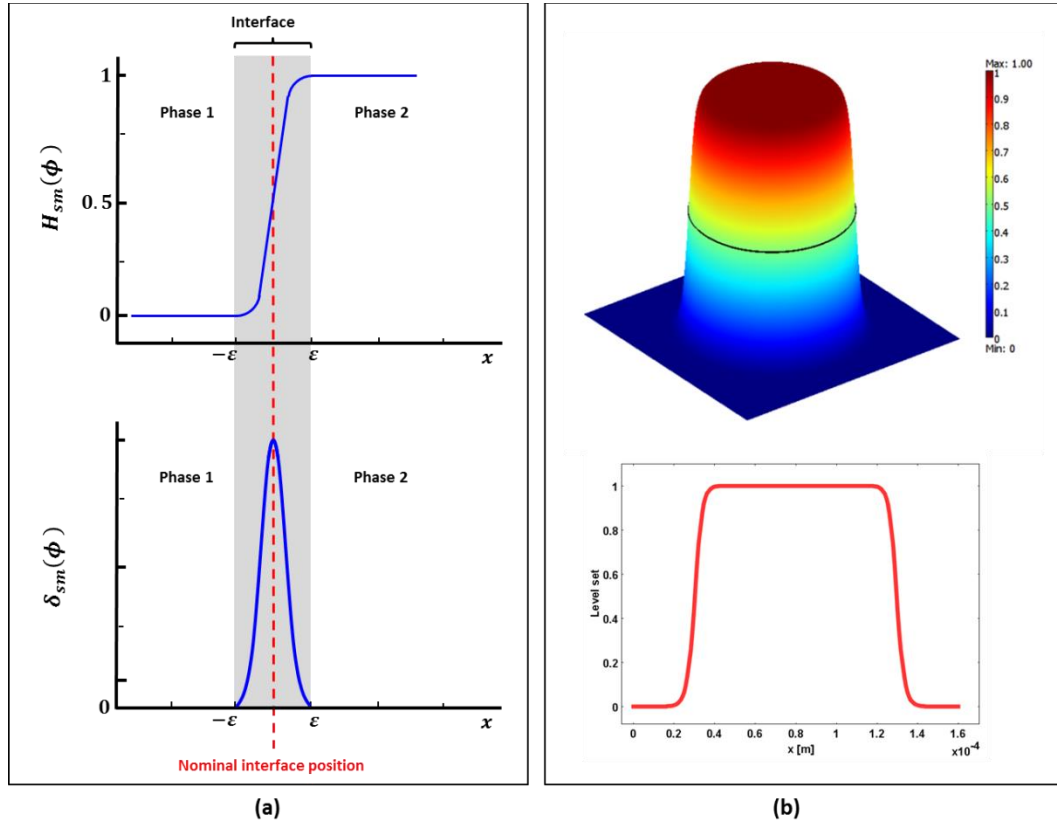


Figure 3.3 Level set for a 2D droplet varying smoothly between 0 and 1. (a) In the height contour data, the interface is represented by the black line contour equal to 0.5; (b) The red line shows how the interface varies, as described in the x -direction.

The density and viscosity constants are varied smoothly across the interface using

$$\rho = \rho_2 + (\rho_1 - \rho_2)\phi \quad (3.32)$$

$$\mu = \mu_2 + (\mu_1 - \mu_2)\phi \quad (3.33)$$

Numerical tools to be used in two-phase microfluidic flows need to be able to account for the effect of interfacial tension. The interfacial tension is a dominant effect, due to small length scales and low velocity flows, as can be seen from low capillary numbers.

3.3.3 Interface re-initialisation

A re-initialisation equation is then solved as a second step until steady state (Zahedi, *et al.*, 2012)

$$\frac{\partial \phi}{\partial \tau} + \nabla \cdot [\phi(1 - \phi)\hat{\mathbf{n}}_{\Gamma}] = \nabla \cdot [\varepsilon(\nabla \phi \cdot \hat{\mathbf{n}}_{\Gamma})\hat{\mathbf{n}}_{\Gamma}] \quad (3.34)$$

where ε is a parameter included to avoid discontinuities at the interface by controlling the interface thickness and the amount of diffusion in the normal direction (Zahedi, *et al.*, 2012).

"Essentially, all models are wrong, but some are useful."--George E. P. Box & Norman R. Draper

Chapter 4

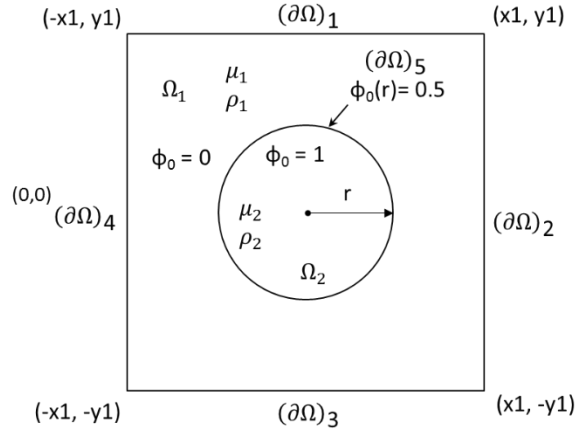
Benchmark Computations and Validation

4.1 Introduction

A numerical model is an approximate representation of exact physics, and as such, the veracity and the usefulness of such a model needs to be interrogated. When modelling two-phase flow with LSM, there are important factors such as conservation of mass, existence of spurious currents at the interface, effect of the interface thickness, and mesh size which must be considered. These factors have a bearing on the accuracy of the results. Stable use of FEM in solving convection-diffusion problems is constrained to mesh Peclet numbers below the value of 2, else it becomes necessary to implement stabilisation techniques, which could also influence the accuracy of the solution. This chapter addresses aspects relating to the reliability of simulation results from COMSOL Multiphysics™ as tested by validation. Validation is essential to indicate whether the correct equations are solved with acceptable accuracy (Roache, 1997). Benchmarking computations were performed on a set of problems, which were also tested against well-known analytical and experimentally-validated theoretical models.

4.2 Two-dimensional stationary droplet

The first case for validation is the stationary neutrally-buoyant droplet, which has the Young-Laplace equation as an analytical solution (van der Graaf, *et al.*, 2006). The droplet was simulated in a two-dimensional (2D) domain. A range of interfacial tensions from high to low was evaluated in a range of micron-size droplets. Figure 4.1 shows the numerical set-up of the 2D stationary droplet case with subdomain and boundary conditions.



Subdomains

Fluid 1 ($\phi_0 = 0$)

Fluid 2 ($\phi_0 = 1$)

Boundary conditions (BCs)

Symmetry (BCs 1 – 4): $\mathbf{n} \cdot \mathbf{u}$, $\mathbf{t} \cdot [-p\mathbb{I} + \mu(\nabla\mathbf{u} + (\nabla\mathbf{u})^T)]\mathbf{n} = 0$

Initial fluid interface (BC 5): $\phi_0 = 0.5$, $[-p\mathbb{I} + \mu(\nabla\mathbf{u} + (\nabla\mathbf{u})^T)]\mathbf{n} = 0$

Figure 4.1 2D computational domain of the stationary droplet consisting of two fluid sub-domains Ω_1 and Ω_2 .

The droplet was centred at (0,0) and the domain was set up such that $x_1 = y_1$ and $r/x_1 = 0.625$. The viscosity and density ratios were both kept at unity ($\rho = 1000 \text{ kg/m}^3, \mu = 0.005 \text{ Pa} \cdot \text{s}$). Symmetry boundary conditions were specified for the four peripheral edges of the domain (BC 1 – BC 4) and initial fluid interface specified for the droplet edge (BC 5).

The factors affecting accuracy, spurious currents and mass conservation were quantified. The parameters which were used to quantify were the relative error of pressure in relation to the exact analytical solution, the magnitude of the parasitic currents, and area conservation of the droplet by the level set. The exact solution for the pressure difference across the interface as described by the Young-Laplace law in a two-dimensional space is expressed as

$$\Delta p_{exact} = \frac{\sigma}{r} \quad (4.1)$$

The relative error (E_r) from the numerical solution is determined from

$$E_r = \frac{|\Delta p_{exact} - (p_{in} - p_{ext})|}{\Delta p_{exact}} \times 100 \quad (4.2)$$

Since the exact solution for the velocity is zero, any velocities in the flow field are considered to be spurious currents (Zahedi, *et al.*, 2012). The magnitude (U_p) of the of the spurious currents as the maximum norm of the velocity field

$$U_p = \|\mathbf{u}\|_{\infty} \quad (4.3)$$

The performance of the method in conserving mass is determined by checking the reduction (or increase) in the droplet area

$$A_{loss} = \frac{A_{exact} - A_{\phi}}{A_{\phi}} \times 100 \quad (4.4)$$

where $A_{exact} = \pi r^2$ is the area of the initially specified for the droplet. The area of the droplet as defined by the level set is determined by integrating the area covered by $\phi > 0.5$ over the whole domain using the expression

$$A_{\phi} = \int_{\phi > 0.5} d\Omega \quad (4.5)$$

4.2.1 Spatial grid resolution

The mesh independence was evaluated on a droplet of radius $r = 50 \mu\text{m}$ by computing solutions from grids of different sizes. Two criteria were used to evaluate the importance of the grid: the exact solution for pressure and the spurious currents (Zahedi, *et al.*, 2012). Six grid sizes (Figure 4.2) were set up using the automatic mesh sizing function. The number of mesh elements was increased using built-in commands for generating grids and refinement, as shown in Table 4.1. The grid sizes of A to D were automatically generated. Mesh E was generated by refining D. F was generated from mesh E refinement.

Table 4.1 Parameters for the six different meshes evaluated.

Grid	Sizing command	No. of nodes	No. of elements	Max. size [m]	Min. size [m]	Min. quality	Element area ratio	DOF
A	Coarse	190	338	$1.90 \cdot 10^{-5}$	$7.69 \cdot 10^{-6}$	0.8597	0.1851	2341
B	Normal	395	728	$1.27 \cdot 10^{-5}$	$6.38 \cdot 10^{-6}$	0.8537	0.2585	4946
C	Finer	1136	2158	$7.37 \cdot 10^{-6}$	$3.31 \cdot 10^{-6}$	0.8608	0.2201	14423
D	Extrafine	3813	7424	$4.06 \cdot 10^{-6}$	$1.802 \cdot 10^{-6}$	0.8860	0.1833	48960
E	Refine (D)	15049	29696	$2.03 \cdot 10^{-6}$	$9.16 \cdot 10^{-7}$	0.8860	0.1833	194428
F	Refine (E)	59793	118784	$1.01 \cdot 10^{-6}$	$4.51 \cdot 10^{-7}$	0.8860	0.1833	774900

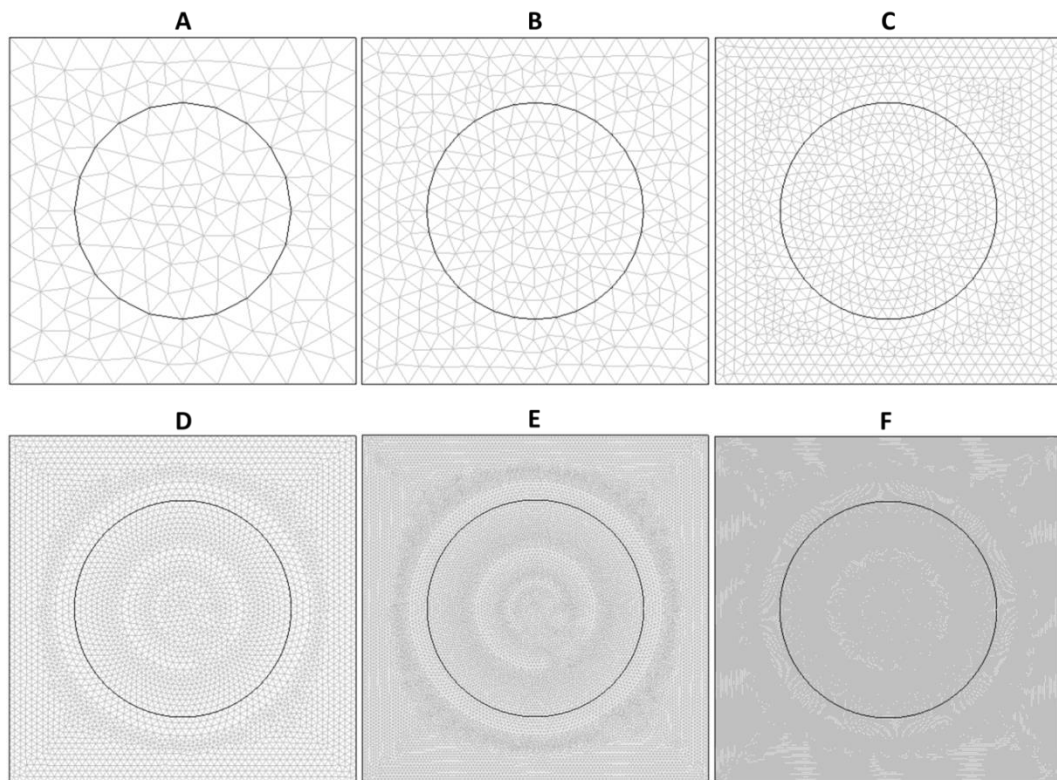
**Figure 4.2** Six types meshes of various sizes.

Figure 4.3 shows the surface pressure on the domain as computed using the different grids. Figure 4.5 shows corresponding linear pressure profiles across the droplet for the different mesh sizes. These results show that with progressively finer meshes, the pressure jump across the interface becomes more pronounced (less diffuse).

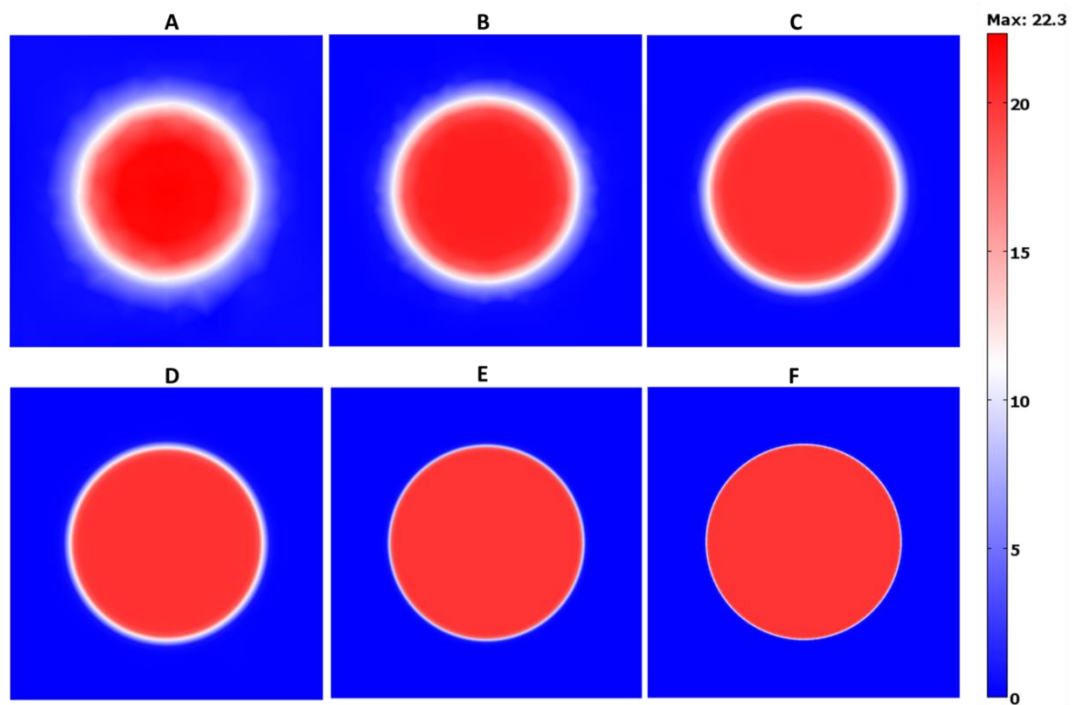


Figure 4.3 Surface plots of pressure (in Pa) fields corresponding to the different meshes.

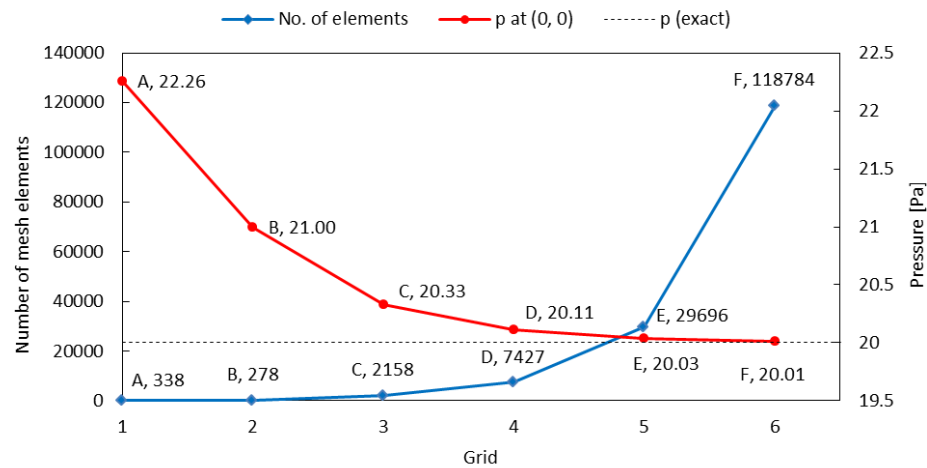


Figure 4.4 Graphs showing relation between the number of mesh elements and the numerical pressure at the centre of the droplet. The horizontal line shows the exact analytical solution.

The pressure value from grids C and D were both within 2% of the analytical solution and the difference between them was below 1.5%. The profile of the pressure across the interface still spread out significantly, as shown in Figure 4.5(a). Even though the grid F was considerably more refined than grid E, having approximately 4 times as many grid points, the cross-sectional profiles of the pressure and performance of the two grids were similar (see Figure 4.5 and Table 4.2).

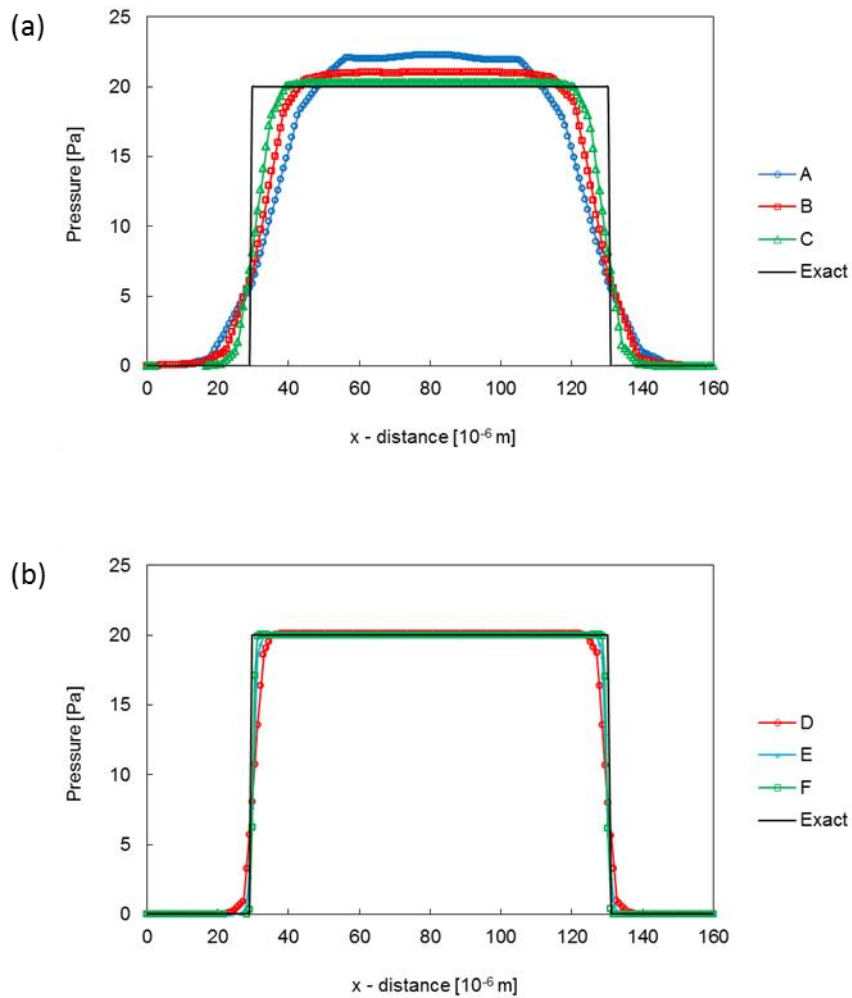


Figure 4.5 Overlays of pressure profiles across the middle of the droplet, showing variations across the interface between the different grids (a) A-C and (b) D-F

The plots of the cross-sectional profiles of the pressure and the fluid interface in Figure 4.6 show that there is a correlation between the smearing of the interface with that of pressure across the interface.

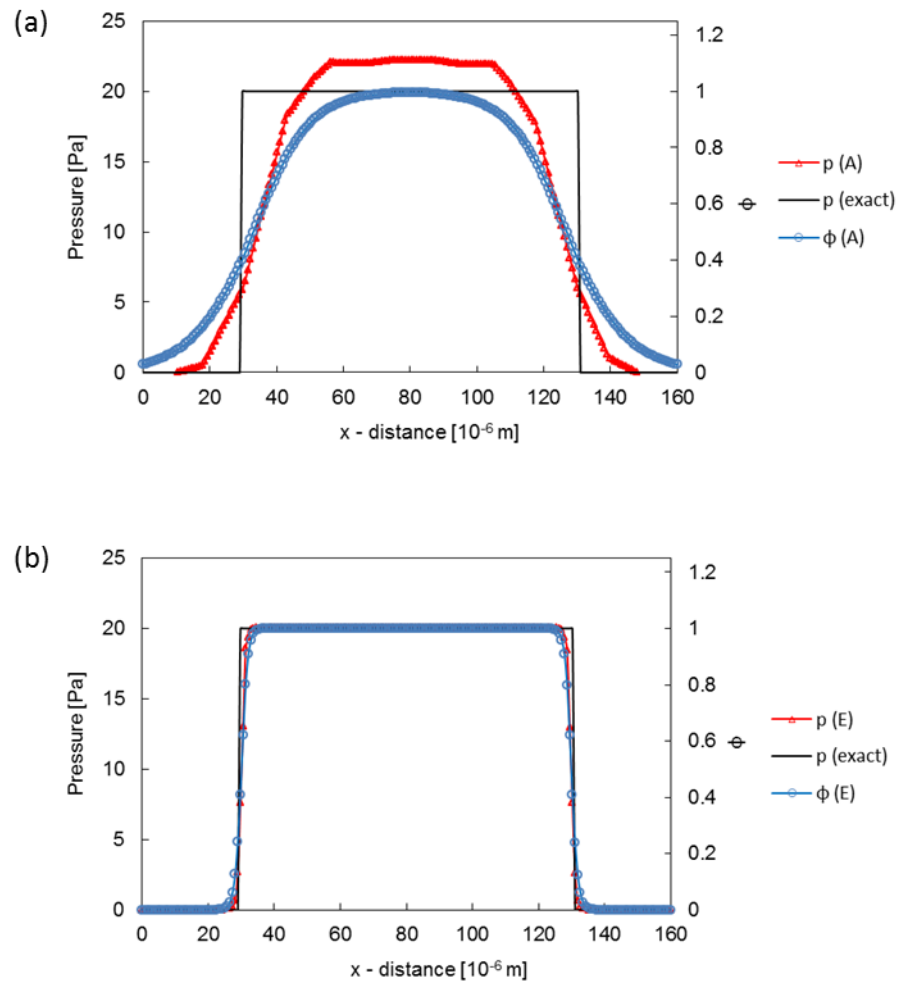


Figure 4.6 Cross-sections of pressure and the fluid interface along a horizontal line through the middle of the droplet computed using grid (a) A and (b) E, compared to the exact solution for pressure.

The surface and arrow plots of the velocity field in Figure 4.7 demonstrate an increased magnitude of spurious currents in a coarse mesh (A) which diminish by an order of magnitude in a refined mesh (E). The sizes of the

arrows in the plot are proportional to maximum velocities in each case and do not represent relative magnitude between the two cases.

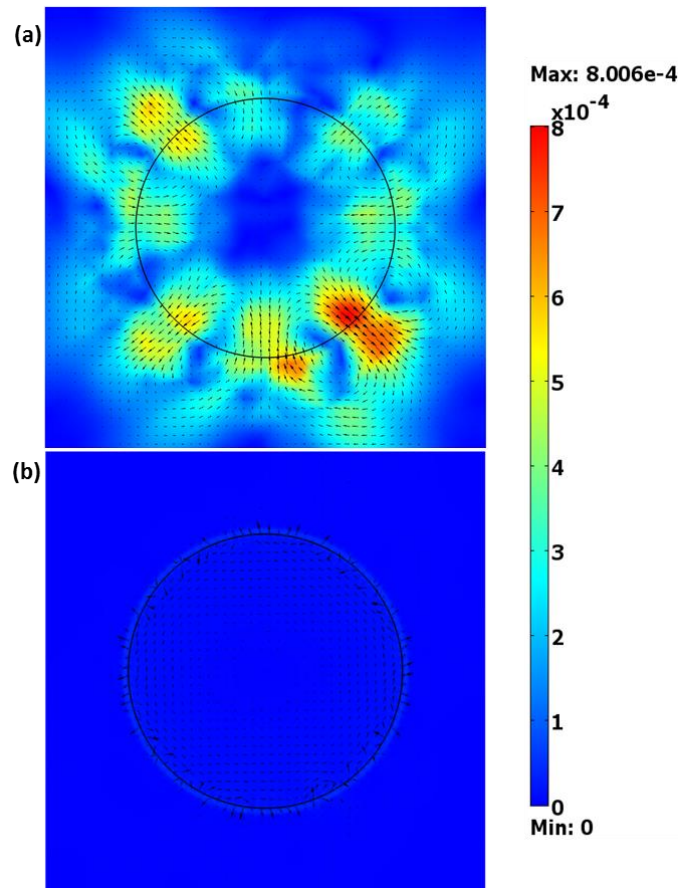


Figure 4.7 Reduction in parasitic currents by mesh refinement between (a) mesh A and (b) mesh E. The computed fluid interface is indicated with the black circle. The units for velocity are m/s.

The results in Table 4.2 indicate that the magnitude to the spurious currents will reduce with refinement of the spatial mesh. This observation is consistent with previous studies (Renardy & Renardy, 2002; Zahedi, *et al.*, 2012).

Table 4.2 Performance of the different spatial meshes as determined through the parameters E_r , U_p and A_{loss}

Mesh	E_r	U_p [m/s]	A_{loss}
A	11%	8.01×10^{-4}	13.6%
B	5.0%	5.64×10^{-4}	9.3%
C	1.7%	2.48×10^{-4}	<0.01%
D	0.6%	8.82×10^{-5}	1.14%
E	0.2%	5.50×10^{-5}	<0.01%
F	0.1%	8.03×10^{-5}	<0.01%

The grid size in E was then used in the modelling of droplets in different sizes and further analysis. The capability of measuring the pressure difference at different interfacial tensions at each of the droplet size was determined.

4.2.2 Interface thickness

The parameter controlling the interface thickness in the level set equation (3.3) was varied proportionally to size of the maximum mesh spacing (h_{max}) to investigate the effect of a thin ($\varepsilon < h_{max}$) or thick ($\varepsilon > h_{max}$) interface. The interface that is set too thin ($\sim \varepsilon \leq 0.25 h_{max}$) or too thick ($\sim \varepsilon \leq 4 h_{max}$) shows an adverse influence in at least two of the parameters in Table 4.3. The thick interfaces exhibits more mass loss (almost 10%) while the thin interface

($\sim \varepsilon \leq 0.25h_{max}$) shows a spike in the magnitude of the spurious currents to $\mathcal{O}(10^{-2})$.

Table 4.3 E_r , U_p and A_{loss} for 100 μm droplet for different interface thicknesses a determined at $\Delta t = 10^{-5}$ and $h_{max} = 2.03 \times 10^{-6}$.

ε [m]	E_r	U_p [m/s]	A_{loss}
$4h_{max}$	7.2%	3.03×10^{-4}	9.3%
$2h_{max}$	1.3%	1.71×10^{-4}	2.8%
h_{max}	0.5%	1.37×10^{-4}	1.5%
$h_{max}/2$	0.2%	5.50×10^{-5}	<0.01%
$h_{max}/4$	7.5%	9.22×10^{-3}	0.70%

The relative errors on the computed pressure differential show an increase as the interface is thickened or thinned to $\sim 7.5\%$ for $4h_{max}$ and $0.25h_{max}$. The latter value can be misleading, as the cross-sectional profile of the pressure in Figure 4.8(a) shows an erratic behaviour at the interface with inaccuracies that spike to nearly an order of magnitude from the exact value. The pressure profile of the erratic behaviour corresponds to the profile of the interface in Figure 4.8(c), which also shows the inaccuracies in the neighbourhood of the interface. The pressure profile in the case of interface with twice the thickness ($\varepsilon = 0.5h_{max}$) has good fit with the profile of the exact solution. This prescription for ε is recommended for controlling the thickness of the interface in COMSOL. As demonstrated by the results in Table 4.3, interface thickness of $\varepsilon = 0.5h_{max}$ provides good performance in conjunction with a

sufficiently refined spatial mesh ($h_{max} = 2.03 \times 10^{-6}$). Figure 4.8(b) and Figure 4.8(c) demonstrate the previously highlighted resemblance between the cross-sectional profiles of the pressure and interface. A large value of ε results in a diffuse interface and the corresponding pressure profile is also diffuse.

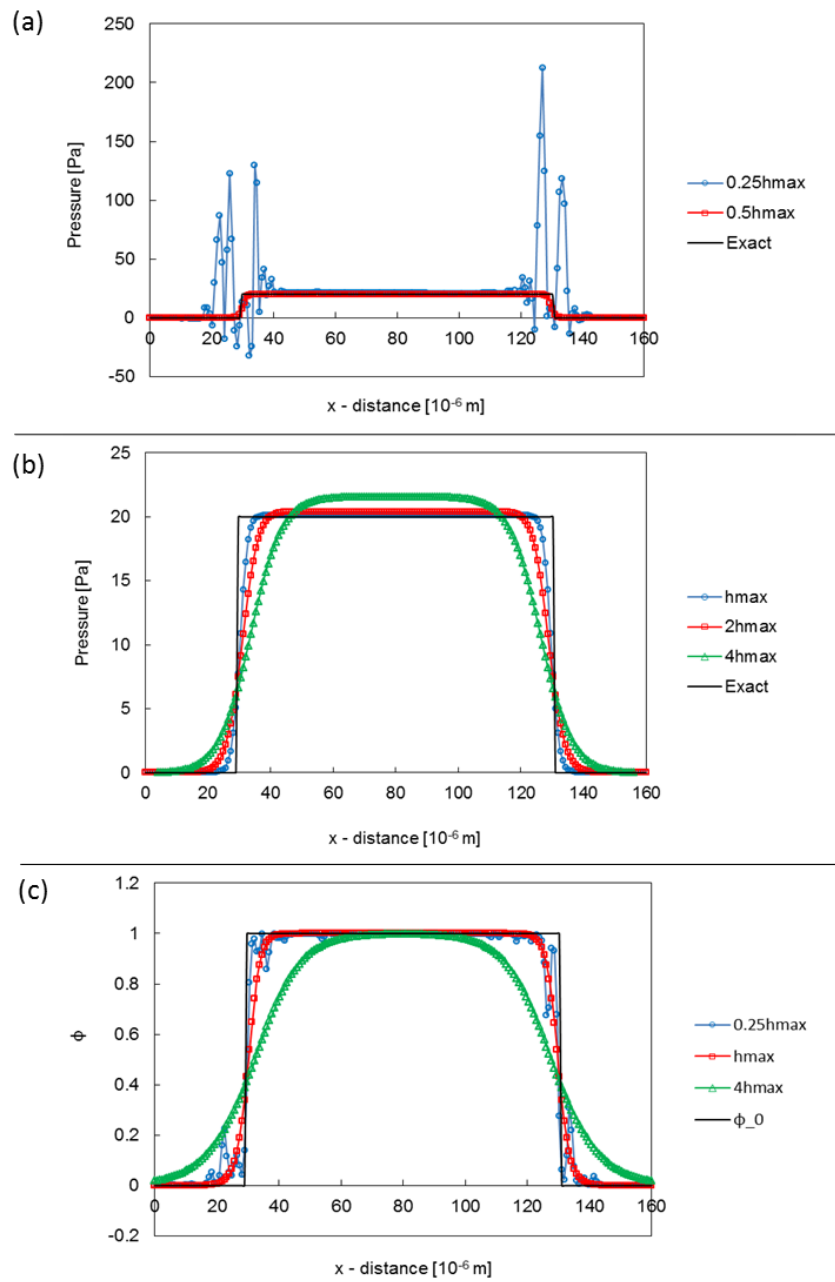


Figure 4.8 (a) Cross-sectional profiles of (a)-(b) pressure and (c) interface, along a horizontal line through (0,0) the middle of the droplet for different value of ϵ as a factor of h_{max} . The cross-sectional profile of the exact solutions and initial interface are plotted.

4.2.3 Time step

The stability of the solution in the presence of parasitic currents was evaluated via the Courant-Friedrichs-Lewy (CFL) number, or Courant number, calculated based on the U_p value and a selected time step

$$CFL_p = U_p \frac{\Delta t}{h_{max}} \quad (4.6)$$

Table 4.4 shows the results of E_r , U_p , A_{loss} and CFL_p as a result of time step Δt . Reduction of the time step Δt resulted in a positive benefit until a certain limit, beyond which the accuracy of the results and presence of the parasitic currents are determined by the spatial grid resolution. The results also demonstrate that very large time steps can result in increased magnitude to the parasitic currents, even though there is no significant error or mass loss. The significance of the results is that reasonably large time steps ($\sim 5 \times 10^{-4} s$) can be taken when the spatial mesh is of sufficient resolution provided the interface remains unperturbed by spurious currents of large magnitudes.

Table 4.4 The effect of time step on E_r , U_p , A_{loss} .

Δt [s]	E_r	U_p [m/s]	A_{loss}	CFL_p [-]
1×10^{-6}	0.2%	5.33×10^{-5}	<0.01%	2.67×10^{-5}
5×10^{-6}	0.2%	2.38×10^{-4}	<0.01%	5.95×10^{-4}
1×10^{-5}	0.2%	5.31×10^{-5}	<0.01%	2.66×10^{-4}
1×10^{-4}	0.4%	1.66×10^{-3}	1.2%	8.30×10^{-2}
5×10^{-4}	0.1%	1.33×10^{-3}	<0.01%	3.33×10^{-1}

4.2.4 Ohnesorge number

Since the exact solution for velocity in the flow domain is zero, the Ca value can be determined as a function of U_p and, thus, cannot easily be determined *a priori*. Another relevant dimensionless number which can be used is the Ohnesorge number (Oh)

$$Oh = \frac{\mu}{(2r\rho\sigma)^{1/2}} = \sqrt{\frac{Ca}{Re}} \quad (4.7)$$

Essentially, Oh^2 is the ratio of Ca to Re , an inverse of the Laplace number (La)

$$Oh^2 = \frac{Ca}{Re} = \frac{1}{La} = \frac{\mu^2}{2r\rho\sigma} \quad (4.8)$$

Re and Ca numbers can be determined as functions of the magnitude of the parasitic currents from

$$Ca_p = \frac{\mu U_p}{\sigma} \quad (4.9)$$

$$Re_p = \frac{2r\rho U_p}{\mu} \quad (4.10)$$

In this case due the small length scale and low Re the Weber number (We) is not relevant. The results in Table 4.5 show the influence of σ and Oh^2 on the determined parameters Oh^2 on E_r , U_p , A_{loss} . Notably, the Ca values change very little with the changing σ or Oh^2 values. When the interfacial tension becomes too dominant, as indicated by the small Oh^2 values, the difficulties to the numerical scheme become evident.

Table 4.5 The influence of the interfacial tension and Oh^2 on E_r , U_p , A_{loss} .

σ [N/m]	Oh^2	U_p [m/s]	Ca	E_r	A_{loss}
0.0001	25	6.20×10^{-5}	3.10×10^{-3}	0.15	<0.01%
0.001	2.5	6.58×10^{-5}	3.29×10^{-4}	0.13	<0.01%
0.005	0.5	2.36×10^{-4}	2.36×10^{-4}	0.02	<0.01%
0.01	0.25	4.67×10^{-4}	2.34×10^{-4}	0.19	<0.01%
0.05	0.05	1.20×10^{-3}	1.20×10^{-4}	1.27	-2.6%
0.1	0.025	2.34×10^{-3}	1.17×10^{-4}	1.94	-3.9%

The increasing error observed at $Oh^2 \leq 0.05$, although insignificant (below 4%) is as the result of emerging spurious currents when the interfacial tension begins to dominate over viscous forces. (Renardy & Renardy, 2002). At Oh^2 values of 0.05 and 0.025 the droplet area increases to larger area than the initially specified as indicated by the negative A_{loss} values. This observation is the reverse of the type of mass loss expected from the scheme. Ordinarily, the second phase experiences the reduction in area (mass loss) rather than an increase. The magnitude of parasitic currents is also high for these latter two conditions to $\mathcal{O}(10^{-3})$. The overall results, however, indicate that interfacial tension values across three orders of magnitude with were handled with reasonable accuracy and minimal spurious currents. With the exception of Oh^2 of 0.05 and 0.025, the area of the droplet enclosed by the computed interface remained consistent with the initially specified droplet.

4.3 Dispersion of a chemical species in a microchannel

Mixing of chemical species is an important aspect of the current work, and as such, it is necessary to consider a benchmark computation of mass transport (convection-diffusion). The first case under consideration is that of transport of chemical species by only molecular diffusion where there is no flow. The second case is the axial (Taylor) dispersion of chemical species due to both convective and diffusive effects. The dispersion is also known as Taylor-Aris dispersion.

4.3.1 Diffusion

Consider a tracer of chemical species transversely orientated between two parallel plates of length L , as illustrated in Figure 4.9. When the tracer extends the across the distance h between the plates and across the width, the diffusive transport is considered only in the axial direction, and is described by a one-dimensional differential equation (Fick's Second Law)

$$\frac{\partial C}{\partial t} = D \frac{\partial^2 C}{\partial x^2} \quad (4.11)$$

The dimensionless concentration profile of diffusing species is a normally distributed Gaussian curve, described by

$$\frac{C(x,t)}{C_0} = \frac{1}{\sqrt{4\pi Dt}} \exp\left(-\frac{x^2}{4Dt}\right) \quad (4.12)$$

In the above analytical expression, C_0 is the initial concentration of the tracer, D is a diffusion coefficient and x is the axial distance from the centre of the

curve. The width w_D of the tracer species broadens due to the diffusion proportionally to \sqrt{Dt} .

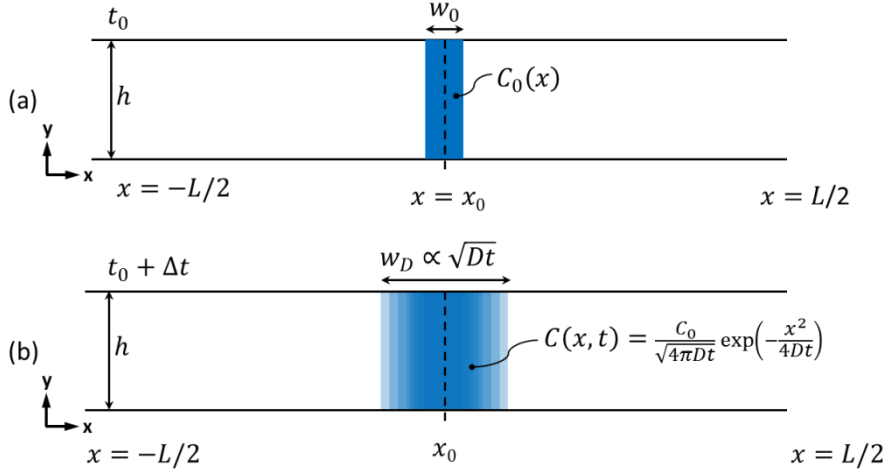


Figure 4.9 One-dimensional diffusion of a tracer species between parallel plates

The considered 2D domain consists of a microchannel of length $L = 1000\mu\text{m}$ and height $h = 100\mu\text{m}$. Although the case is that of a flow between parallel plates, for simplicity, the flow conduit herein is referred to as a microchannel. The middle of the axial dimension is positioned at $x = 0$. The governing equation, for diffusion only model is

$$\frac{\partial C}{\partial t} = D \left(\frac{\partial^2 C}{\partial x^2} + \frac{\partial^2 C}{\partial y^2} \right) \quad (4.13)$$

The initial tracer was set at

$$C(x, y, t) = C(-5 \times 10^{-6} \leq x \leq 5 \times 10^{-6}, 0 \leq y \leq h, 0) = C_0 = 1 \text{ mol/m}^3$$

and the concentration elsewhere in the domain set to zero. Zero-normal-flux conditions ($\frac{\partial C}{\partial \mathbf{n}} = 0$) were specified in all four boundaries of the domain.

The properties of the numerical meshes tested are shown in Table 4.6. The mesh was generated using an automatic meshing function for triangular elements. The mesh sizing function was set at 8×10^{-6} , 4×10^{-6} , 2×10^{-6} and 1×10^{-6} (metres) for the different tests.

Table 4.6 Properties of the different meshes used in the diffusion numerical model.

Sizing [m]	Max. [m]	Min. [m]	No. of nodes	No. of elements	Element area ratio	Min. quality	DOF
8×10^{-6}	9.15×10^{-6}	3.91×10^{-6}	2212	4140	0.1831	0.8714	8563
4×10^{-6}	4.76×10^{-6}	2.70×10^{-6}	8086	15618	0.3608	0.8536	31789
2×10^{-6}	2.41×10^{-6}	1.09×10^{-6}	32450	63796	0.1832	0.8557	128695
1×10^{-6}	1.14×10^{-6}	6.16×10^{-7}	125276	248350	0.3040	0.8502	498901

The absence of a convection term in Equation (4.13) makes finding a numerical solution to the problem relatively easy in a stable manner. Linear solver PARDISO was used to obtain the solution. Figure 4.11 shows the numerical results generated using meshes of different sizes which have been plotted together with the analytical results from Equation (4.14). In all cases, the solution obtained with the mesh size of $h = 4 \times 10^{-6}$ m was comparable to the analytical solution. Further reduction in the mesh size to $h = 2 \times 10^{-6}$ m yielded no change in the numerical solution. The results in Figure 4.12 were obtained with a fine mesh $h = 1 \times 10^{-6}$ m. Beyond 0.02s the colour visualisation is faded due to the low concentration relative to the highest value in the scale. Due to this challenge, subsequent surface and

contour plots in this chapter are presented with scales relative to respective maximum values in each time step.

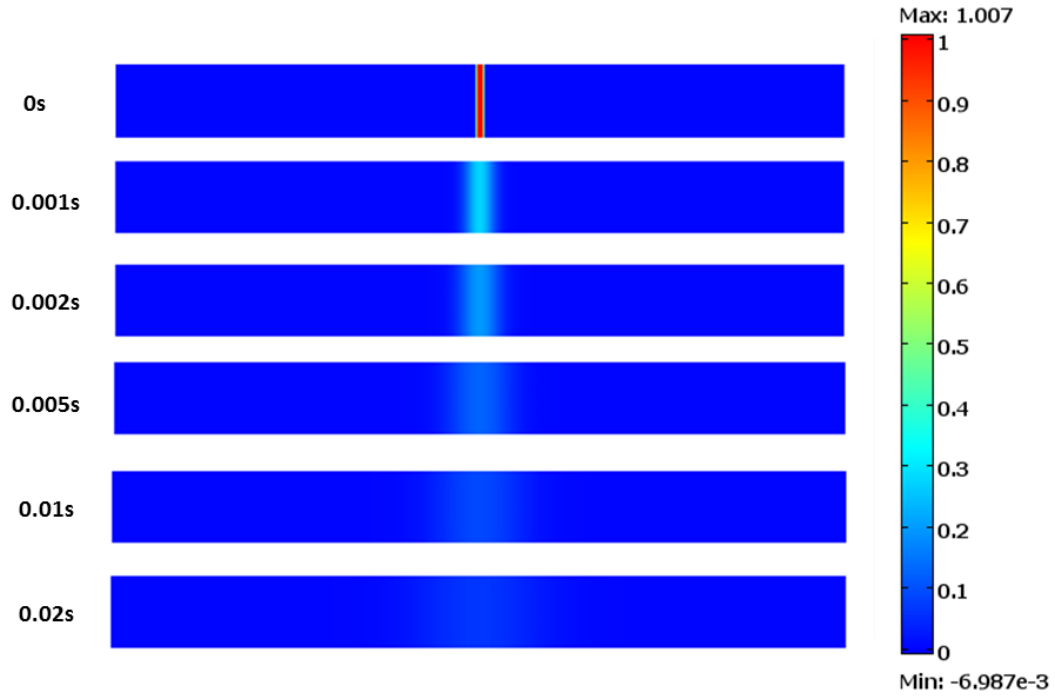


Figure 4.10: Colour plot of changes in concentration where the diffusion coefficient is $10^{-7} \text{ m}^2/\text{s}$.

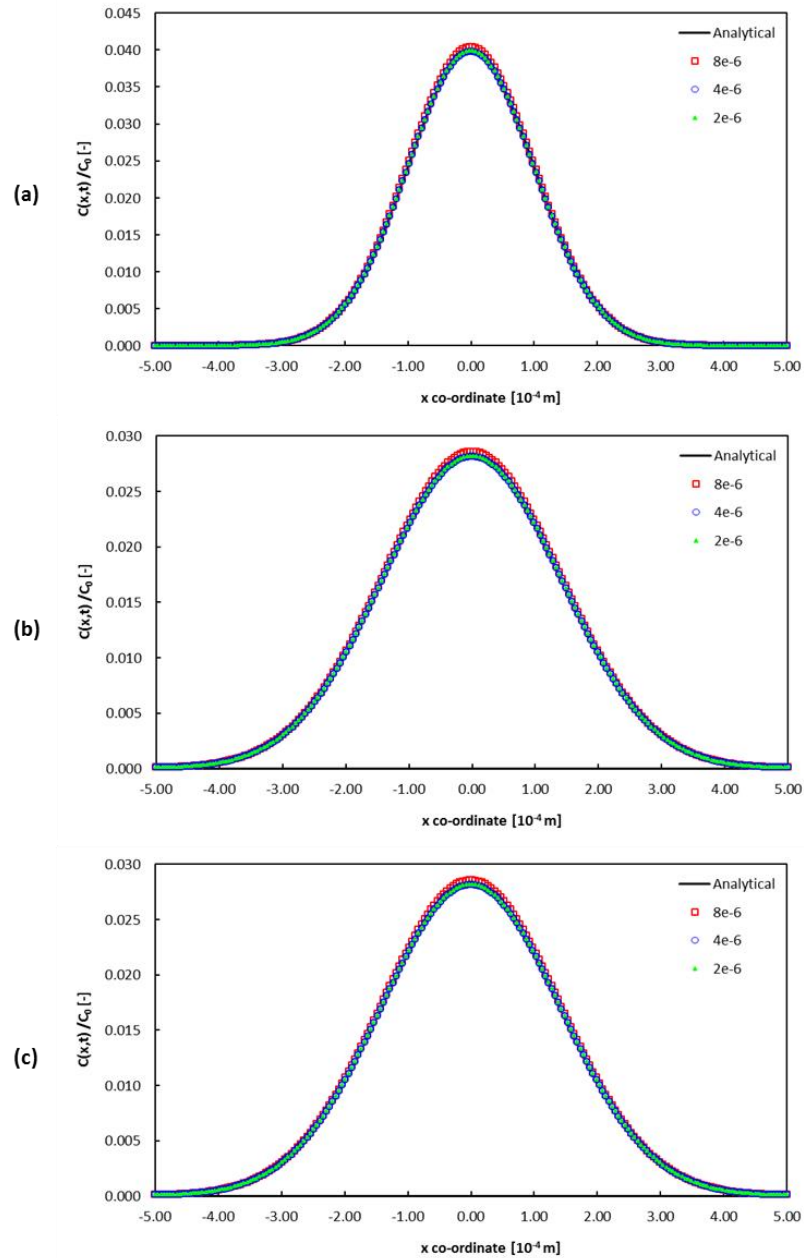


Figure 4.11 Analytical and numerical solutions of the dimensionless concentration profile across the x-axis of the channel for diffusion coefficients: (c) $10^{-11} \text{ m}^2/\text{s}$ (b) $10^{-9} \text{ m}^2/\text{s}$ and (c) $10^{-7} \text{ m}^2/\text{s}$ determined at times of 500s, 0.1s and 1s, respectively.

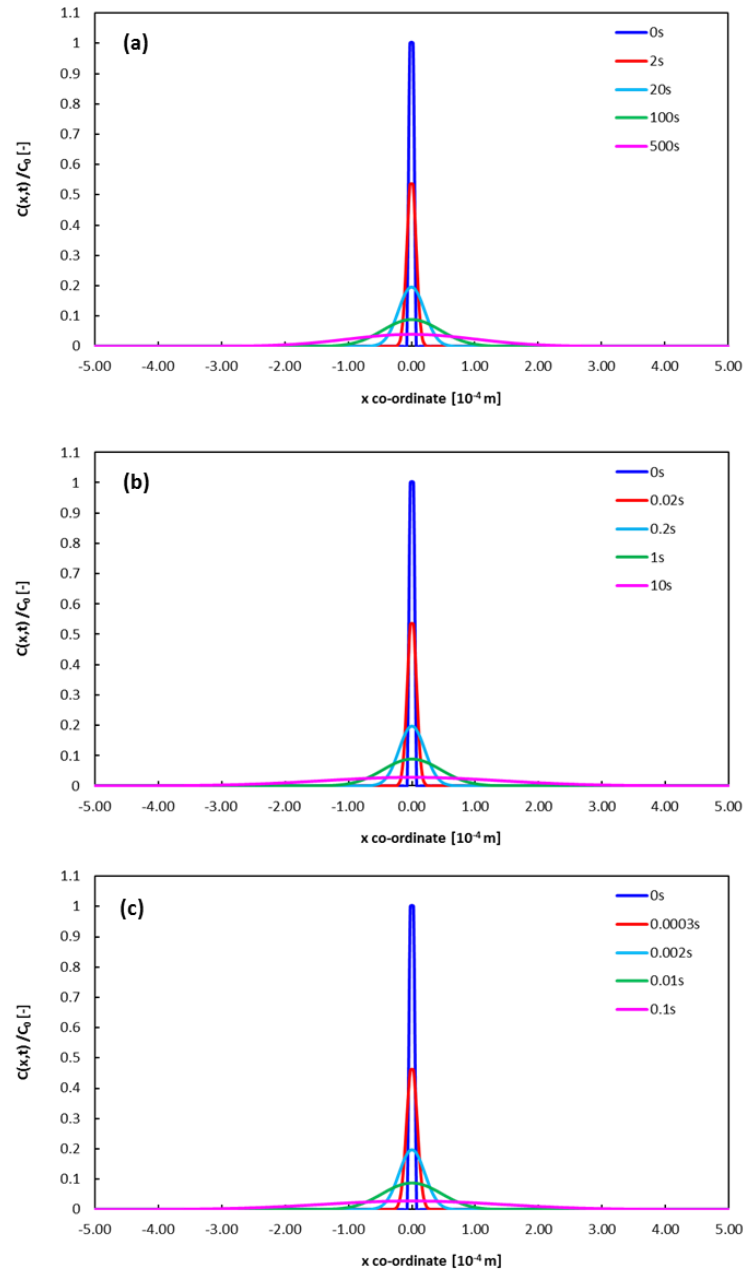


Figure 4.12 Dimensionless concentration profile across the x-axis of the channel at increasing times for diffusion coefficients: (a) $1 \times 10^{-11} \text{ m}^2/\text{s}$ (b) $1 \times 10^{-9} \text{ m}^2/\text{s}$ and (c) $1 \times 10^{-7} \text{ m}^2/\text{s}$.

There is a correlation between the diffusion timescales and the diffusion coefficients as shown the numerical results.

4.3.2 Taylor-Aris dispersion

The theory of the Taylor-Aris dispersion emanates from the classic work by Taylor (1953) and as extended by Aris (1955), which describes the dispersion of a solute in capillary laminar flow. In the presence of flow, the dispersion dynamics will differ from the case of pure diffusion in that the solute tracer experiences dispersive effect (Taylor dispersion) due the parabolic velocity profile of the flow. The condition of the flow is steady and fully developed (Hagen-Poiseuille flow). Figure 4.13 depicts the dispersion in a microchannel under the influence of the parabolic flow.

In the limit of $L \gg h$, or $Pe \ll L/h$ the mean concentration of the species across changes according to

$$\frac{\partial \bar{C}}{\partial t} + U \frac{\partial \bar{C}}{\partial x} = K \frac{\partial^2 \bar{C}}{\partial x^2} \quad (4.14)$$

where \bar{C} is the mean concentration, averaged across h , U is the average velocity and K is a Taylor dispersion coefficient or effective diffusion coefficient. For a case of flow between parallel plates, the effective diffusion coefficient is determined from

$$K = D \left(1 + \frac{Pe^2}{210} \right) \quad (4.15)$$

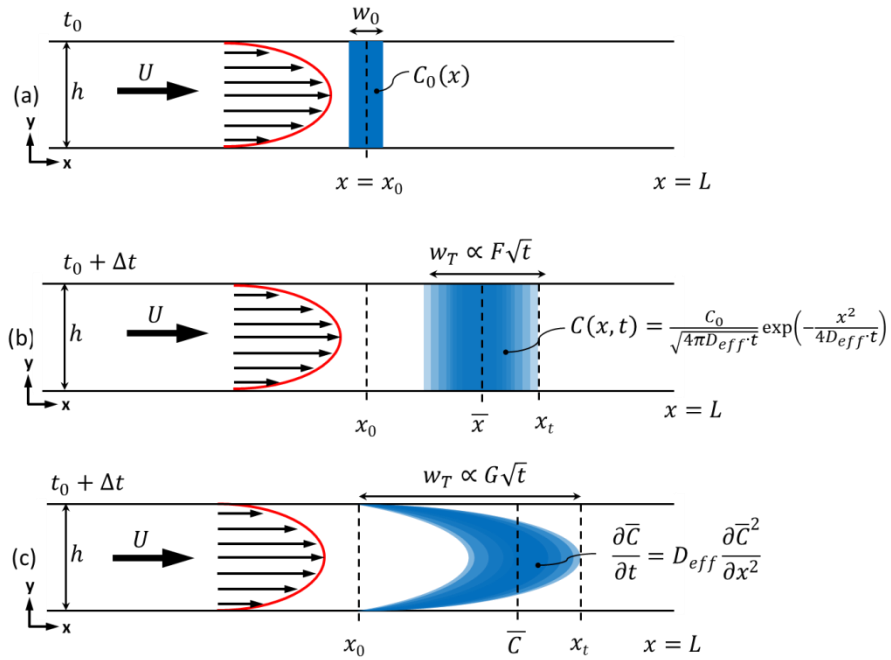


Figure 4.13 Taylor dispersion as a result of the parabolic flow. Adapted from Wilkes (2006).

The criterion for validity of the Taylor-Aris theory is that the residence time $t_r = L/U$ should be greater than the diffusive period of time $t_d = h^2/D$ (Taylor, 1953). The analytical solution for the Taylor dispersion is given by

$$C(x, t) = \frac{c_0}{\sqrt{4\pi Kt}} \exp\left(-\frac{x^2}{4Kt}\right) \tag{4.16}$$

The width of the tracer increases according $w_T = 4\sqrt{\ln 2} \sqrt{Kt}$ (Kirby, 2010).

The governing equations for the problem are Navier-Stokes and convection-diffusion equations

$$\nabla \mathbf{u} = 0 \quad (4.17)$$

$$\frac{\partial \mathbf{u}}{\partial t} + \mathbf{u} \cdot \nabla \mathbf{u} = -\nabla p + \nabla \cdot \mu [\nabla \mathbf{u} + (\nabla \mathbf{u})^T] \quad (4.18)$$

$$\frac{\partial C}{\partial t} + \mathbf{u} \cdot \nabla C - D \nabla^2 C = 0 \quad (4.19)$$

where $\mathbf{u} = (u_x, u_y)$ and $\nabla = \frac{\partial}{\partial x} + \frac{\partial}{\partial y}$.

The model considered in this case resembles the diffusion case in Section 4.4.2 above and the numerical mesh utilised is $h = 2 \times 10^{-6}$. The inlet and outlet boundary conditions for the NS equation were specified as the velocity 0.0333 m/s and zero pressure, respectively. A no-slip boundary condition was set at the top and bottom walls. The fluid properties are taken as similar to that of water ($\mu = 1 \text{ Pa} \cdot \text{s}$, $\rho = 1000 \text{ kg/m}^3$). The initial conditions for the transient flow solution were obtained from a prior obtained steady solution. The solution of the Navier Stokes equation was used in the solution of the convection-diffusion transport equation. A zero concentration was set at the channel inlet for the convection-diffusion equation and a convective flux condition was set at the outlet. Zero-normal-flux conditions were specified at the channel walls. The initial condition for the diffusion-convection was specified as previously stated in the diffusion only case (sub-section 4.4.3). The time step was set to 0.001s for all computations. Massless numerical particles, transported purely by convection according to $\mathbf{x}' = \mathbf{u}(t, \mathbf{x})$, are introduced into the solution as a benchmark indicator of convective transport. The particles, as observable in Figure 4.14 through to Figure 4.17 represented

by black dots, are initially positioned at the starting line $x = 0$ across the width of the channel at intervals of 5×10^{-5} m.

There two cases in which the axial dispersion can be considered to fit the Taylor-Aris dispersion theory (Taylor limit). The first case is when $t_r \gg t_d$ and the second one is at long times when diffusion is small *i.e.* $t_r < t_d$. In the current case, since the tracer is initially located in the middle of microchannel, the convection time (t_r) is considered as $L/2U$, and therefore equal to 0.015s. On the other hand, the diffusion times for the diffusion coefficients 10^{-7} m²/s, 10^{-9} m²/s, 10^{-10} m²/s, 5×10^{-12} m²/s and 10^{-12} m²/s are 0.1s, 10s, 100s, 2000s and 10000s, respectively. Therefore, the latter condition is applicable and long flow times are required. However, in practical applications, viable times for microfluidic mixing should be sub-millisecond (Bringer, Gerdt, Song, Tice, & Ismagilov, 2004). In order for the first scenario to apply at the specified diffusion coefficients, smaller velocities which are typically also ineffective in real world microfluidics could be specified.

Figure 4.14 through to Figure 4.17 show simulated axial dispersion at selected times up to 0.1s for diffusion coefficients of 10^{-7} m²/s, 10^{-9} m²/s, 10^{-10} m²/s and 5×10^{-12} m²/s. Due to perpetuation of numerical instabilities at low diffusion coefficients and long times, the solution for $D = 5 \times 10^{-12}$ m²/s (Figure 4.17) could not be obtained beyond 0.05s using PARDISO. The multigrid solver as an alternative was able to achieve the solution of up to 0.1s. Table 4.7 shows

the minimum and the maximum values at various solution times up to 0.05s obtained using the two solvers. Although there are slight variations in the results obtained, the results fair well. For the case of low diffusion coefficient $D = 10^{-12} \text{ m}^2/\text{s}$, the solution was obtained using the multigrid solver.

Table 4.7 Comparison of minimum and maximum concentration (mol/m^3) values at various solution times obtained using PARDISO and multigrid solvers.

Time [s]	PARDISO		Multigrid	
	Min	Max	Min	Max
0	$7.94 \cdot 10^{-9}$	1.007	-0.0161	1.015
0.001	-0.245	1.239	-0.228	1.203
0.005	-0.310	1.276	-0.339	1.314
0.01	-0.344	1.264	-0.322	1.289
0.05	-0.420	0.979	-0.051	1.354

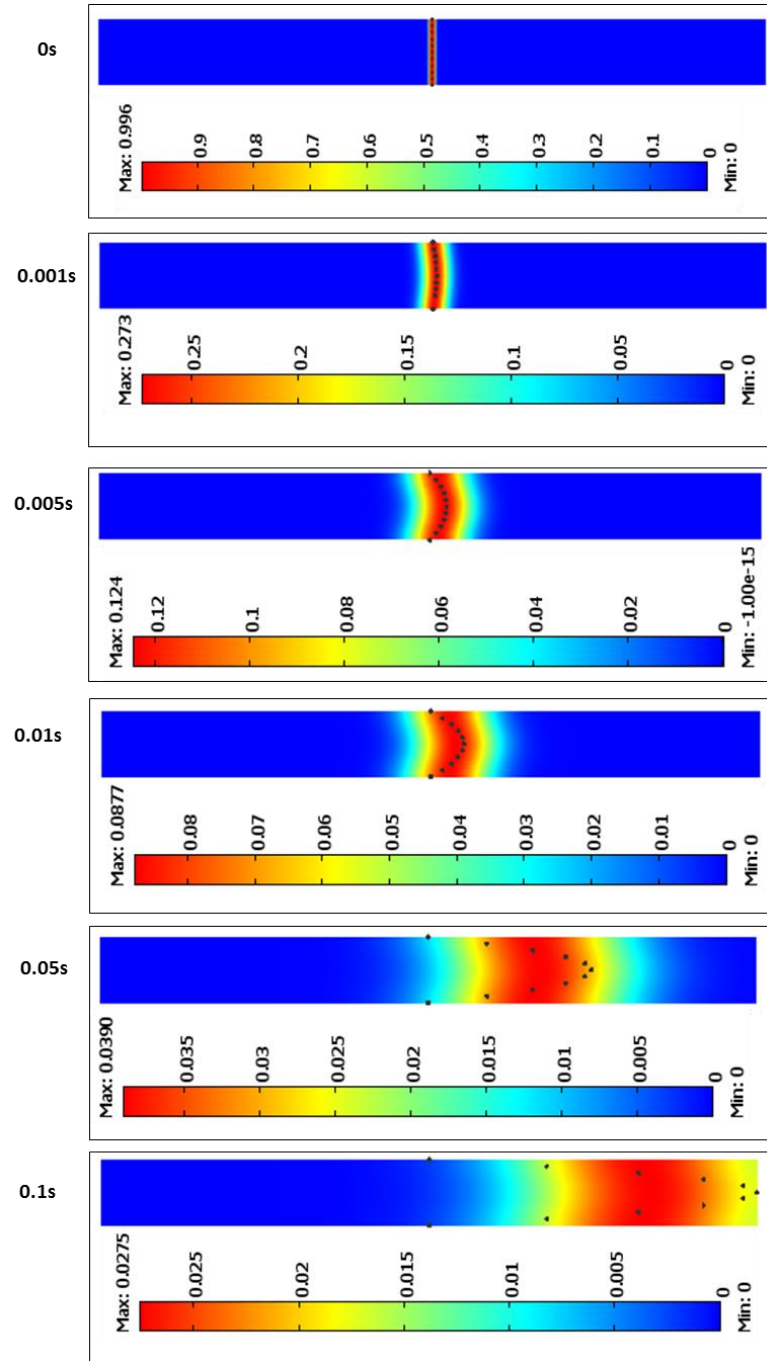


Figure 4.14 Dispersion of a solute tracer at high diffusion coefficient of $10^{-7} \text{ m}^2/\text{s}$. Concentration units are in mol/m^3 .

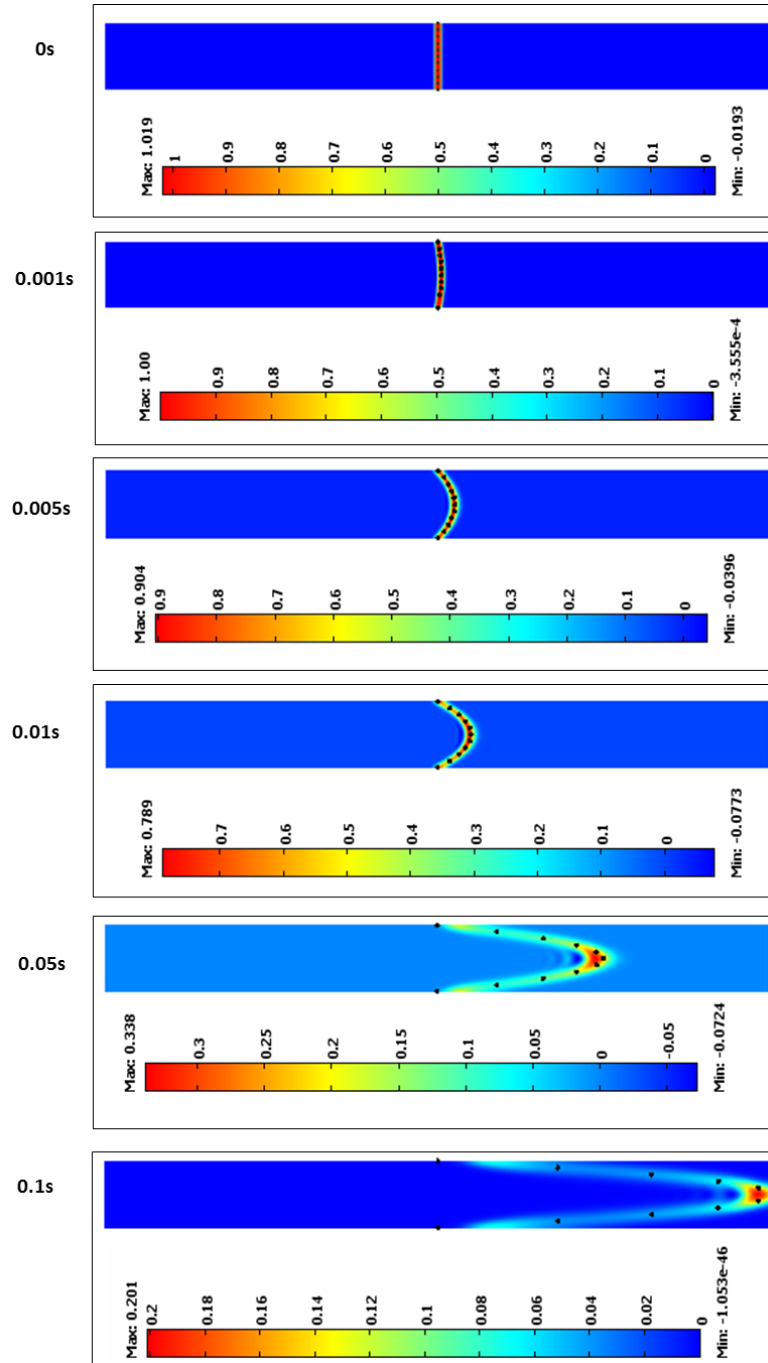


Figure 4.15 Dispersion of a solute tracer with a diffusion coefficient of $10^{-9} \text{ m}^2/\text{s}$. Concentration units are in mol/m^3 .

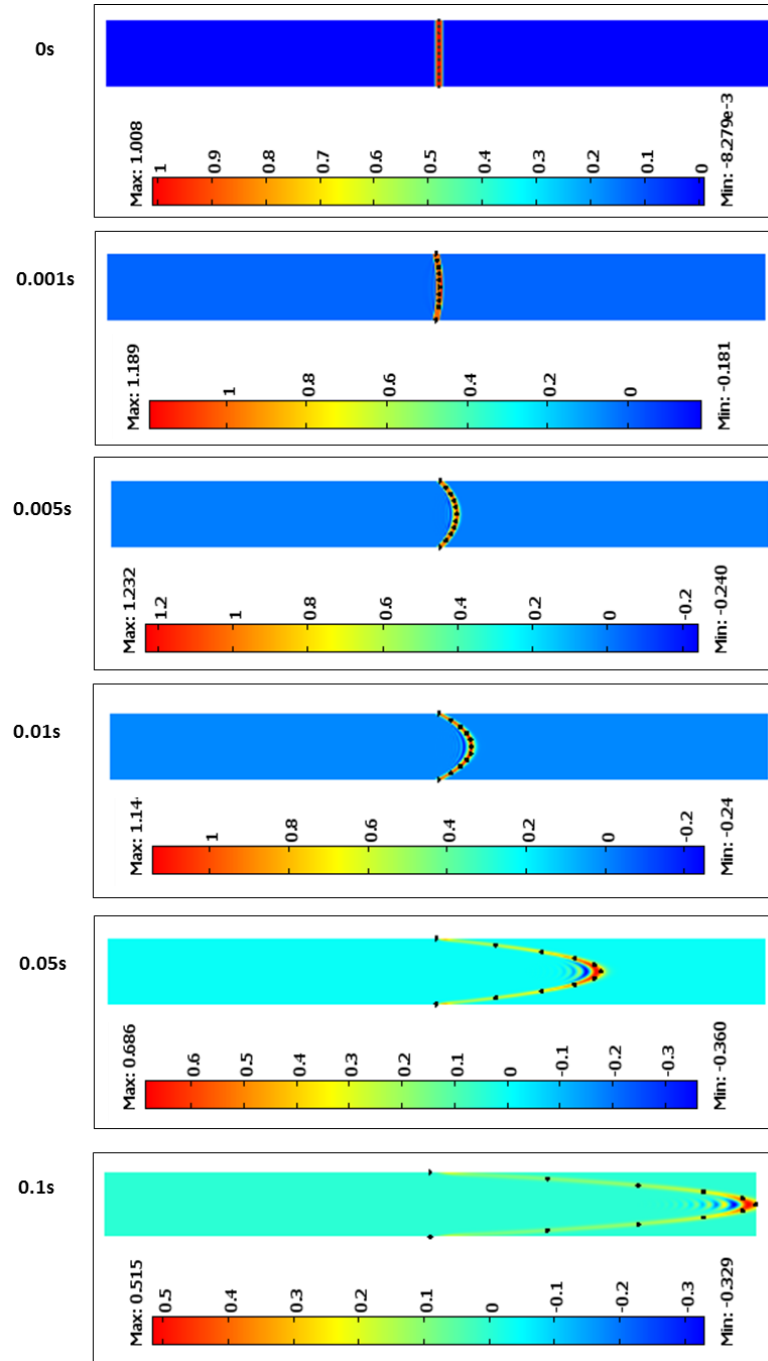


Figure 4.16 Dispersion of a solute tracer with a diffusion coefficient of $10^{-10} \text{ m}^2/\text{s}$. Concentration units are in mol/m^3 .

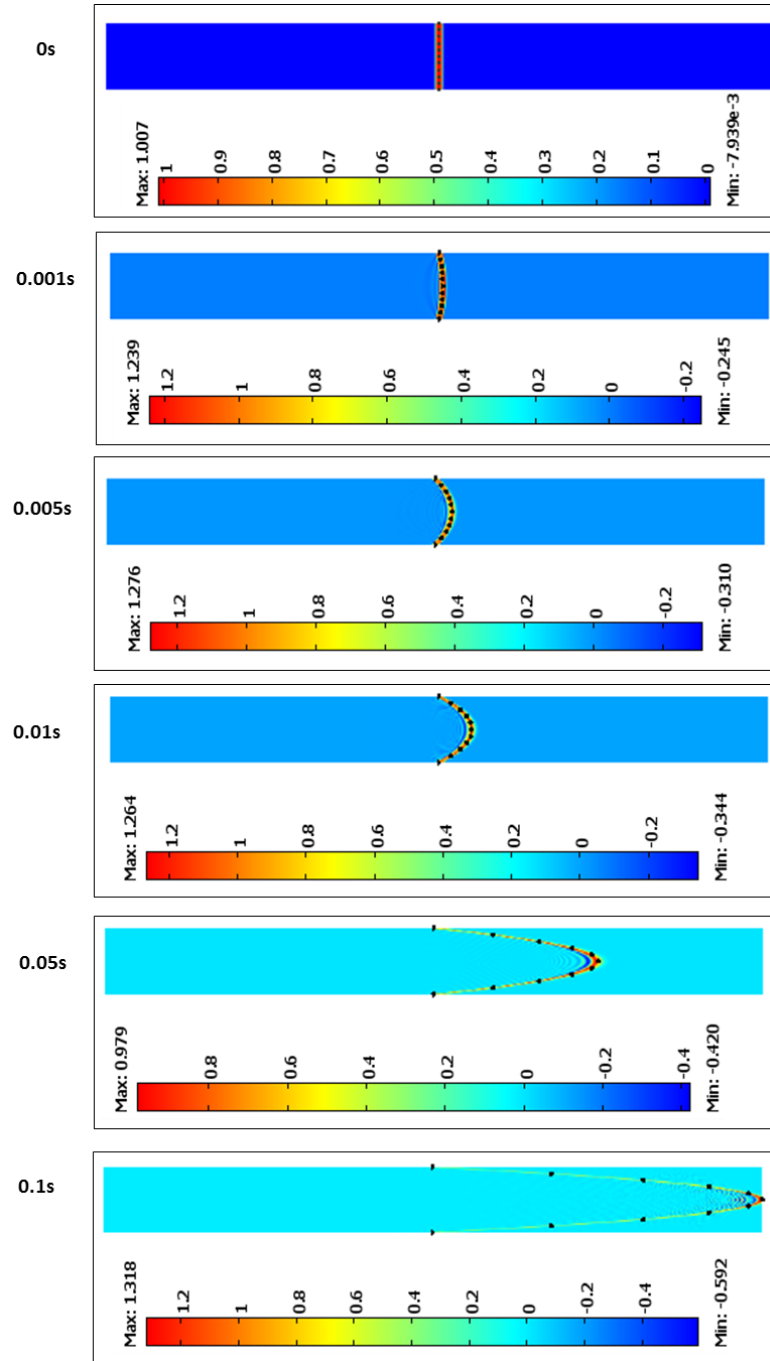


Figure 4.17 Dispersion of a solute tracer with at low diffusion coefficient of $5 \times 10^{-12} \text{ m}^2/\text{s}$. Concentration units are in mol/m^3 .

The implication of low diffusion coefficients is that Pe values dealt with in typical microfluidic channels of width equal to $100\ \mu\text{m}$ are at least $\mathcal{O}(500)$. When dealing with a numerical solution of a convection-diffusion equation, there is a general requirement to satisfy the cell Peclet number $Pe_{\hat{h}}$ inequality (Kuzmin, 2010)

$$Pe_{\hat{h}} = \frac{\|\mathbf{u}\|_{\infty} \hat{h}_{max}}{2D} \leq 2 \quad (4.20)$$

The onset of numerical instabilities at $D = 10^{-9}\ \text{m}^2/\text{s}$ (Figure 4.15) is consistent with this limitation, considering that $Pe_{\hat{h}}$ is already at 6.71 (where $\|\mathbf{u}\|_{\infty} = 0.00512\ \text{m/s}$ and $\hat{h}_{max} = 2.41 \times 10^{-6}\ \text{m}$). The implication of the above condition is that for a problem of given flow and chemical species (or diffusion coefficient) conditions, numerical instabilities can, theoretically, be avoided through reduction in mesh size. However, the limitation in that approach, as demonstrated in Figure 4.18 and Table 4.8, is that the number of mesh elements ($N_{\hat{h}}$) required to meet the condition increases exponentially with decreasing diffusion coefficient (*i.e.* $N_{\hat{h}} \propto 2.11Pe^2$). To that end, the number of mesh elements necessary to maintain $Pe_{\hat{h}} \leq 2$, for current case at the modest $D = 10^{-9}\ \text{m}^2/\text{s}$, would be $\approx 2 \times 10^6$, which is on the high demand side of available computer resources.

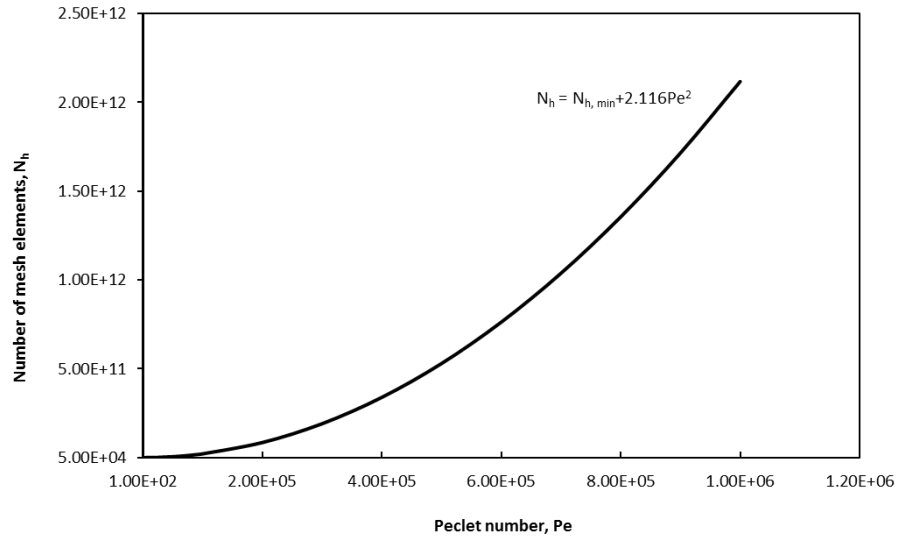


Figure 4.18 Exponential increase in required number of mesh elements to maintain $Pe_{\hbar} = 2$.

Table 4.8 Number of mesh elements required to maintain $Pe_{\hbar} = 2$.

Pe	D	Pe_{\hbar}	$\hbar_{Pe=2}$	N_{\hbar}
500	$2 \cdot 10^{-9}$	4.60	$4.35 \cdot 10^{-7}$	$5.29 \cdot 10^5$
1000	$1 \cdot 10^{-9}$	9.2	$2.17 \cdot 10^{-7}$	$2.12 \cdot 10^6$
2500	$4 \cdot 10^{-10}$	23	$8.70 \cdot 10^{-8}$	$1.32 \cdot 10^7$
5000	$2 \cdot 10^{-10}$	46	$4.35 \cdot 10^{-8}$	$5.29 \cdot 10^7$
7500	$1 \cdot 10^{-10}$	69	$2.90 \cdot 10^{-8}$	$1.19 \cdot 10^8$
10000	$1 \cdot 10^{-10}$	92	$2.17 \cdot 10^{-8}$	$2.12 \cdot 10^8$
15000	$7 \cdot 10^{-11}$	138	$1.45 \cdot 10^{-8}$	$4.76 \cdot 10^8$
20000	$5 \cdot 10^{-11}$	184	$1.09 \cdot 10^{-8}$	$8.46 \cdot 10^8$
50000	$2 \cdot 10^{-11}$	460	$4.35 \cdot 10^{-9}$	$5.29 \cdot 10^9$
100000	$1 \cdot 10^{-11}$	920	$2.17 \cdot 10^{-9}$	$2.12 \cdot 10^{10}$
500000	$2 \cdot 10^{-12}$	4600	$4.35 \cdot 10^{-10}$	$5.29 \cdot 10^{11}$
1000000	$1 \cdot 10^{-12}$	9200	$2.17 \cdot 10^{-10}$	$2.12 \cdot 10^{12}$

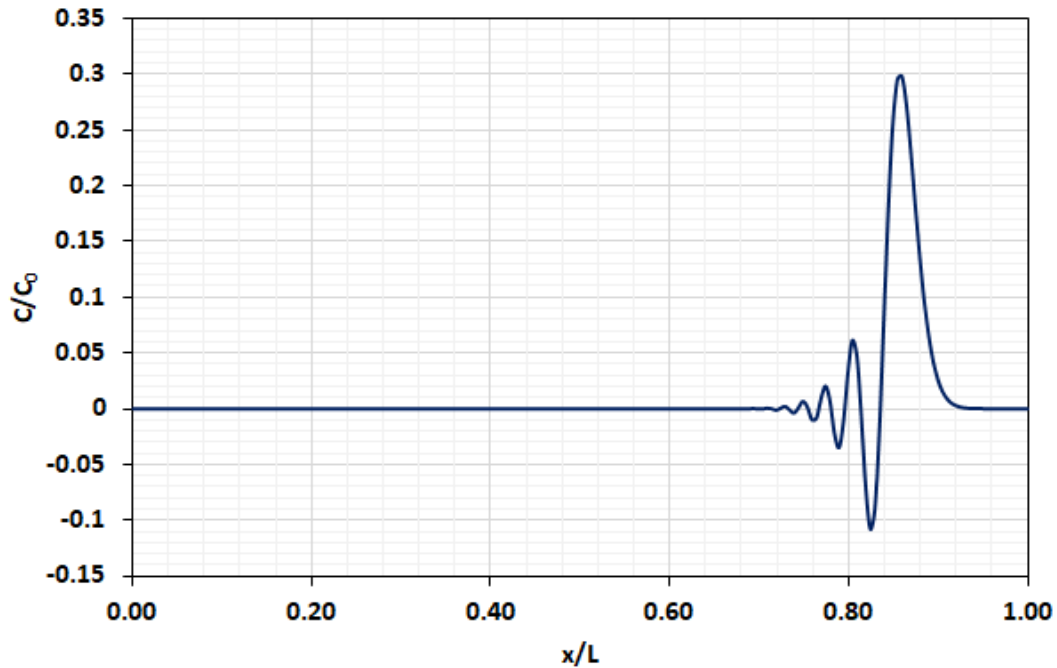


Figure 4.19 Instabilities in the normalised concentration profile from the Taylor-Aris dispersion solution at $Pe = 500$.

The instabilities of convection-diffusion equation were observed at $Pe = 500$ ($D = 2 \times 10^{-9} \text{ m}^2/\text{s}$), which required implementation of the artificial diffusion. The refined mesh of $h_{max} = 1 \times 10^{-6} \text{ m}$, was already high and sufficient

Guidelines recommended by COMSOL did not provide acceptable results (Comsol AB, COMSOL Multiphysics 3.5a Modelling Guide, 2008b). For example, the instabilities or spurious oscillations in the solution using streamline Petrov-Galerkin compensated diffusion tuned to 0.5, such as

shown in Figure 4.20, exceeded the case without artificial diffusion. The anisotropic artificial diffusion, on the other hand reduced the instabilities better than the Petrov-Galerkin methods but resulted in higher error of the solution. Hence, an iterative tuning approach was followed in evaluating an acceptable method and tuning parameters (See Appendix B).

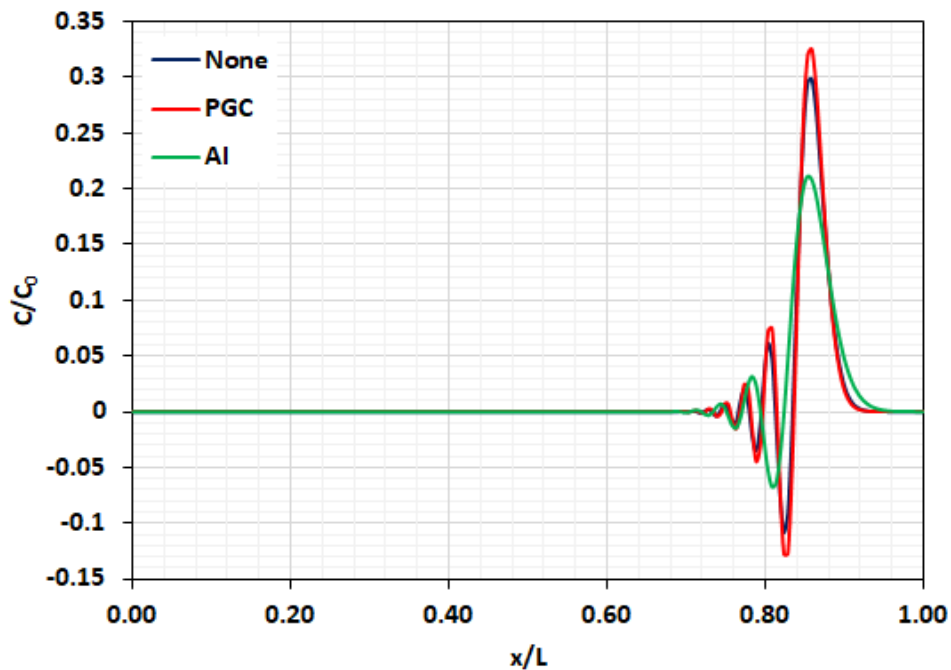


Figure 4.20 Instabilities in the concentration profile from the solution of the Taylor-Aris dispersion at $Pe = 500$ with streamline Petrov-Galerkin compensated (PGC) tuned to 0.5 and anisotropic (AI) diffusion set at 0.25.

The combination of diffusion methods using isotropic, SUPG and cross wind shock capturing provided the best results (Figure 4.21). Unfortunately, these

spurious oscillations cannot be completely eliminated and are generally not negligible (Knobloch & Tobiska, 2011).

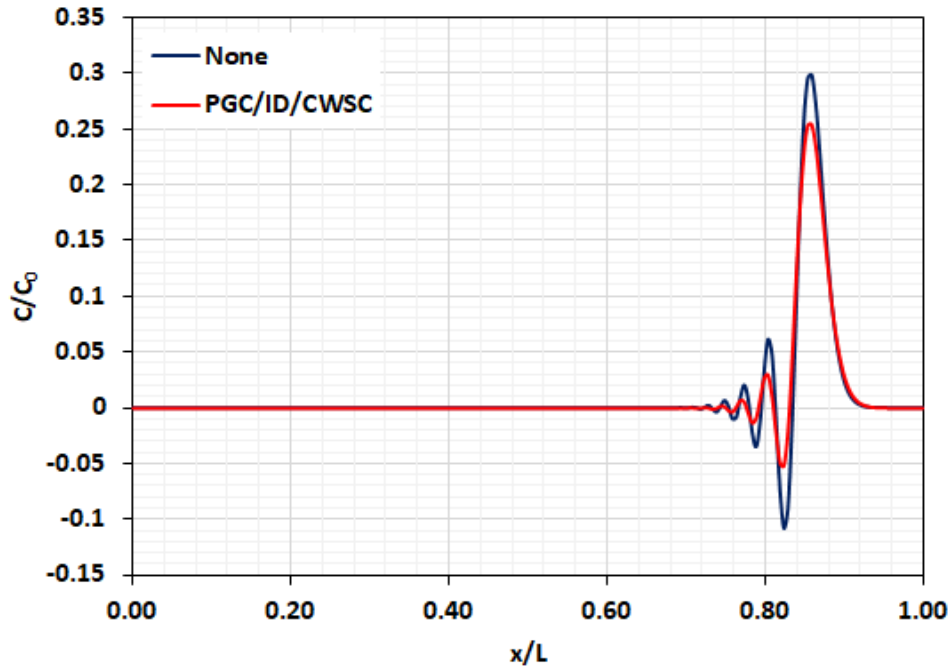


Figure 4.21 Instabilities in the normalised concentration profile from the solution of the Taylor-Aris dispersion at $Pe = 500$ with combined isotropic (ID), streamline Petrov-Galerkin compensated (PGC) and crosswind shock capturing (CWSC) tuned to 0.05, 0.5 and 0.35, respectively.

4.4 Conclusion

In the CFD field, there is a general understanding that there is no panoptic proof of the correctness of complex computational models. (Oberkampf &

Trucano, 2002). In that context, this chapter evaluated and demonstrated the suitability of COMSOL Multiphysics™ for handling problems involving droplets, moving interfaces and transport of chemical species (convection-diffusion). The benchmark cases used in the evaluation were adequately solved within specific numerical parameters. These parameters provide guidelines and limitations for utilising COMSOL as a numerical tool in two-phase microfluidics involving mixing. The benchmark computations fair with analytic models against which accuracy can be confidently determined. There is a need for exceedingly fine meshes in order to correctly capture deformations in the interface when utilising the level set method. Solutions of convection-diffusion that are without oscillations remain without a definitive and optimal artificial diffusion method. It remains an open question as to which method performs best (John & Knobloch, 2008).

"Man's life is like a drop of dew on a leaf." -- Socrates

Chapter 5

Modelling of Droplet Mixing Using Two-Phase Moving-Frame-of-Reference

5.1 Introduction

The aim of the current chapter is two-fold. Firstly, the work seeks to assess the two-phase moving-frame-of-reference modelling approach as means of studying mixing in droplets or plugs travelling in straight microchannels. Secondly, the parameters that influence the mixing within a droplet transported in a straight microchannel are evaluated.

Previous numerical studies looking at mixing within a moving microfluidic droplet have either utilised the single-phase moving-frame-of-reference or two-phase fixed-frame-of-reference. The studies by Tung *et al.* (2009) and Jiang *et al.* (2012) are examples where two-phase fixed-frame-of-reference was utilised. There is scope for demonstration of the two-phase moving-frame-of-reference approach for studying mixing microfluidic droplets.

5.2 Development of numerical model

5.2.1 Assumptions

In developing the model, five key assumptions were imposed. Whilst the assumptions simplify the model, they were plausible and practical for the problem at hand. The assumptions were as follows:

- (1) The flow is Newtonian and isothermal.
- (2) There is only one droplet in the system. The resulting flow field is as a result of a carrier fluid transporting an individual droplet in the microfluidic channel.
- (3) The Marangoni effects are negligible and, therefore, gradients of interfacial tension do not exist.
- (4) Viscosity and density are constant in each phase and not a function of concentration of the chemical/solute species.
- (5) Mass transport is confined within the droplet phase and interfacial mass transfer does not occur. This case is typical where solutes have low diffusivity in the carrier phase.

5.2.2 Model geometry

The model geometry for the problem is set up in two-dimensions (2D), as illustrated in Figure 5.1. The droplet (plug) is positioned along the centre line of a microchannel of length L and height, h . The droplet is specified as a

composite geometric structure comprising a rectangle capped by two semi-circles of equal diameter at the front and back ends. Initially, the plug is of certain prescribed length, L_0 and width, w_0 . As such, the nose and the tail are of equal curvatures ($d_n = d_t$). The distance between the plug tail and the back end of the microchannel is X_t and X_n is the distance between the nose and the front end of the microchannel.

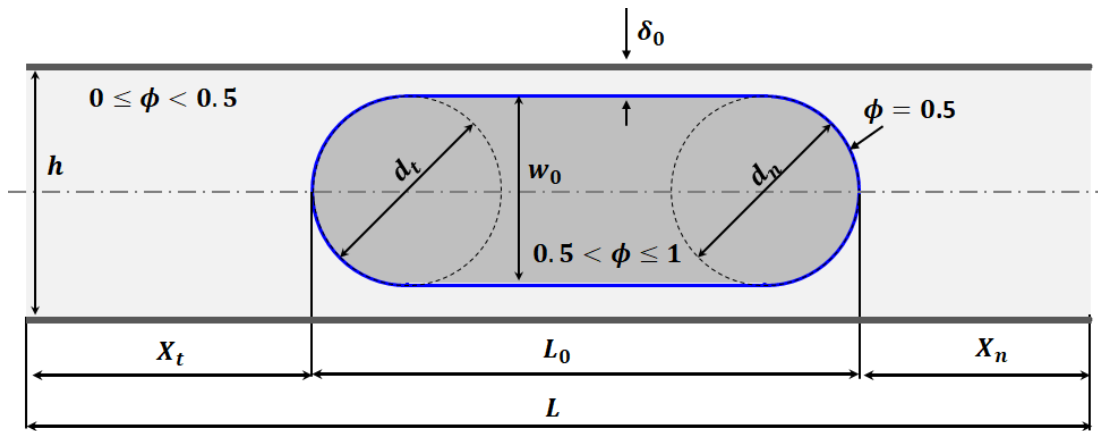


Figure 5.1 Schematic representation of the 2D model geometry for the current problem.

The channel height was fixed at $h = 100 \mu\text{m}$ and L_0 varied between $1.5h$ and $5h$. The prescribed droplet width (w_0), as well as d_n and d_t were also constant at $0.8h$. The thickness of lubrication film is specified as $\delta_0 = 0.5(h - w_0)$. The microchannel length L is based on L_0 , X_n and X_t , where $X_t = h$, and $X_n = h$.

5.2.3 Mesh

A triangular mesh with the maximum size of 10^{-6} m was specified in the domain. The mesh at the walls was specified to have a maximum size of 2×10^{-7} m. In Chapter 4, the specified mesh size had been demonstrated to give mesh-independent solutions for both the solutions of the two-phase flow (level set method) as well as mass transport (convection-diffusion).

5.2.4 Computation of the flow field

The flow field and the concentration field were computed sequentially, with the flow solution being computed first. The governing equations are the Navier-Stokes and the level set equations. Figure 5.2 shows the imposed initial and boundary conditions for the flow solution.

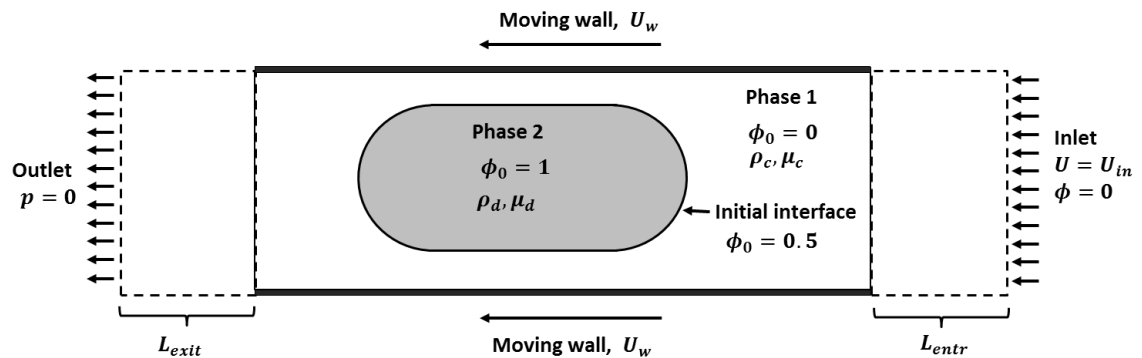


Figure 5.2 Initial and boundary conditions for a droplet travelling in microchannel modelled using a two-phase moving-frame-of-reference.

The superficial velocity of the system is defined by the difference between the droplet velocity and the average inlet velocity, *i.e.* $U_s = U_d - U_{in}$. The speed of the dispersed phase relative to the superficial velocity is given by the droplet mobility, $\mathcal{M} = U_d/U_s$. When $\mathcal{M} = 1$, the droplet and the carrier travel with the same speed, typically when there is no lubrication film and the plug is fully wetting to the walls of microchannel (Walker, 2016). The current problem considers the case where $\mathcal{M} > 1$ and a lubrication film exists between the droplet and the channel wall. Necessarily, for the current problem $\mathcal{M} > 1$ condition must always prevail, due to the moving wall boundary conditions. The effect of gravity and Marangoni effects were neglected. The density of 1000 kg/m^3 and the interfacial tension of 0.14 N/m were utilised in all cases, except where specified otherwise.

The computations for both the two-phase flow and convection-diffusion equations were achieved using the parallel direct solver (PARDISO). The time steps for all cases were set to conform to *CFL* condition of 0.25.

5.2.5 Quasi-steady-state condition

The values of U_s , U_d and U_{in} were determined iteratively from Ca and an initial estimate of droplet mobility and the solution was computed until a quasi-steady-state condition was achieved. The true steady-state or equilibrium for the simulation prevails when displacement of the nose of the droplet in the axial direction is zero (Taha & Cui, 2006b). The condition set for

the quasi-steady-state is $|U_{drift}|/U_{sv} \leq 10^{-2}$ in a minimum of 100 timesteps, where U_{drift} is the speed at which the nose moves at a given U_w and U_{in} . The prevailing Ca values were then determined from the quasi-steady-state U_s . The flow diagram in Figure 5.4 shows the iterative process towards achieving the desired quasi-steady-state condition. Figure 5.3 illustrates the position of fluid-fluid interface at quasi-steady-state versus its position at initial condition.

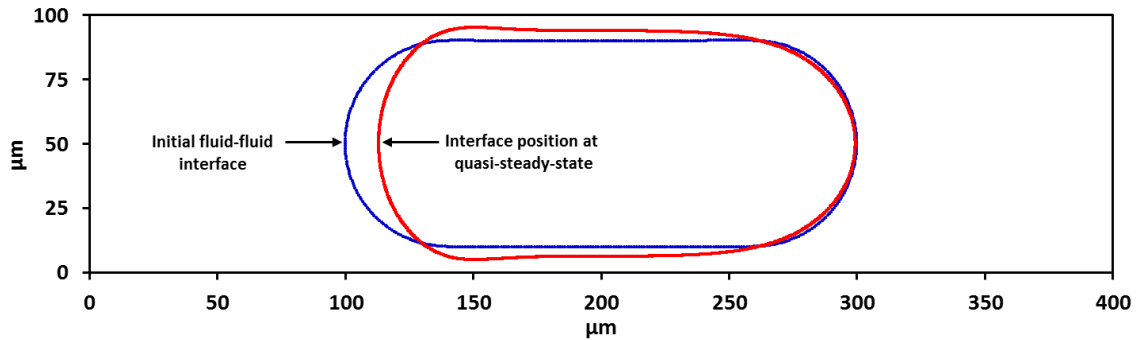


Figure 5.3 Illustration of the interface at the initial position (blue line) and when is at quasi-steady-state (red line).

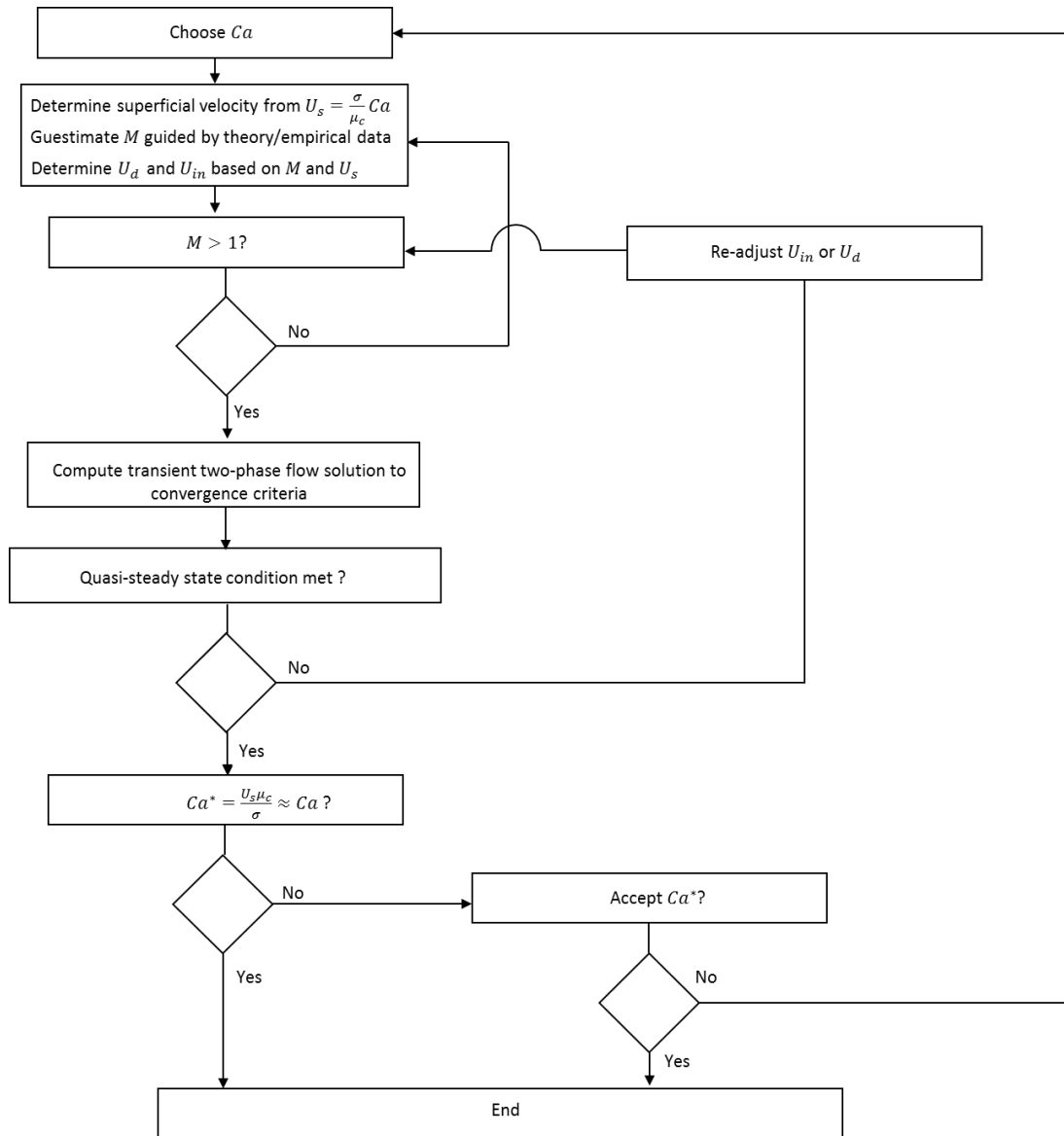


Figure 5.4 Flow diagram for the iteration process towards quasi-steady-state of the flow solution.

5.2.6 Computation of the concentration field

The concentration field was computed as a function of time by solving the convection- diffusion equation, coupled to the velocity field to flow solution. The velocity field for the computation of the concentration field was obtained from the quasi-steady-state solution of the two-phase flow. The computation of the concentration field $C(x, y, t)$ was confined to only the droplet phase ($\phi > 0.5$) by imposing subdomain and initial conditions which are appropriate for the model. The convection of the solute species into the carrier phase was minimised by making the x and y velocity components 3 orders of magnitude smaller than in the droplet phase, *i.e.*

$$u_x = u_x|_{\phi > 0.5} + (u_x|_{\phi \leq 0.5}) \cdot 10^{-3} \quad \text{and} \quad u_y = u_y|_{\phi > 0.5} + (u_y|_{\phi \leq 0.5}) \cdot 10^{-3} \quad ,$$

where u_x and u_y are x and y components of the velocity field. The second terms in the expressions minimise numerical errors which emanate from large concentration and velocity discontinuities the interface. Instead of the velocity components being set zero in the continuous phase, they are limited to three orders of magnitude smaller than the components in the droplet phase. The diffusion of solute species across the interface is constrained by imposing variable diffusion coefficient between the two phases as per $D|_{\phi > 0.5} = D_0$ and $D|_{\phi \leq 0.5} = D_0 \cdot 10^{-2}$. For the current study $D_0 = 10^{-9} \text{ m}^2/\text{s}$ and constant. As with the case on velocity components, the second term accounts for the diffusion coefficient in the carrier phase which is very small but not equal to zero.

The initial distribution of concentration of the solute species is either transversely or axially to the flow direction as illustrated in Figure 5.5.

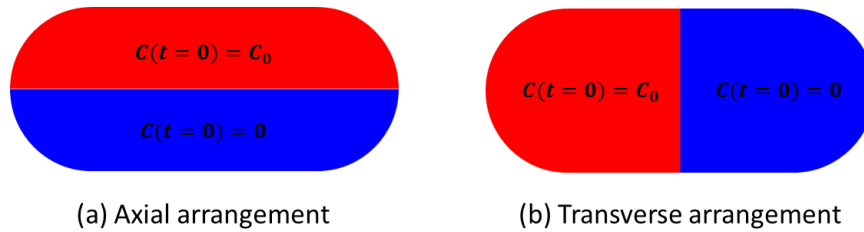


Figure 5.5 Illustration of the two alternative initial arrangements of the solute species: (a) Axial orientation and (b) Transverse orientation.

Of the two, the transverse orientation is the most favourable initial distribution for an efficient mixing inside droplets and plugs (Sarrazin, *et al.*, 2006; Tanthapanichakoon, *et al.*, 2006a). In order to achieve transverse orientation, some microfluidic operations involve merging two droplets consisting of the fluid elements to be mixed in a merged droplet.

5.2.7 Dimensionless parameters

The capillary number and the Reynolds numbers are quantified in terms of the superficial velocity and the properties of continuous phase as $Ca = \mu_c U_s / \sigma$ and $Re = \rho_c U_s h / \mu_c$. The material properties of the continuous and the dispersed phases are compared through the viscosity ratio ($\lambda = \mu_d / \mu_c$) and density ratio ($\psi = \rho_d / \rho_c$). The thickness of the film (δ_f) is scaled by h such that $\delta^* = 2\delta_f / h$ is the non-dimensionalised film thickness.

The ratio of the diffusive timescale w_d^2/D to the convective timescale (L_d/U_{sv}), expressed as a modified Peclet number ($Pe_m = w_d^2 U_{sv}/DL_d$), was suggested by Tanthapanichakoon, *et al.*, (2006a) to be an important dimensionless parameter for designing mixing in microfluidic plugs. The modified Peclet number is however limited, as it does not take into account the effect of the viscosity ratio between the carrier and the droplet phases. Appendix C provides a table of computed modified Peclet numbers as a function of the capillary number for droplets/plugs of different sizes.

5.3 Parametric study

The influence of mixing by a number of parameters was investigated through a parametric study (See Sections 5.4 and 5.5). The effect of the density ratio was excluded from the study and therefore kept constant at unity for all cases unless specified otherwise. Results from previous numerical studies suggest that two-phase flows in microchannels at low Re and λ are independent of density ratio (Walker, 2016). The Reynolds number, being a dependent variable, was influenced and varied with the controlling parameters. These selected parameters were typical of operating conditions in microfluidic systems.

5.3.1 Capillary number

The capillary numbers varied between 0.002 and 0.21, in proportion to the superficial velocity which was adjusted by changing the wall velocity. Under conditions of constant interfacial tension, the capillary number changes with changes in viscosity and in superficial velocity. The lower limit of the capillary number is constrained by the droplet mobility condition $\mathcal{M} > 1$, where the two-phase MFR model becomes untenable.

5.3.2 Droplet size

Droplets (or plugs) of different sizes were modelled by postulating the initial size of the droplet (L_d) to h , $2h$ and $5h$. The viscosity ratio of 0.5 was used for the droplet size study (Sub-section 5.5.5).

5.3.3 Viscosity ratio

The effect of viscosity ratio was investigated at single initial droplet size of $L_0 = 2h$. The input parameters for the study are given in Table 5.1, together with the range of quasi-steady-state capillary and Reynolds numbers. The viscosity range is comprehensive typical of microfluidic applications. The viscosity of the continuous phase remained constant for all the simulations.

Table 5.1 Parameters for the investigations of influence of viscosity ratio

λ	μ_d [Pa·s]	μ_c [Pa·s]	σ [N/m]	L_0	Ca range	Re range
0.1	$2 \cdot 10^{-4}$	$2 \cdot 10^{-3}$	0.14	$2h$	0.002 to 0.21	5 to 75
0.5	$1 \cdot 10^{-3}$	$2 \cdot 10^{-3}$	0.14	$2h$	0.002 to 0.21	5 to 75
1	$2 \cdot 10^{-3}$	$2 \cdot 10^{-3}$	0.14	$2h$	0.002 to 0.21	5 to 75
2	$4 \cdot 10^{-3}$	$2 \cdot 10^{-3}$	0.14	$2h$	0.002 to 0.21	5 to 75
10	$2 \cdot 10^{-2}$	$2 \cdot 10^{-3}$	0.14	$2h$	0.002 to 0.21	5 to 75

5.4 Numerical results for flow field and hydrodynamics

5.4.1 Droplet mobility

Figure 5.6 shows the dependency relationship between droplet mobility and capillary number at viscosity ratios of 0.1, 0.5, 1, 2 and 10. The droplet mobility was computed from the iteratively-determined flow parameters at quasi-steady-state. For all the viscosity ratios the droplet mobility increases monotonically with increasing capillary number. It is expected that for larger capillary numbers, the mobility would tend towards an asymptotic value upon which the data would diverge from the current curve fit. The significance of these results is that the parameters flow U_d , U_s , and \mathcal{M} can be stated *a priori* for other simulation studies within the Ca range.

The numerical data for the viscosity ratios in the range $0.017 < Ca < 0.25$ converge to the fitted curve $\mathcal{M} = 0.0675 \ln Ca + 1.339$. The range of the mobility ratios are within the recirculating flow regimes described in

literature (Boudreaux, 2015). The droplet of lowest viscosity ($\lambda = 0.1$) demonstrates a higher mobility compared to higher viscosity ratios at the same capillary number. In the considered range, $0.02 < Ca < 0.13$, the mobility values are between 1% and 3% higher compared to other viscosity ratios.

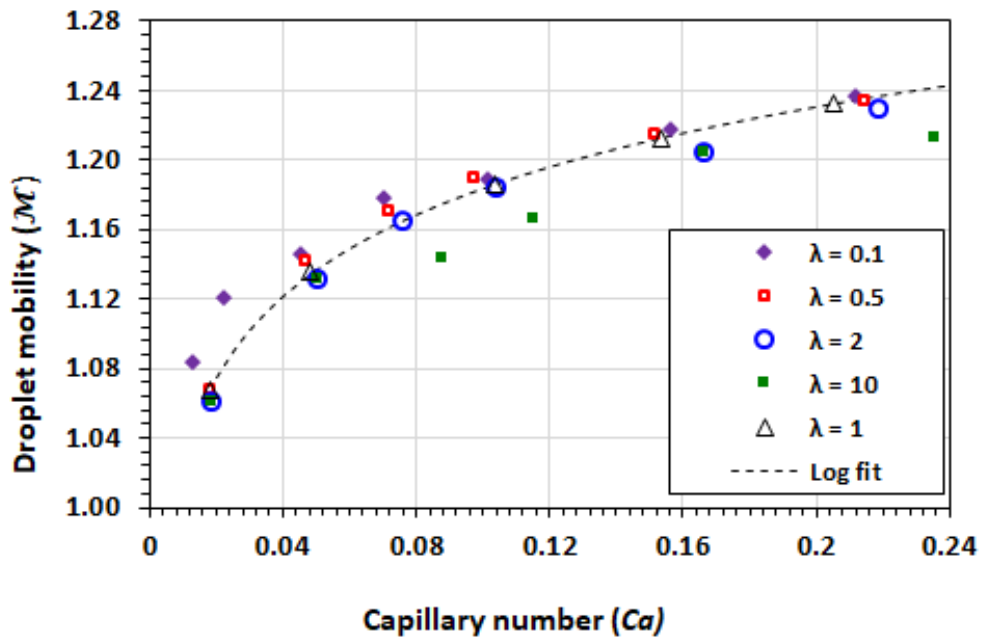


Figure 5.6 Plot of droplet mobility (\mathcal{M}) versus capillary number (Ca) for different viscosity ratios.

5.4.2 Plug shape and size

The shape of the plug is influenced by dominance of the viscous force over the capillary forces. As illustrated by the results in Figure 5.7, as the capillary

number increases, the interfacial tension is not enough to retain large curvatures of the interface, the nose sharpens and the tail flattens ($Ca = 0.3$). The tail end eventually curves inwardly as Ca increases to 0.5. The behaviour can also be attributed to increasing effect of inertial forces as the corresponding Re values are in the range $6 \leq Re \leq 72$ and We reaches 25 (Kreutzer, *et al.*, 2005).

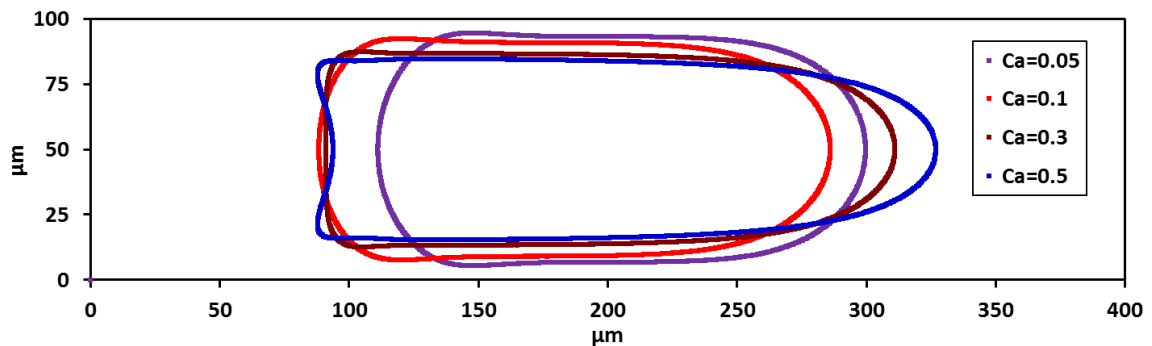


Figure 5.7 Shape of the interface of the droplet at $Ca = 0.04, 0.06$ and 0.2 .

The size of the droplet is quantified via its length and width. The widest width dimension is used as the quantifying metric, given the width of tapering droplets is not uniform. The thickness of the wetting film is based on the inverse of the same principle (*i.e.* minimum thickness). Figure 5.8 illustrates the measurement of droplet width, droplet length and minimum film thickness (Walker, 2016).

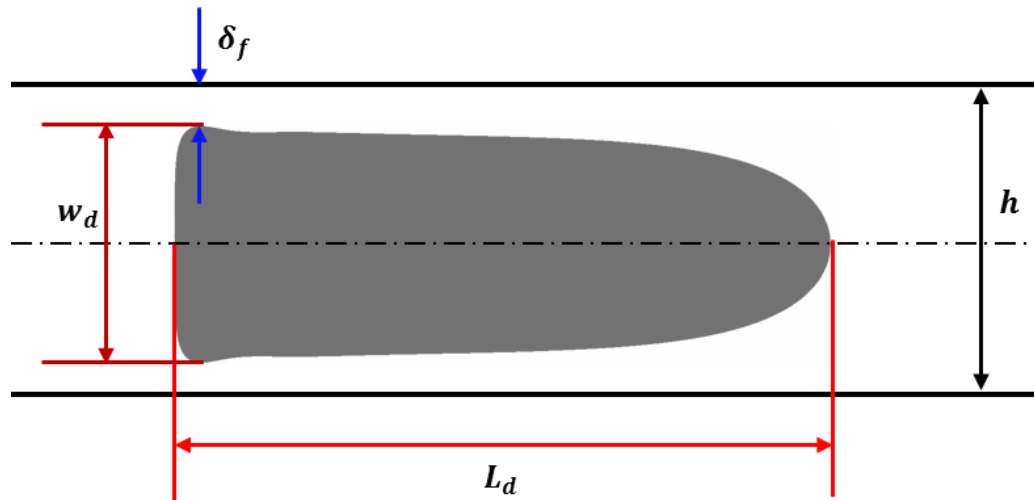


Figure 5.8 Illustration for characterisation of the droplet length (L_d), width (w_d) and minimum film thickness (δ_f).

The dependence of the non-dimensionalised droplet length on the capillary number is shown in plotted results in Figure 5.9. The droplets become increasingly elongated as the capillary number increases. The droplets at viscosity ratios of 2 and 10 experience more deformation than for $\lambda \leq 1$.

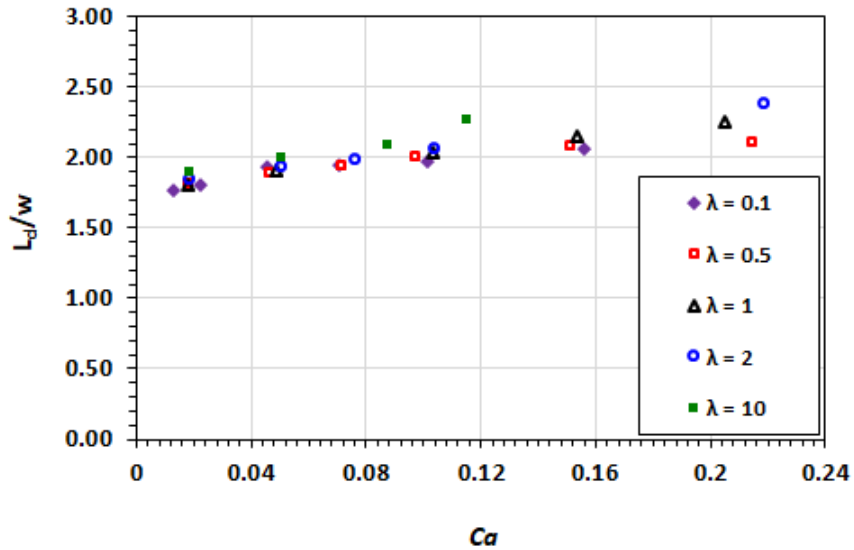


Figure 5.9 Dependence of the non-dimensionalised droplet length (L_d/w) on capillary number (Ca) at varying viscosity ratios.

Similarly, the width of the droplets decreases with increasing capillary number, as shown in Figure 5.10. The contribution of the droplet viscosity in the overall domination of interfacial effects by viscous effects is demonstrated by the greater deformation of the droplets at $\lambda > 1$.

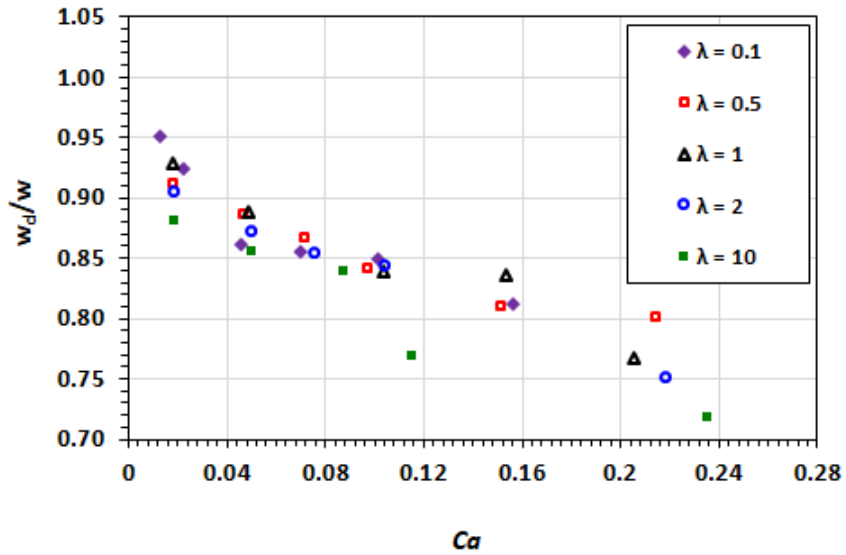


Figure 5.10 Dependence of the non-dimensionalised droplet width (w_d/w) on capillary number (Ca) at varying viscosity ratios.

The dependencies of droplet length and width on droplet mobility is similar to that of the capillary number as shown in Figure 5.11 and Figure 5.12. The deformation (increasing length and narrowing width) of the droplet increases with the increasing droplet mobility. The high viscosity ratio exhibits greater deformation due to increased viscous effects. These viscous effects are not captured in the capillary number.

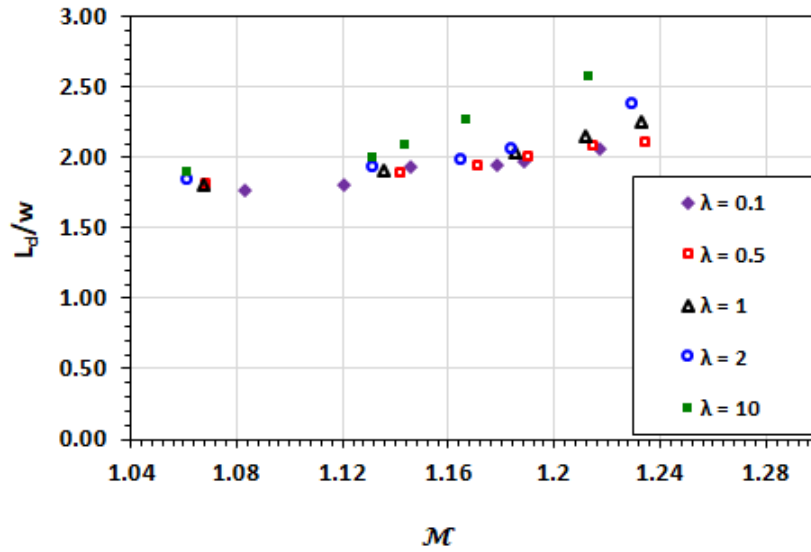


Figure 5.11 Dependence of the non-dimensionalised length (L_d/w) on droplet mobility (\mathcal{M}) at varying viscosity ratios.

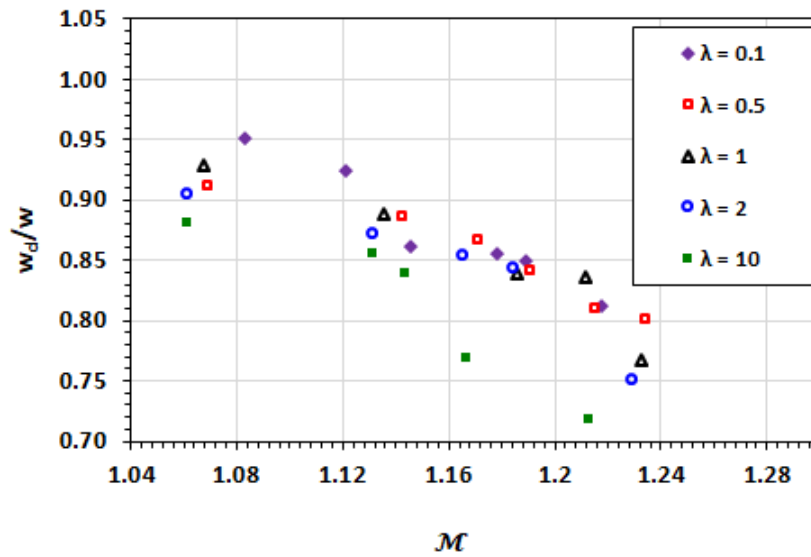


Figure 5.12 Dependence of the non-dimensionalised width (w_d/w) on droplet mobility (\mathcal{M}) at varying viscosity ratios.

5.4.3 Film thickness

Figure 5.13 shows the plot of the scaled film thickness at various capillary numbers for a range of viscosity ratios. The minimum film thickness increases with the increasing capillary number. This is as the result of the viscous effects becoming more dominant than the interfacial tension and therefore deformation of the interface. For $Ca < 0.1$ the film thickness demonstrates minimal dependence on the viscosity ratio. There is, however, a demonstrable influence of the viscosity of the droplet phase which is higher than the carrier phase (*i.e.* $\lambda > 1$). The contribution of the viscosity of the droplet phase has traditionally been neglected in the analysis of the competition between the viscous and interfacial effects. The case in point is the determination of capillary number based only on the viscosity of the carrier phase. The current results suggest that in cases where the viscosity of the droplet phase is greater than unity, the capillary number may not be sufficient on its own to the visco-capillary behaviour of the droplet flow.

The corresponding plot (Figure 5.14) of the scaled film thickness versus droplet plot mobility for different viscosity ratios demonstrates that similarly to the case of the capillary number, the scaled film thickness increases with the increasing droplet mobility. At higher viscosity ratios ($\lambda \geq 2$), the dominant viscous effects result in an increased deformation of the droplet (*i.e.* large film thickness), due to the combination of high droplet viscosity and droplet mobility. This observation is patent for the case of $\lambda = 10$.

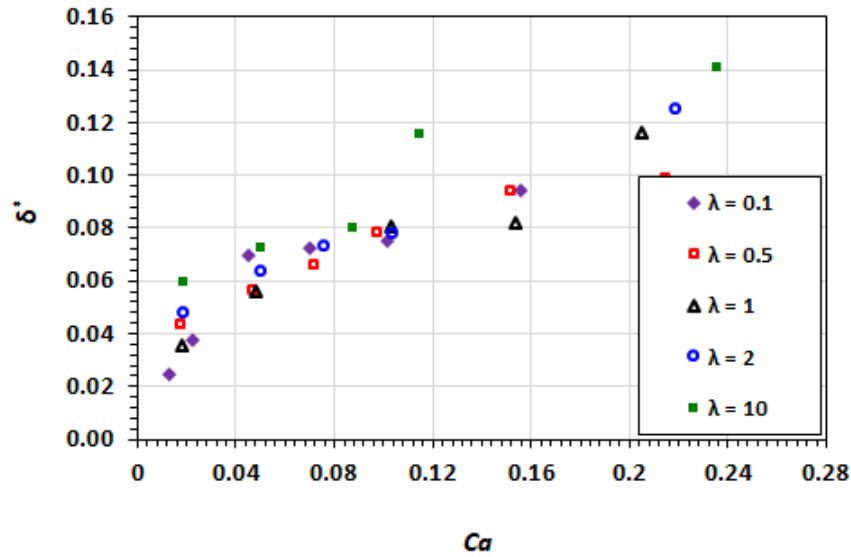


Figure 5.13 Dependence of the scaled film thickness (δ^*) on capillary number (Ca) at different viscosity ratios.

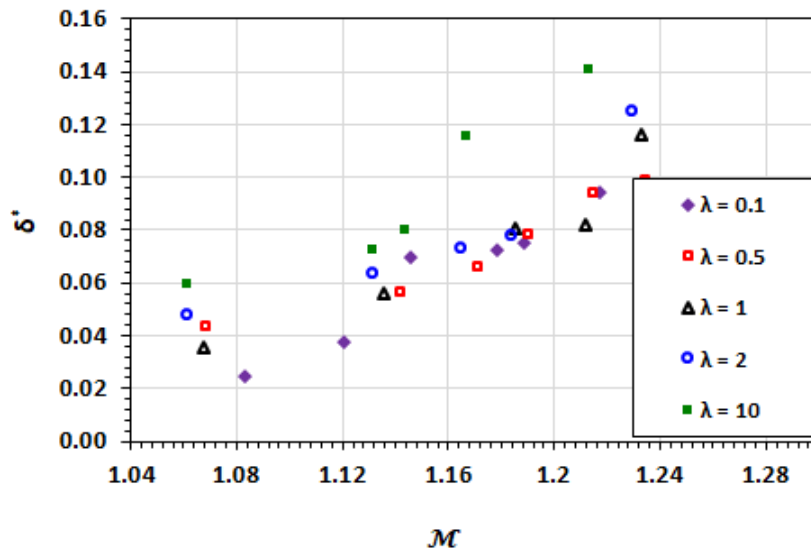


Figure 5.14 Dependence of the scaled film thickness (δ^*) on droplet mobility (\mathcal{M}) at different viscosity ratios.

Boudreaux (2016) found that for capillary numbers above 0.3, the change in behaviour was present even for viscosity ratios of 0.5 and 1.

5.4.4 Velocity field

The velocity field, particularly with the droplet, directly drives the convective transport and mixing. The recirculation creates vortices in symmetry on the centre line along the x-axis. In diffusion dominated flow the vortices enhance mixing by reducing the diffusion path length of the solute (Handique & Burns, 2001; Tice *et al.*, 2003).

The recirculatory flow leads to stagnation zones where $\|\mathbf{u}\| \rightarrow 0$. The stagnation zones manifest as regions of poor mixing during mass transport dominated by convection. The viscosity ratio between the two liquid phases also influences the nature and the extent of the recirculation.

The recirculating flow in the droplet is induced by the flow field of the carrier fluid. The wall shear has a strong influence on the flow on both phases and influences the recirculating flow drives the convective mixing. The contrast in wall shear between $\lambda = 0.5$ and $\lambda = 2$ is an order of magnitude (Figure 5.15 to Figure 5.18).

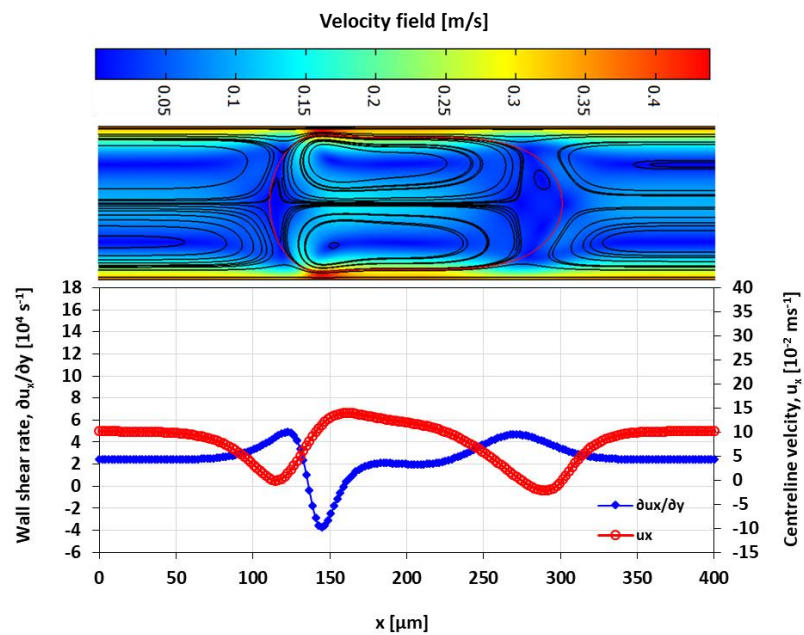
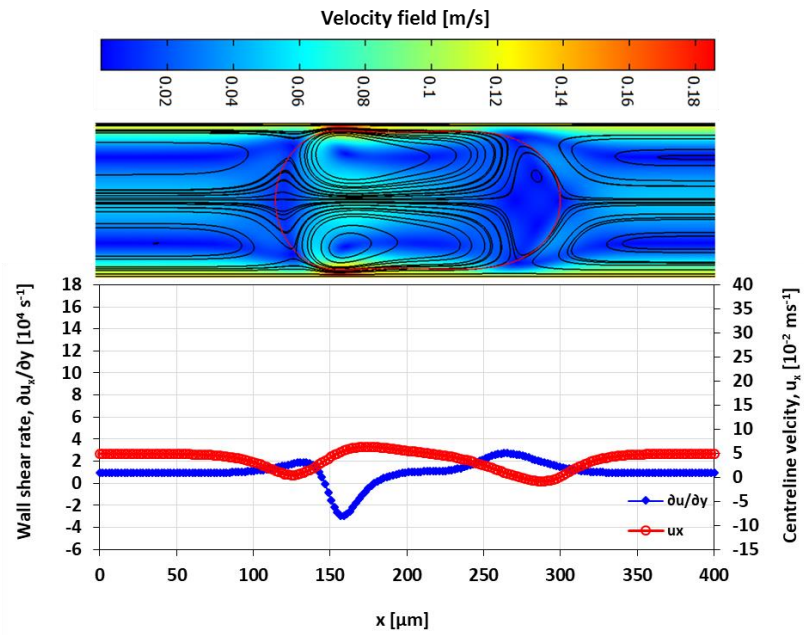


Figure 5.15 Wall shear rate and x -velocity along the centreline ($y = h/2$) at $\lambda = 2$.

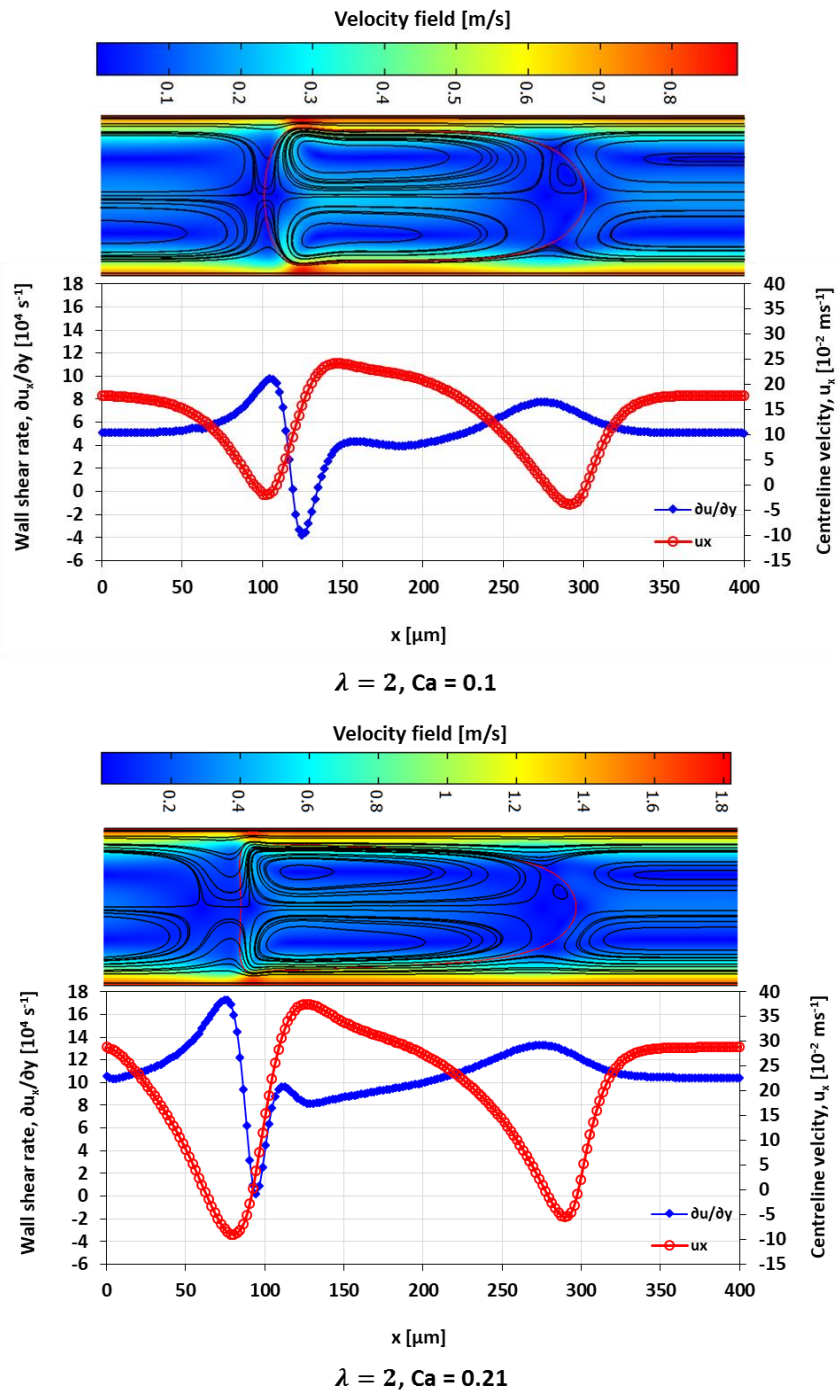


Figure 5.16 Wall shear rate and the x-velocity at centreline ($y = h/2$) for $\lambda = 0.5$.

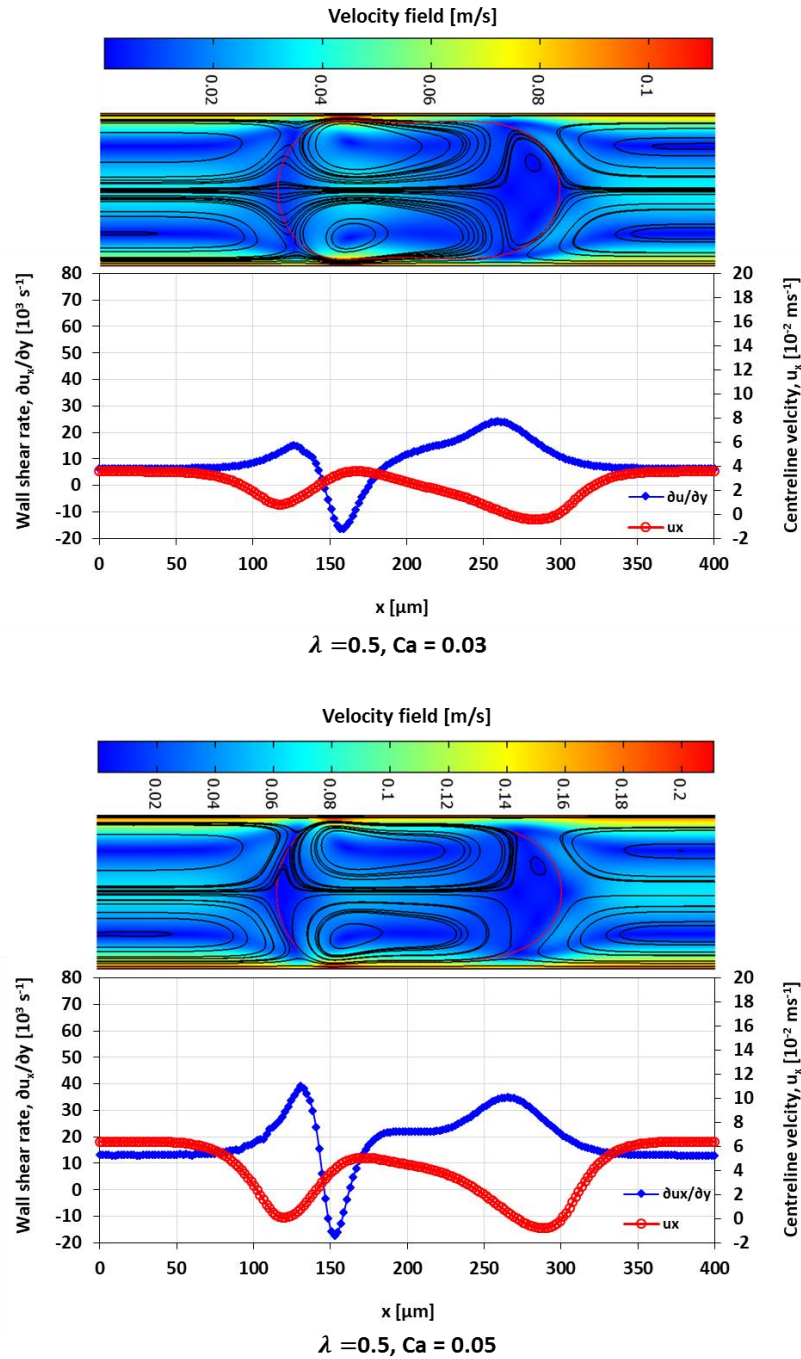


Figure 5.17 Wall shear rate and the x-velocity at centreline ($y = h/2$) for $\lambda = 0.5$.

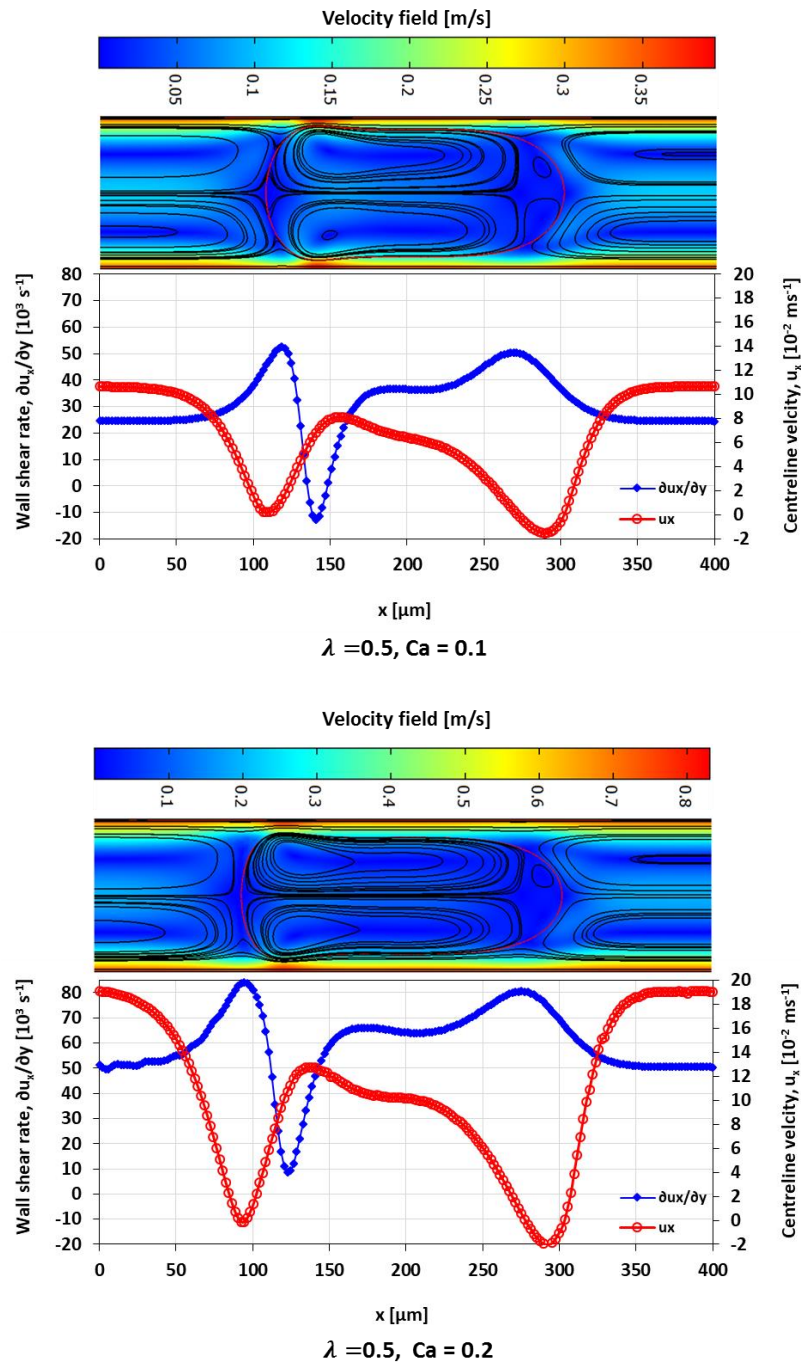


Figure 5.18 Wall shear rate and the x-velocity at centreline ($y = h/2$) for $\lambda = 2$.

5.5 Numerical results for the concentration field and mixing performance

5.5.1 Mixing index

Generally, it is desirable for mixing operations to achieve the desired mixing in the quickest time and shortest channel distance. More often than not, the targeted result of mixing is to obtain a homogenous mixture (*i.e.* complete mixing) of the fluid elements or chemical species. The extent of mixing, at various times was quantified through the mixing index (Tung, *et al.*, 2009)

$$I_M = \left(1 - \frac{\int_{\phi \geq 0.5} |C - C_\infty| d\Omega}{\int_{\phi \geq 0.5} |C_0 - C_\infty| d\Omega} \right) \quad (5.1)$$

The values of I_M range from 0 to 1, where maximum value indicates complete mixing of the solute species to an average concentration C_∞ within the droplet. The average concentration is proportional to ratio of the area (A_0) covered by the initial maximum concentration to the total area of the droplet (A_ϕ), such that

$$C_\infty = C_0 \frac{A_0}{A_\phi} \quad (5.2)$$

In the current work A_ϕ and A_0 are determined by integration over the respective areas covered and, therefore,

$$C_\infty = C_0 \left(\frac{\int_{\phi > 0.5} \int_{C_0} d\Omega}{\int_{\phi > 0.5} d\Omega} \right) \quad (5.3)$$

This approach eliminates the need to have C_0 occupying precisely half of the droplet, and thus can be applied to cases where $A_0 \neq 0.5A_\phi$.

5.5.2 Limitation of the droplet mixing model

The problem at hand requires consideration of the mass transport within the droplet and not in the carrier phase. The manner in which this is achieved in current method is that both the diffusion coefficient and the velocity field in the carrier phase are neglected. This achieved by imposing initial and subdomain conditions (See Sub-section 5.2.6). There are some limitations on the model which relate to three key issues, namely;

- (1) Loss of molar species (or mass loss) manifesting through unbalanced and unphysical decline in concentration.
- (2) Droplet mixing cases where diffusion dominates over convective transport.
- (3) Leakage of chemical species from the droplet phase into the carrier phase.

The origin of the first issue emanates from the well-known inherent disadvantage of the level set method being poor area (volume) conservation in the level set method (Sussman, Smereka, & Osher, 1994). In the current work, the conservative level set method used for two-phase flow has good conservation as per the COMSOL implementation of the method by Olsson &

Kreiss (2005), as demonstrated in Chapter 4. However, coupling of the convection-diffusion physics to the level set function from the two-phase flow solution and imposing of subdomain and initial conditions on the phases separated by $\phi = 0.5$ shows some conservation problems.

The second issue emanates from the discontinuities in mass transfer flux across the fluid-fluid interface ($\phi = 0.5$), as the result of the imposed subdomain and initial conditions. When diffusion becomes dominant over convective mass transport, the imposed condition on the velocity field, *i.e.* $u_x = u_x|_{\phi>0.5} + (u_x|_{\phi\leq 0.5}) \cdot 10^{-3}$ and $u_y = u_y|_{\phi>0.5} + (u_y|_{\phi\leq 0.5}) \cdot 10^{-3}$, the concentration field develops numerical instabilities at the interface. The instabilities manifests as spikes ($C \gg 1$) which can grow to be of $\mathcal{O}10^2$ and above, leading to divergence of the numerical solution. Interestingly, in the case of pure diffusion, *i.e.* $u_x|_{\phi\leq 0.5} = u_x|_{\phi>0.5} = 0$ and $u_y|_{\phi\leq 0.5} = u_y|_{\phi>0.5} = 0$, the problem of the instabilities does not arise. For such a case there is good mass conservation.

The third issue arises as a result of the species at high concentration are at the interface for long periods. The high concentration gradient between fluid in the droplet and that in the carries phase drives the diffusion of traces of chemical species across the interface. This mass leakage is a function of time rather than of the mixing regime. The mass leakage will be more prevalent in

diffusion-dominated case where the mixing times are generally longer than in convection-dominated case.

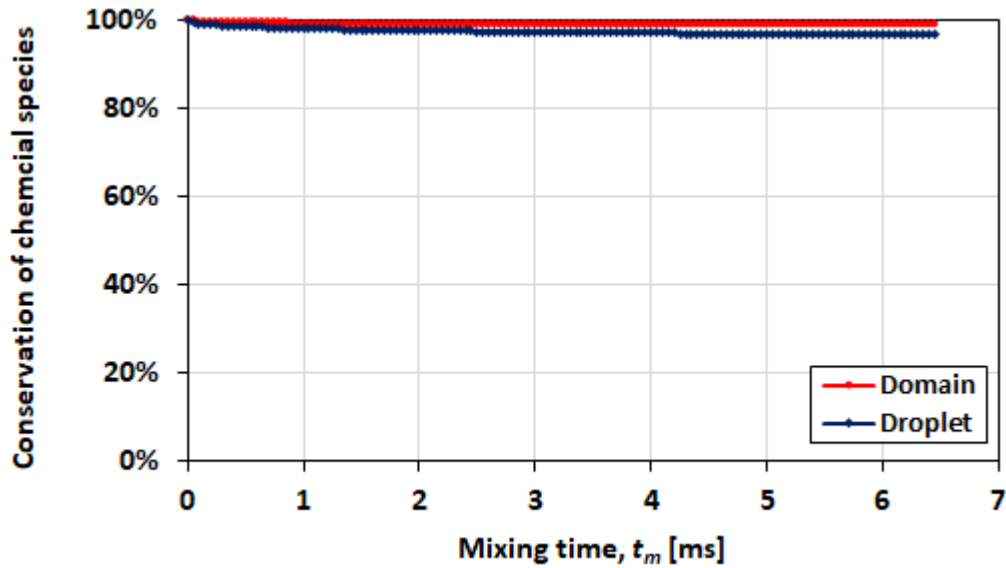


Figure 5.19 Conservation of chemical species for the convection-dominated mixing case $Ca = 0.21$, $\lambda = 0.1$.

Figure 5.19 demonstrates that there is a good conservation of the chemical species in the domain. There is, however, some mass leakage from the droplet into the carrier phase, although fairly insignificant over the mixing period with 10 ms.

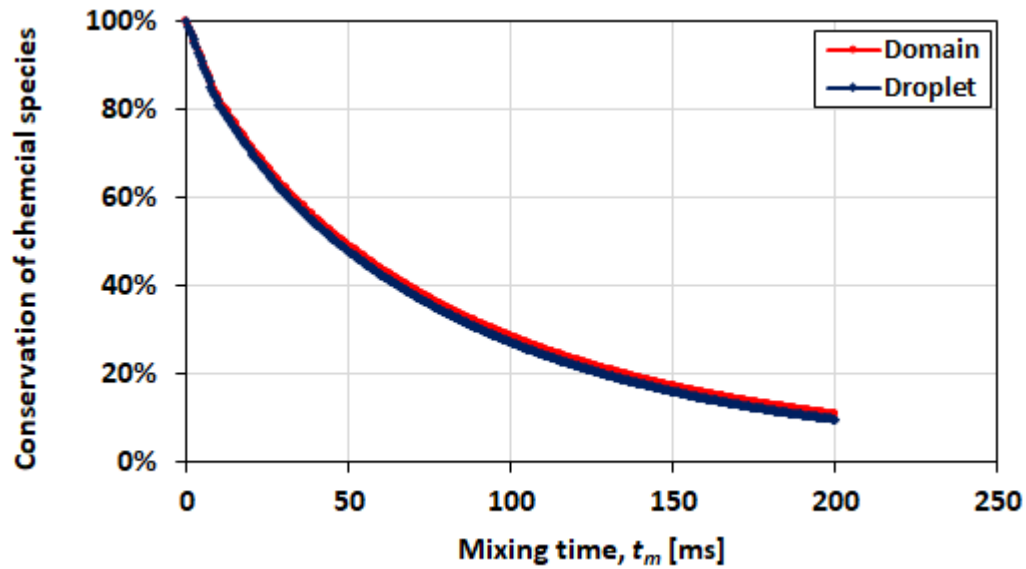


Figure 5.20 Conservation index for the diffusion-dominated mixing case $Ca = 0.018, \lambda = 2$.

In contrast, the diffusion-dominated case (Figure 5.20) has unacceptably poor conservation of the chemical species which seem to disappear from both the droplet and the domain. In 50 ms which is the order of diffusive mixing time, there is over 50% mass loss which extends to approximately 90% in 200 ms.

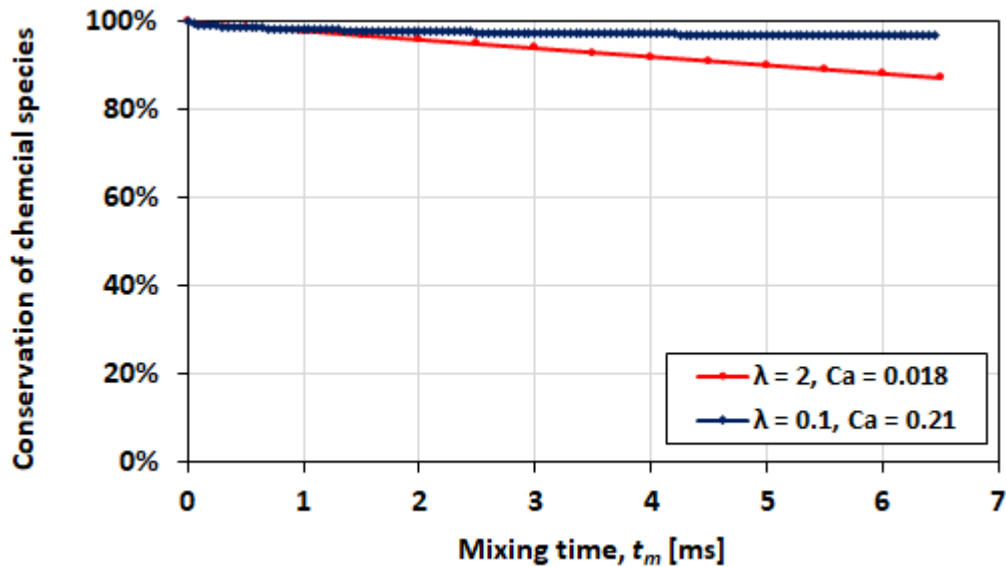


Figure 5.21 Comparison for conservation of chemical species in the droplet between two cases in 6.5 ms mixing time; the convection-dominated ($\lambda = 0.1, Ca = 0.21$) and the diffusion-dominated ($\lambda = 2, Ca = 0.018$).

When the conservation indexes in the droplet of the two cases are contrasted with respect to mixing time of 6.5 ms (Figure 5.21), it can be observed that the losses for the diffusion-dominated case exceed 10%. This result demonstrates that the conservation index worsens with mixing time. Therefore, whilst the results for diffusion-dominated cases may be inaccurate due to these losses, in the cases dominated by convection the losses are negligible.

When examining the case of only diffusion (*i.e.* mixing in a zero-velocity field), there is good conservation of the chemical species up to 5000 ms, as

shown in Figure 5.22. The species are well conserved in both the droplet and the domain.

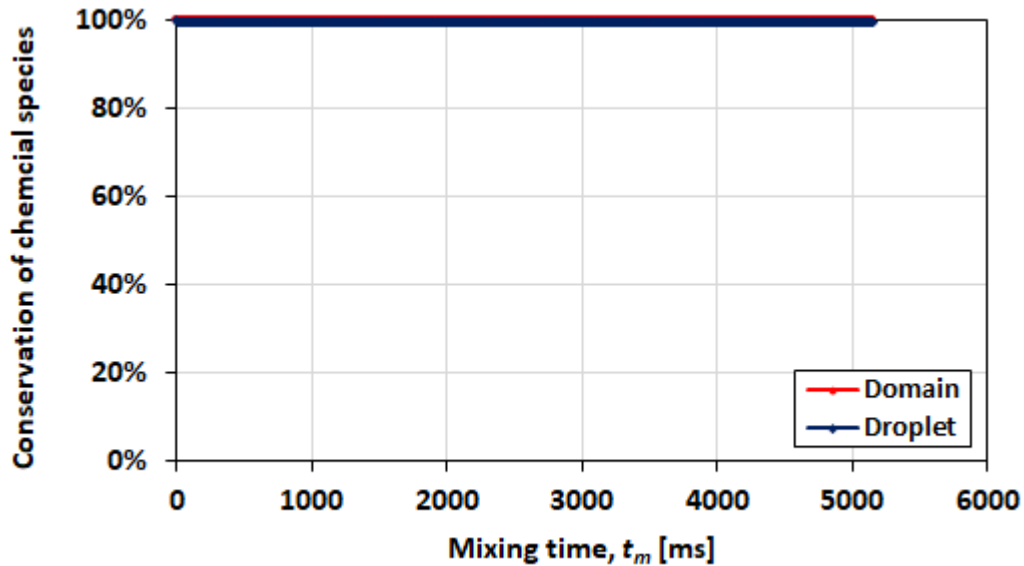


Figure 5.22 Conservation index for the diffusion only case.

The significance of this result is the demonstration that by itself, diffusion is not the cause of mass loss or leakage of the chemical species across the interface. The issue of mass loss emanates in the presence of the velocity field where diffusion dominates the mass transport physics. The results presented in the subsequent sections here are high confidence simulations where the convective mass transport dominates over diffusion and the two issues discussed in this sub-section (mass leakage and mass loss) are insignificant.

5.5.3 Effect of initial orientation of solute species

The results of the effect of the initial orientation of the solute species are shown by plotting the mixing index as a function of mixing time in Figure 5.23. The results demonstrate that for both small droplet ($L_0 = h$) and the longer plug ($L_0 = 5h$), at $Ca = 0.21$ and $\lambda = 0.1$, the transverse distribution leads to better mixing. The mixing index of approximately 0.9 is obtained in 10 ms. Contrastingly, the mixing index for axial orientation reaches between 0.8 and 0.9 for both droplet lengths in twice the mixing time of the transverse case.

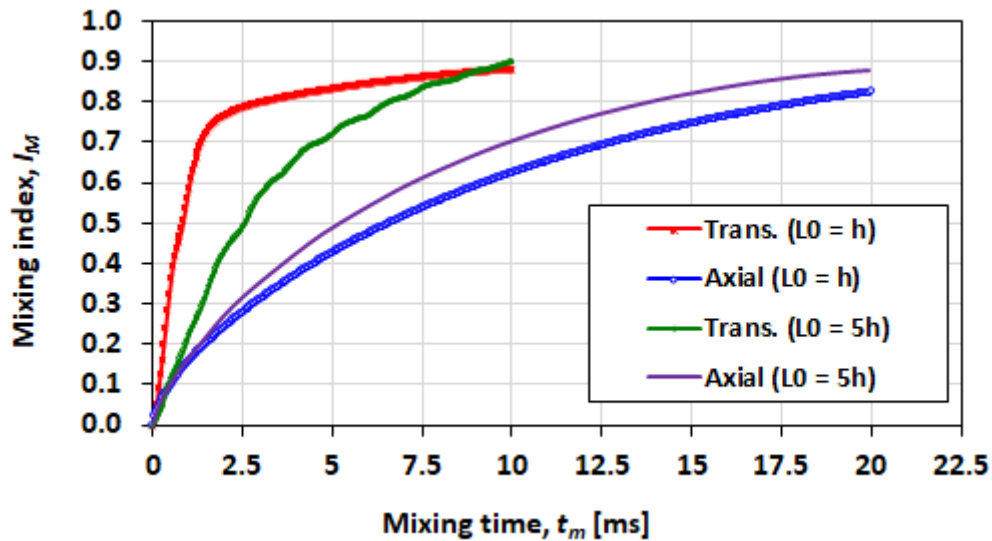


Figure 5.23 Effect of the initial mixing orientation on the mixing index for droplets of different sizes at $Ca = 0.21$ and $\lambda = 0.1$.

Figure 5.24 shows the corresponding results of the relation between the mixing index and dimensionless mixing time. The results show similar trends to those in Figure 5.23, with the non-dimensional mixing distance of 60 corresponding to 10 ms for the transverse case and 120 to 20 ms for counter case.

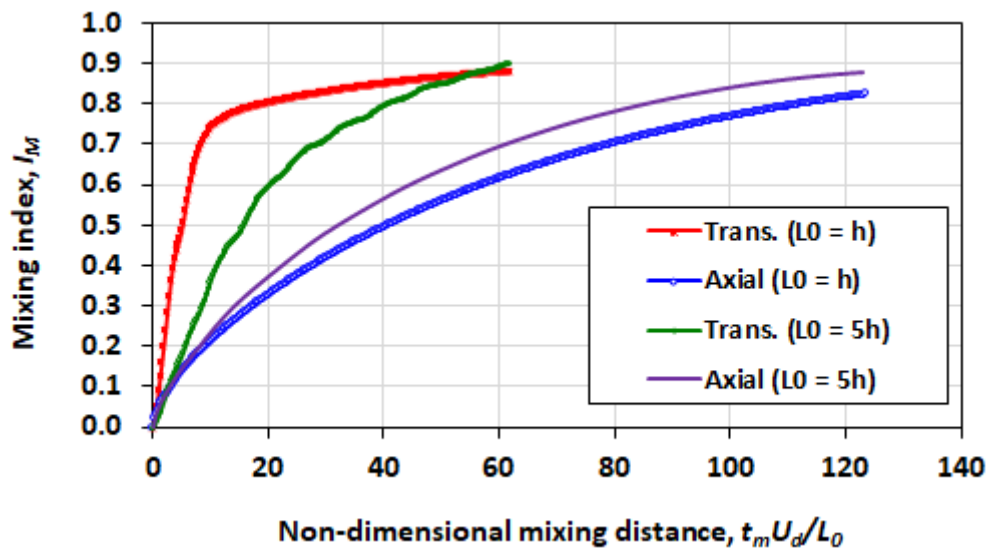


Figure 5.24 Relation between mixing index and of non-dimensional mixing distance for different the initial mixing orientations at $Ca = 0.21$ and $\lambda = 0.1$.

The observation that initial orientation of the solute has an influence of the efficiency of mixing is in agreement with previous experimental and numerical studies (Song *et al.*, 2006; Tanthapanichakoon, *et al.*, 2006a).

5.5.4 Nose stagnation zone

The nose region of the droplets exhibits poor mixing due to localised recirculatory flow within the droplet as illustrated in Figure 5.25. At the centre of the recirculation, there is a stagnation zone where convective mixing is limited. The two stagnation zones on either side of the nose of the droplet/plug form a single region which ends up with a lower concentration that the average concentration in the rest of the plug.

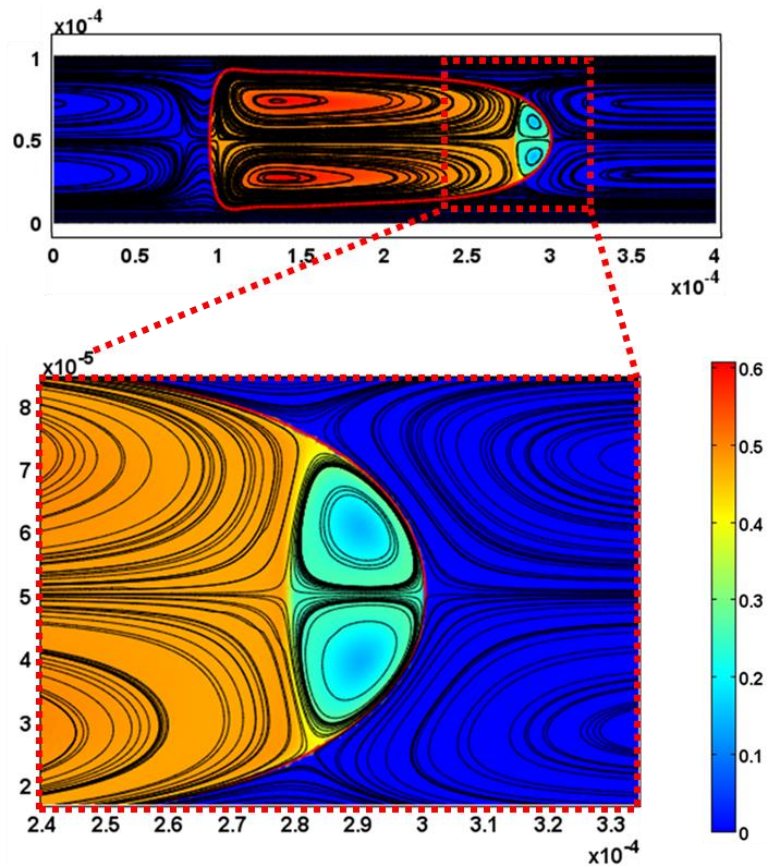


Figure 5.25 Influence of stagnation zones on poor mixing at the nose of the droplet/plug.

The size of the nose recirculation area can be quantified through horizontal length in the middle of the droplet ($y = h/2$), as a proxy measure. The x -velocity component (u_x) in the nose recirculation region is in the negative x -direction. The nose recirculation length (NRL) is given as the horizontal length where $u_x < 0$.

Figure 5.26 shows how the size of the nose recirculation length changes with the increasing capillary number. The parametric conditions for the plotted case include a viscosity ratio of 0.5 and the droplet initialised as $L_0 = 2h$.

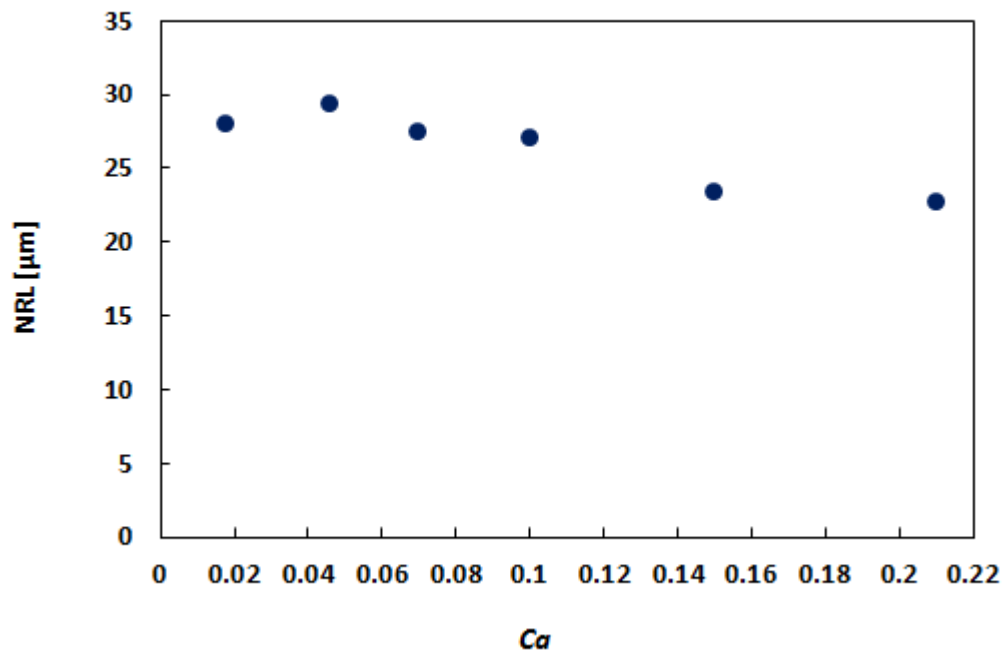


Figure 5.26 Relation between the capillary number and the nose recirculation length at $\lambda = 0.5$ and $L_0 = 2h$.

There is a general decrease in the nose recirculation length as the capillary number increases. The highest difference in the considered range of capillary numbers is 23%.

The effect of the viscosity ratio on the nose recirculation at $Ca = 0.21$ and $L_0 = 2h$ is shown in Figure 5.27. Due to the increasing viscosity of the fluid in droplet phase, the nose recirculation length increases as the viscosity ratio increases.

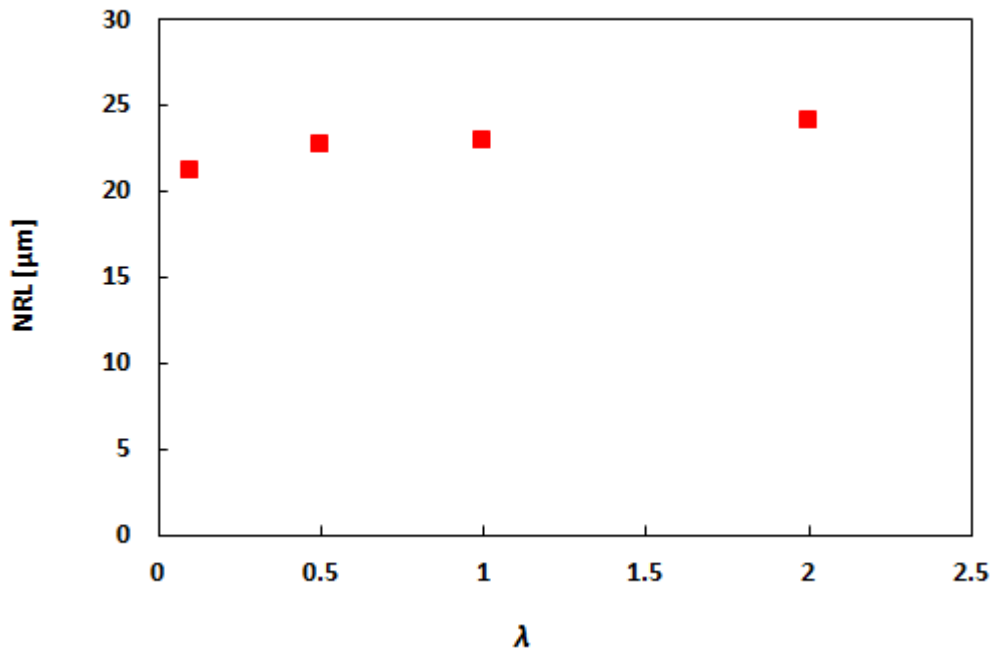


Figure 5.27 Relation between the viscosity ratio and the nose recirculation length at $Ca = 0.21$ and $L_0 = 2h$.

5.5.5 Effect of droplet size

Figure 5.28 shows plots of mixing indexes versus mixing time for three droplet lengths cases ($L_0 = h$, $L_0 = 2h$ and $L_0 = 5h$) obtained with mixing conditions of $Ca = 0.21$ and $\lambda = 0.1$ and initially transverse orientation of the chemical species.

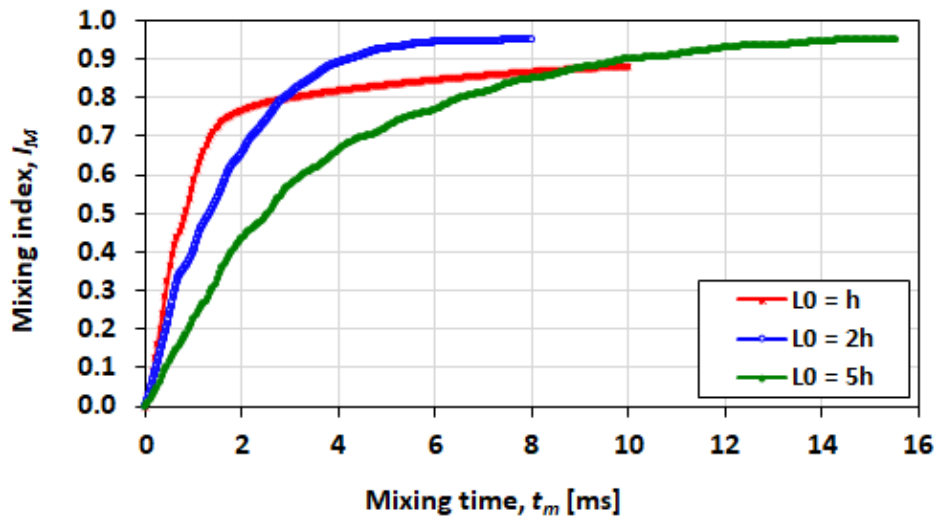


Figure 5.28 Comparison of mixing indexes for droplets with initial lengths of h , $2h$ and $5h$ and transverse solute orientation at conditions of $Ca = 0.21$ and $\lambda = 0.1$.

The smallest droplet ($L_0 = h$) exhibits faster mixing in the first 2 ms seconds as demonstrated by the steep slope. 80% of the mixing is reached in approximately 3 ms. However, after 2 ms seconds, the mixing index begins to

plateau, reaching 0.9 in nearly 10 ms. On the other hand, in the case of the intermediate droplet ($L_0 = 2h$) the mixing index of 0.9 is achieved in 4 ms and plateaus at approximately 0.95. The longest droplet (plug) case has a slower rate of mixing although the mixing index of 0.9 is also reached within 10 ms. The 0.95 mixing index is reached in 15 ms.

The corresponding plots of the mixing indexes against non-dimensional mixing distance are shown in Figure 5.29. These plots resemble the plots of the mixing index against mixing time. This is due to the fact that the flow conditions are similar, *i.e.* same viscosity ratio and droplet velocity.

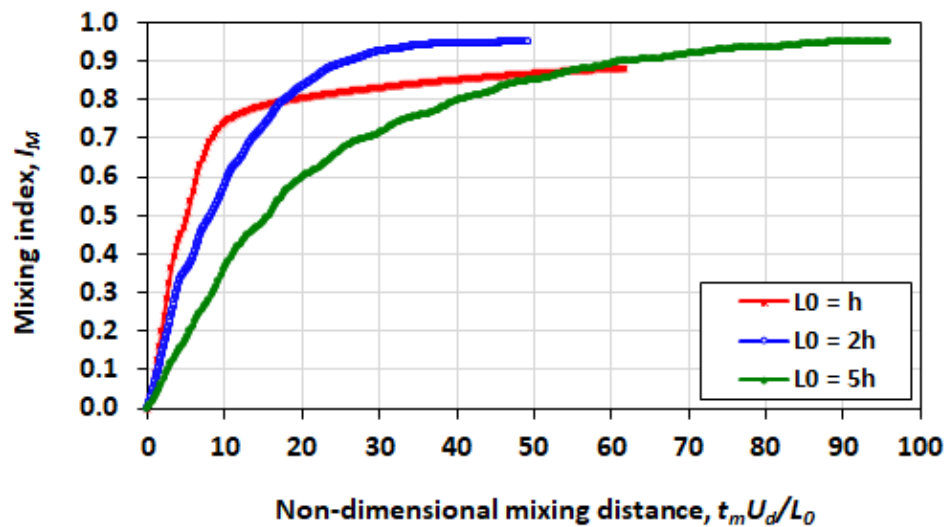


Figure 5.29 Comparison of non-dimensional mixing distance for droplets with initial lengths of h , $2h$ and $5h$ and transverse solute orientation at conditions of $Ca = 0.21$ and $\lambda = 0.1$.

The lower mixing index reached in the case of the smallest droplet can be attributed to the large (20%) nose recirculation zone relative to the droplet size. In the other droplet cases of $2h$ and $5h$, the recirculation zones account for 11% and 3%, respectively.

In the case of axial orientation (Figure 5.30) under similar flow conditions ($Ca = 0.21$ and $\lambda = 0.5$), it takes approximately 20 ms to achieve a mixing index of 0.9 for both $L_0 = 2h$ and $L_0 = 5h$. The corresponding non-dimensional mixing distances for axial orientation are at least 120 in both cases, as shown in Figure 5.31.

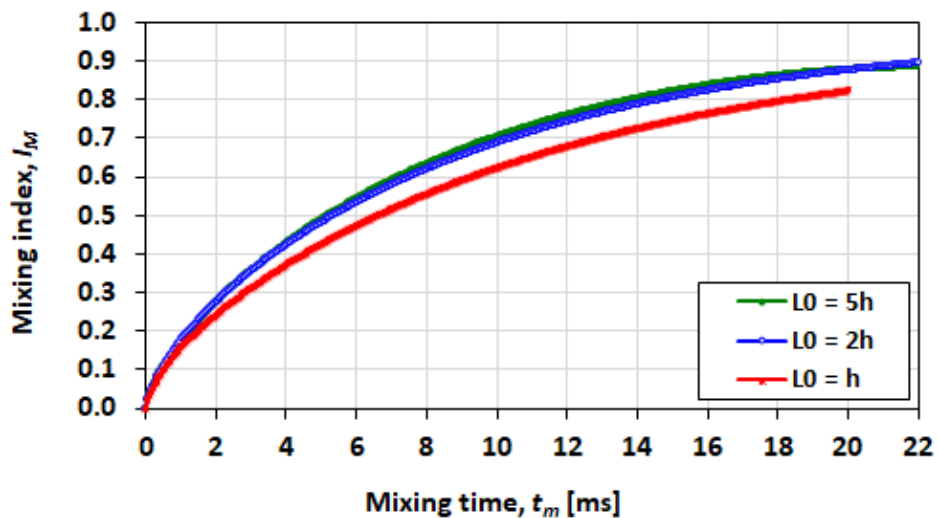


Figure 5.30 Comparison of non-dimensional mixing distance for droplets with initial lengths of h , $2h$ and $5h$ and axial solute orientation at conditions of $Ca = 0.21$ and $\lambda = 0.1$.

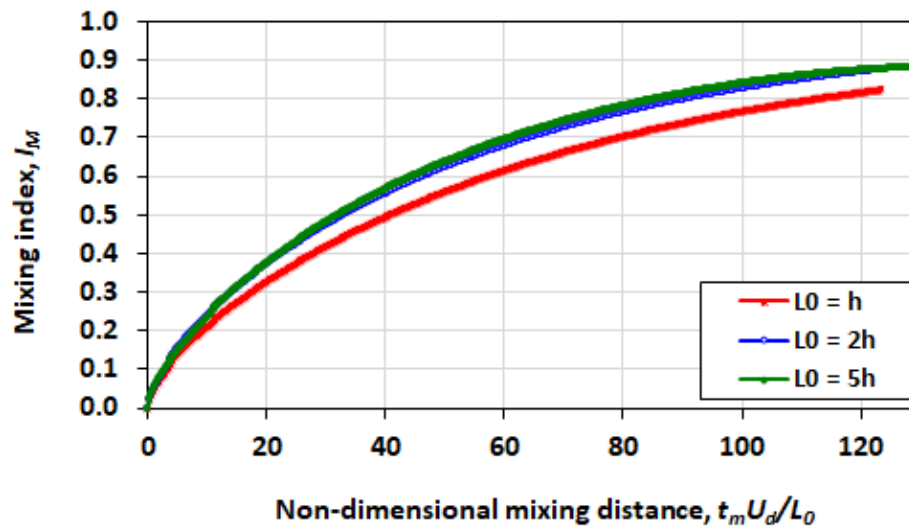


Figure 5.31 Comparison of non-dimensional mixing distance for droplets with initial lengths of h , $2h$ and $5h$ and axial solute orientation at conditions of $Ca = 0.21$ and $\lambda = 0.1$.

5.5.6 Effect of viscosity ratio

The concentration field plots for mixing at various times for $Ca = 0.21$ and $\lambda = 0.5$. are shown in Figure 5.32 and Figure 5.33 for $Ca = 0.21$ and $\lambda = 2$. The latter case exhibits slower mixing due to the higher viscosity of the fluid in the droplet.

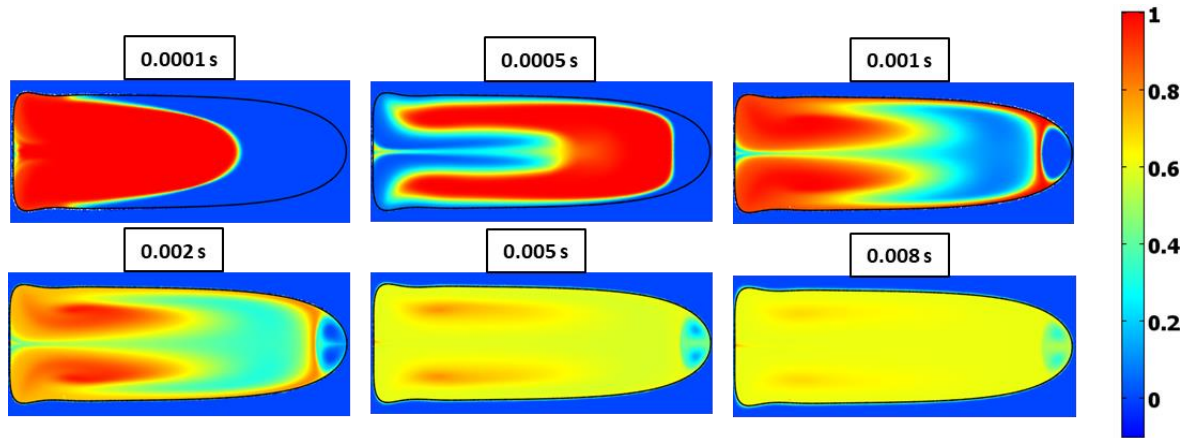


Figure 5.32 Concentration field plots of mixing at different times for $Ca = 0.21$ and $\lambda = 0.5$.

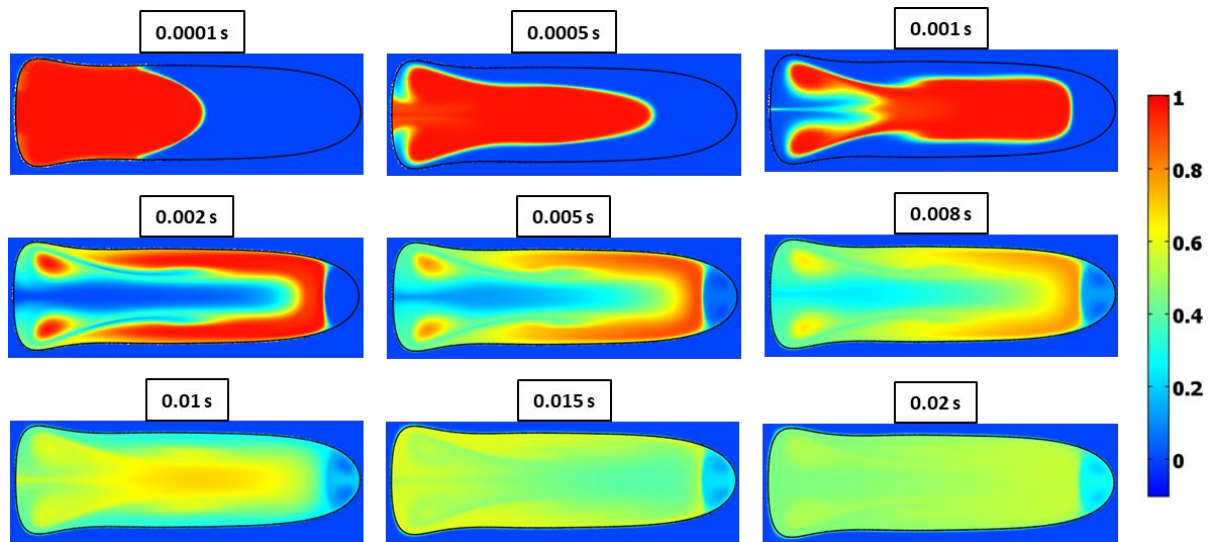


Figure 5.33 Concentration field plots of mixing at different times for $Ca = 0.21$ and $\lambda = 2$.

The mixing index plots for various viscosity ratios at $Ca = 0.21$ and $Ca = 0.15$ are given in Figure 5.34 and Figure 5.35, respectively.

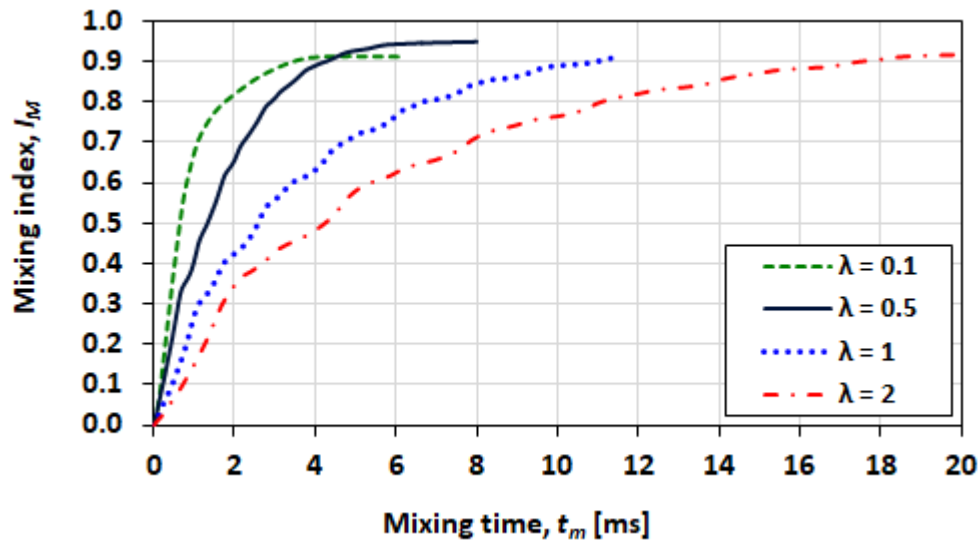


Figure 5.34 Comparison of mixing performances for various viscosity ratios at $Ca = 0.21$.

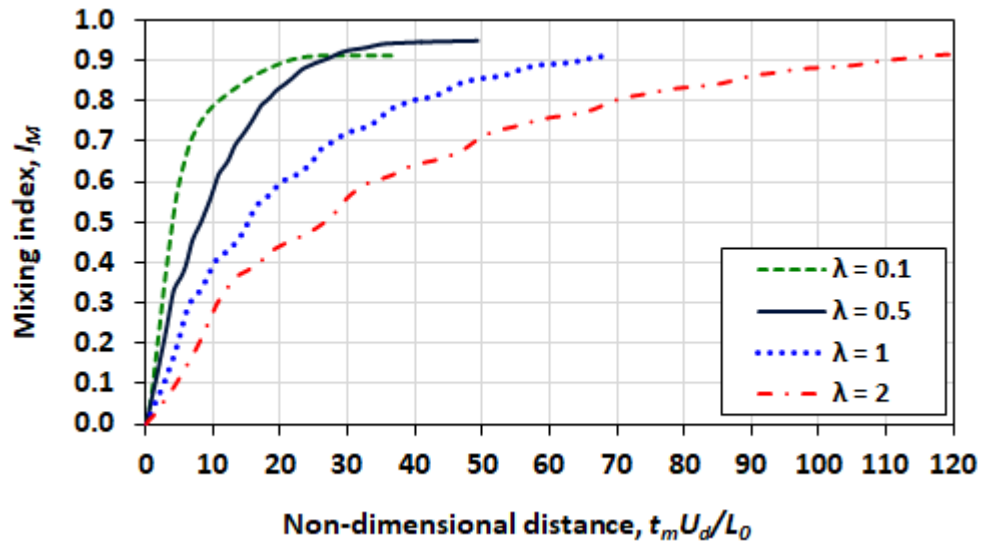


Figure 5.35 Comparison of mixing performances for various viscosity ratios at $Ca = 0.15$.

The performance of the case for $\lambda = 0.5$ has better mixing than that at $\lambda = 0.1$. These results are counter-intuitive and this result is attributed to the early plateauing of the mixing index in the case of $\lambda = 0.1$.

The plot in Figure 5.36 shows the plot of both mixing time and dimensionless mixing distance as a function of viscosity ratio at $Ca = 0.21$. Expectedly, the mixing time and the mixing distance both increase monotonically with the increasing viscosity ratio.

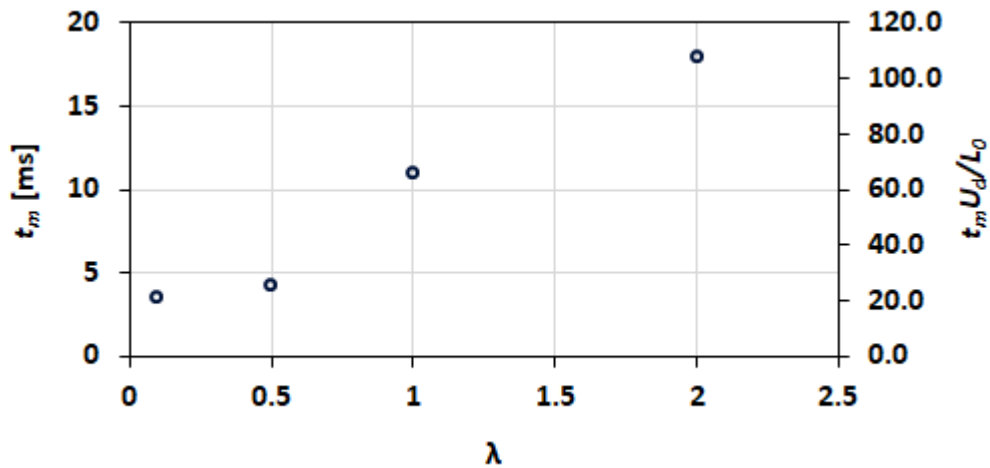


Figure 5.36 Influence of the viscosity ratio on mixing time (t_m) and dimensionless mixing distance ($t_m U_d / L_0$)

$Ca = 0.2$ and $Ca = 0.15$ provide the best mixing performance for the cases where $\lambda < 1$. The latter cases are convection-dominated and able to achieve mixing indices of above 0.85. There are three types of mixing behaviour:

- Convection-dominated mixing where at least I_M of 0.8 is achieved within 5 ms.
- Convective mixing within 5 ms, after which diffusion becomes dominant and the rate of mixing then levels out. The I_M values do not reach 0.8.
- A diffusion-dominated mixing where the mixing rate is low and it takes at least 15 ms for the rate of mixing before it begins to plateau. The results of this type of mixing are linked to the model limitations discussed in sub-section 5.5.2.

Within the studied flow conditions, achieving a mixing index of 1 is limited by poor mixing at the stagnation zone at nose of the droplet. Mixing where the carrier fluid has lower viscosity than the droplet ($\lambda = 0.5$) demonstrably has better mixing than the counter case of viscosity ratio of 2. At $Ca = 0.2$, a mixing index of 0.8 is achieved in 5 ms at $\lambda = 2$. The same mixing index is achieved at double the time in the case of $\lambda = 0.5$. Higher capillary numbers exhibit better mixing but also require long microchannels as the droplets travel at high speeds.

At capillary numbers of 0.1 and below, the mixing index curve reach the asymptotic value of around 0.8 or below. This is due to the influence of the stagnation zones.

The viscosity ratio of the droplet phase and the carrier phase does influence the flow field and, therefore, the quality of mixing in the droplet. Under conditions of similar or comparable capillary numbers, better mixing is obtained when the viscosity of the carrier fluid is lower than the droplet phase.

5.6 Conclusion

The work in the current chapter has established and demonstrated the two-phase MFR modelling approach for studying mixing in a droplet/plug moving in a straight microchannels. The applicability of the method is limited at low capillary numbers where the corresponding droplet mobility tends to unity. The convection-diffusion solution yields low confidence results when the mixing is diffusion dominated. In consideration of these limitations, some parametric guidelines (design rules) are postulated for use of the method: capillary number ($Ca > 0.02$), Reynolds number ($Re \lesssim 100$), droplet mobility ($\mathcal{M} > 1$, for $\mathcal{M} \approx 0.0675 \ln Ca + 1.339$) and viscosity ratio ($\lambda < 1$).

The simulation results demonstrate the sensitivity of the initial distribution of solute species, concurring with existing studies (Fu, *et al.*, 2018; Sarrazin, *et al.*,

2006). Solute species initially positioned in transverse orientation mix faster than the axial arrangement where the solute species are positioned symmetrically in long plugs. This advantage is not distinct in the case where the droplet has a length comparable to its width. Both the viscosities of the individual phases, as well as their viscosity ratios influence the extent (time and space) and the quality of mixing (mixing index).

"I think and think for months and years. Ninety-nine times, the conclusion is false. The hundredth time I am right." -- Albert Einstein

Chapter 6

Conclusion

6.1 General discussion

Mixing phenomena in microfluidic droplets is crucial for various applications of droplet microfluidics. This work investigated the factors that influence mixing in microfluidic droplets and plugs using numerical simulations. COMSOL Multiphysics™ was utilised as the numerical tool, subsequent to being validated using a set of benchmark cases. There is currently no standardisation of CFD benchmark cases for microfluidics and the cases were implemented as *ad hoc* cases. Although these are referred to as 'weak sense benchmarks', they are recognised to fulfil a vital role in the absence of standard benchmark cases which are set by engineering bodies across the CFD field (Oberkampf & Trucano, 2002). One of the key advantages of utilising CFD is that it can offer benefits linked to lower costs and complexity of setting up when experimental approaches. However, in some cases for analysis, the computational costs with regards to both time and equipment requirements, can be limiting. In such instances, trade-offs can be made between ideal result or model and abstract results or simplified model. For example, the 2D model implemented was able to provide suitable results at

an affordable computational cost in terms of time and resources, in contrast to the case of a 3D model.

The advantages of utilising two-phase moving-frame-of-reference modelling approach in problems such as those involving heat and mass transfer are covered in detail in literature (Taha & Cui, 2005; Talimi 2012). The approach's lower computational cost than, for example, two-phase fixed-frame-of-reference is asserted in the current work as one of such advantages. A basic benchmarking study to illustrate the latter point is presented in Appendix D.

6.2 Summary of key contributions

The contributions of the current work are summarised as follows:

- A set of benchmark cases were implemented for the purpose of validating a commercially-available numerical tool, COMSOL Multiphysics™, for modelling a combination of two-phase flow and mass transport in droplet microfluidics systems.
- A two-phase moving-frame-of-reference modelling approach underpinned on finite element and level set methods (offered in COMSOL Multiphysics™) has been presented and demonstrated to be appropriate for investigation of mixing within droplets travelling in straight microchannels. This approach had not been previously demonstrated for the problem of mixing in droplet microfluidics requires

less computational resources compared to the fixed frame-of-reference approach.

- The work identified specific limitations of method, namely; for flow conditions where the droplet mobility approaches unity as well as conditions where diffusion mixing dominates convective conditions. Some basic guidelines (design rules) based on key parameters were postulated.
- The major result of this work is the demonstration of reduced mixing at the nose region of the droplet/plug. Little attention has previously been given to the mixing in this region. Under conditions of high viscosity ratio ($\lambda > 1$) and initially transverse configuration of the chemical species, mixing may be insufficient at the nose region.
- The viscosity of the carrier phase, the viscosity of the droplet phase, and their ratio, have been demonstrated to play significant roles, in agreement with existing studies. This work also demonstrated that the viscosity of the droplet phase is equally important for mixing.
- It has been shown that the problem of reactant wastage through nose recirculation may be minimised by using a high-viscosity fluid as carrier phase. This solution is applicable if the viscosity ratio is less than unity.

6.3 Conclusions

The key conclusions from this work can be summarised as follows:

- Mixing in microchannels is governed by a number of factors which can be lumped into key parameters.
- As the length of the plug increases ($L_d \gg w_d$), the efficiency of the mixing is reduced.
- The initial orientation of the droplet influences the mixing and the transverse orientation provides better mixing performance than the axial orientation.
- The recirculation inside the droplet depends on the superficial velocity and the viscosity ratio.

6.4 Recommendations for future work

The recommendations emanating from this work are given as follows:

- Further improvement on the model is necessary to enable capturing of diffusion-dominated mixing characterised by long mixing times. This improvement will enable to expand the scope of application of the model.
- Implementation of a periodic boundary condition, to assess the influence of the droplet spacing and frequency on the mixing inside the droplet. The current study looked at an isolated droplet to provide fundamental details, however, microfluidic applications generally utilise microfluidic droplet trains.

- Investigation on the influence of viscosity on the mixing. This study will provide an understanding of how mixing of fluid with concentration dependent viscosity will behave.
- Numerical investigation of mixing in cases where either or both of the fluid phases are non-Newtonian fluids. Certain solutions or suspensions encountered in microfluidics, such as of macromolecules and certain proteins, exhibit non-Newtonian flow characteristics. Studies into such cases will expand the knowledge of droplet mixing necessary for relevant applications.

References

- Abdollahi, A., Sharma, R. N., & Vatani, A. (2017). Fluid flow and heat transfer of liquid-liquid two phase flow in microchannels: A review. *International Communications in Heat and Mass Transfer*, 84(1), 66-74.
- Afkhami, S., Leshansky, A. M., & Renardy, Y. (2011). Numerical investigation of elongated drops in a microfluidic T-junction. *Physics of Fluids*, 23, 022002 1-14.
- Aris, R. (1956). On the dispersion of a solute in a fluid flowing through a tube. *Mathematical and Physical Sciences*, 235(1200), 67-77.
- Aubin, J., Ferrando, M., & Jiricny, V. (2010). Current methods for characterising mixing and flow in microchannels. *Chemical Engineering Science*, 65, 2065-2093.
- Aussillous, P., & Quéré, D. (2000). Quick deposition of a fluid on the wall of a tube. *Physics of Fluids*, 12(10), 2367-2371.
- Bandara, T., Nguyen, N.-T., & Rosengarten, G. (2015). Slug flow heat transfer without phase change in microchannels: A review. *Chemical Engineering Science*, 126(1), 283-295.
- Baroud, C. N., Gallaire, F., & Dangla, R. (2010). Dynamics of microfluidic droplets. *Lab on a Chip*, 10, 2032-2045.
- Bordbar, A., Taassob, A., Zarnaghsh, A., & Kamali, R. (2018). Slug flow in microchannels: Numerical simulation and applications. *Journal of Industrial and Engineering Chemistry*, 62(1), 26-39.
- Bothe, D. (2010). Evaluating the quality of a mixture: degree of homogeneity and scale of segregation. In H. Bockhorn, D. Mewes, W. Peukert, & H.-J. Warnecke (Eds.), *Micro and Micro Mixing* (pp. 17-35). Heidelberg: Springer.

References

- Boudreaux, J. M. (2015). *Exploration of Segmented Flow in Microchannels using the Volume of Fluid Method in ANSYS Fluent*. Master's Thesis: Louisiana State University (LSU). Retrieved from https://digitalcommons.lsu.edu/gradschool_theses/1945
- Brackbill, J. U., Kothe, D. B., & Zemach, C. (1992). A continuum model for modeling surface tension. *Journal of Computational Physics*, 100, 335-354.
- Bretherton, F. B. (1961). Motion of long bubbles in tubes. *Journal of Fluid Mechanics*, 10(02), 166- 188.
- Bringer, M. R., Gerdts, C. J., Song, H., Tice, J. D., & Ismagilov, R. F. (2004). Microfluidic systems for chemical kinetics that rely on chaotic mixing in droplets. *Philosophical Transactions of the Royal Society of London*, 362, 1087-1104.
- Bruneau, C. -H., Colin, T., Galusinski, C., Tancogne, S., & Vigneaux, P. (2008). simulations of 3D dynamics of microdroplets: A comparison of rectangular and cylindrical channels. *7th European Conference on Numerical Mathematics and Advanced Applications* (pp. 449-456). Graz: Springer.
- Bruus, H. (2008). *Theoretical Microfluidics*. Oxford: Oxford University Press.
- Burns, J. R., & Ramshaw, C. (2001). The intensification of rapid reactions in multiphase systems using slug flow in capillaries. *Lab on a Chip*, 1, 10-15.
- Che, Z., Wong, T. N., & Nguyen, N. -T. (2010). An analytical model for a liquid-liquid plug moving in curved microchannels. *International Journal of Heat and Mass transfer*, 53, 1977-1985.
- Chen, X., Li, T., & Hu, Z. (2016). A novel research on serpentine microchannels of passive micromixers. *Microsystem Technologies*, 1-8. doi:10.1007/s00542-016-3060-7

References

- Cherlo, S. K., Kariveti, S., & Pushvanam, S. (2010). Experimental and numerical investigations of two-phase (liqui-liquid) flow behaviour in rectangular mirochannels. *Industrial and Engineering Chemistry Research*, 49(1), 893-899.
- Christopher, G. F., & Anna, S. L. (2007). Microfluidic methods for generating continuous streams. *Journal of Physics D: Applied Physics*, 40, R319-R336.
- Chung, B. G., Lee, K.-H., Khademhosseini, A., & Lee, S.-H. (2012). Microfluidic fabrication of microengineered hydrogels and their application in tissue engineering. *Lab on a Chip*, 12, 45–59.
- Comsol AB. (2008a). *COSMOSOL Multiphysics 3.5a User's Guide*. Stockholm: Comsol AB.
- Comsol AB. (2008b). *COMSOL Multiphysics 3.5a Modelling Guide*. Stockholm: Comsol AB.
- Danckwerts, P. (1952). The definition and measurement of some characteristics of mixtures. *Applied Scientific Research, Section A*, 3(4), 279–296.
- Dangla, R., Kayi, S. C., & Baroud, C. N. (2013). Droplet microfluidics driven by gradients of confinement. *Proceedings of the National Academy of Sciences*, 110(3), 853-858.
- Das, D., Biswas, K., & Das, S. (2014). A microfluidic device for continuous manipulation of biological cells using dielectrophoresis. *Medical Engineering & Physics*, 36(6), 726-731.
- de Gennes, P.-G., Brochard-Wyart, F., & Quéré, D. (2004). *Capillarity and wetting phenomena: drops bubbles, pearls, waves*. (A. Reisinger, Trans.) New York: Springer.
- Dittrich, P. S., & Manz, S. (2006). Lab-on-a-chip: microfluidics in drug discovery. *Nature Reviews: Drug Discovery*, 5, 210-218.

References

- Dore, V., Tsaoulidis, D., & Angeli, P. (2012). Mixing patterns in water plugs during water/ionic liquid segmented flow in microchannels. *Chemical Engineering Science*, 80, 334–341.
- Erickson, D. (2005). Towards numerical prototyping of labs-on-chip: modeling for integrated microfluidic devices. *Microfluidics and Nanofluidics*, 1, 201-318.
- Filipovic, N., Ivanovic, M., & Kojic, M. (2009). "A comparative numerical study between dissipative particle dynamics and smoothed particle hydrodynamics when applied to simple unsteady flows in microfluidics. *Microfluidics and Nanofluidics*, 7(2), 227-235.
- Fu, Y., Bai, L., Zhao, S., Zhang, X., Jin, Y., & Cheng, Y. (2018). Simulation of reactive mixing behaviors inside micro-droplets by a lattice Boltzmann method. *Chemical Engineering Science*, 181(1), 79-89.
- Godin, J., Chen, C.-H., Cho, S. H., Qiao, W., Tsai, F., & Lo, Y.-H. (2008). Microfluidics and photonics for Bio-System-on-a-Chip: A review of advancements in technology towards a microfluidic flow cytometry chip. *Journal of Biophotonics*, 1(5), 355-376.
- Gulati, S., Rouilly, V., Niu, X., Chappell, J., Kitney, R. I., Edel, J. B., . . . deMello, A. J. (2009). Opportunities for microfluidic technologies in synthetic biology. *Journal of Royal Society Interface*, 1-14. doi:10.1098/rsif.2009.0083.focus
- Hale, C., & Darabi, J. (2018). Computational Analysis of a Microfluidic Magnetophoretic Device for DNA Isolation. *ASME 2018 5th Joint US-European Fluids Engineering Division Summer Meeting* (pp. V003T21A011-V003T21A011). American Society of Mechanical Engineers.
- Handique, K., & Burns, M. A. (2001). Mathematical modeling of drop mixing in a slit-type microchannel. *Journal of Micromechanics and Microengineering*, 11, 548–554.

References

- Hirt, C. W., & Nichols, B. D. (1981). Volume of fluid (VOF) method for the dynamics of free boundaries . *Journal of Computational Physics*, 39(1), 201-225.
- Hoang, D. A., Steijn, V. v., Portela, L. M., Kreutzer, M. T., & Kleijn, C. R. (2013). Benchmark numerical simulations of segmented two-phase flows in microchannels using the Volume of Fluid method. *Computers & Fluids*, 86, 28-36.
- Hua, H., Shin, J., & Kim, J. (2014). Level Set, Phase-Field, and Immersed Boundary Methods for Two-Phase Fluid Flows. *Journal of Fluids Engineering*, 136, 021301 1-14.
- i Solvas, X. C., Srisa-Art, M., deMello, A. J., & Edel, J. B. (2010). Mapping of fluidic mixing in microdroplets with 1 us time resolution using fluorescence lifetime imaging. *Analytical Chemistry*, 82, 3950-3956.
- Israelachvili, J. N. (2011). *Intermolecular and surface forces* (3rd ed.). Amsterdam: Academic Press, Elsevier.
- Jiang, L., Zeng, Y., Zhou, H., Qu, J. Y., & Yao, S. (2012). Visualizing millisecond chaotic mixing dynamics in microdroplets: A direct comparison of experiment and simulation. *Biomicrofluidics*, 6, 012810 1-12.
- Joensson, H. N., & Andersson-Svahn, H. (2011). Droplet microfluidics - a tool for protein engineering and analysis. *Lab on a Chip*. doi:10.1039/c1lc90102h
- John, V., & Knobloch, P. (2008). On spurious oscillations at layers dimishing (SOLD) methods for convection-diffusion equations: Part II - Analysis for P1 and Q1 finite elements. *Computational Methods in Applied Mechanics and Engineering*, 197, 1997-2014.
- Kashid, M. N., Agar, D. W., & Turek., S. (2007). CFD modelling of mass transfer with and without chemical reaction in the liquid-liquid slug flow microreactor. *Chemical Engineering Science*, 62(18), 5102-5109.

References

- Kashid, M. N., Gerlach, I., Goetz, s., Franzke, J., Acker, J. F., Platte, F., . . . Turek, S. (2005). Internal circulation within the liquid slugs of a liquid-liquid slug-flow capillary microreactor. *Industrial & Engineering Chemistry Research*, *44*, 5003-5010.
- Khodaparast, S., Borhani, N., & Thome, J. R. (2014). Application of micro particle shadow velocimetry uPSV to two-phase flows in microchannels. *International Journal of Multiphase Flow*, *62*, 123-133.
- Kinoshita, H., Kaneda, S., Fujii, T., & Oshima, M. (2006). Three-dimensional measurement and visualization of internal flow of a moving droplet using confocal micro-PIV. *Lab on a Chip*, *7*, 338-346.
- Kirby, B. (2010). *Micro- and Nanoscale Fluid Mechanics: transport in microfluidic devices* (1st ed.). Cambridge: Cambridge University Press.
- Knobloch, P., & Tobiska, L. (2011). On the stability of finite-element discretizations of convection–diffusion–reaction equations. *IMA Journal of Numerical Analysis*, *31*, 147-164.
- Kothe, D. B., & Rider, W. J. (1995). Comments on modeling interfacial flows with volume-of-fluid methods.
- Kreutzer, M. T., Kapteijn, F., Mouijn, J. A., Kleijn, C. R., & Heiszwolf, J. J. (2005). Inertial and interfacial effects on pressure drop of Taylor flow in capillaries. *AIChE Journal*, *51*(9), 2428-2440.
- Kumacheva, E., & Garstecki, P. (2011). *Microfluidic Reactors for polymer Particles*. Chichester: John Wiley and Sons.
- Kuzmin, D. (2010). *A Guide to numerical methods for transport equations*. Retrieved April 09, 2015, from www.mathematik.uni-dortmund.de/~kuzmin/Transport.pdf
- Lafaurie, B., Nardone, C., Scardovelli, R., Zaleski, S., & Zanetti, G. (1994). Modelling merging and fragmentation in multiphase flows with SURFER. *Journal of Computational Physics*, *113*(1), 134-147.

References

- Lei, J., Hill, M., & Glynne-Jones, P. (2014). Numerical simulation of 3D boundary-driven acoustic streaming in microfluidic devices. *Lab on a Chip*, 14(3), 532-541.
- Liu, J., & Nguyen, N. T. (2010). Numerical Simulation of Droplet-Based Microfluidics-A Review. *Micro and Nanosystems*, 2(3), 193-201.
- Malsch, D., Kielpinski, M., Merthan, R., J. Alberta, G. M., Köhler, J., Süße, H., . . . Henkel, T. (2008). μ PIV-Analysis of Taylor flow in micro channels. *Chemical Engineering Journal*, 135S, S166–S172.
- Manz, A., Graber, N., & Widmer, H. (1990). Miniaturized total chemical analysis system: A novel concept for chemical sensing. *Sensors and Actuators B*, 1, 244-248.
- Mashaghi, S., Abbaspourrad, A., A.Weitz, D., & Oijen, A. M. (2016). Droplet microfluidics: A tool for biology, chemistry and nanotechnology. *Trends in Analytical Chemistry*, 82(1), 118-125.
- Mason, L., Ciceri, D., Harvie, D., Perera, J., & Stevens, G. (2013). Modelling of interfacial mass transfer in microfluidic solvent extraction: part I. Heterogenous transport. *Microfluidics and nanofluidics*, 14(1-2), 197-212.
- Mbanjwa, M. B., Land, K. J., & Brady, D. (2018). Production of self-immobilised enzyme microspheres using microfluidics. *Process Biochemistry*, 69, 75-81.
- Meinhart, C. D., Wereley, S. T., & Santiago, J. G. (1999). PIV measurements of a microchannel flow. *Experiments in Fluids*, 27, 414-419.
- Muradoglu, M., & Stone, H. A. (2005). Mixing in a drop moving through a serpentine channel: A computational study. *Physics of Fluids*, 17, 073305 1-9.
- Oberkampf, W. L., & Trucano, T. G. (2002). Verification and validation in computational fluid dynamics. *Progress in Aerospace Sciences*, 38, 209–272.

References

- Olsson, E., & Kreiss, G. (2005). A conservative level set method for two phase flow. *Journal of Computational Physics*, 210, 225-246. doi:10.1016/j.jcp.2005.04.007
- Ong, W., Hua, J., Zhang, B., Teo, T., Zhuo, J., Nguyen, N., . . . Yobas, L. (2007). Experimental and computational analysis of droplet formation in a high-performance flow-focusing geometry. *Sensors and Actuators A: Physical*, 138(1), 203-212.
- Renardy, Y., & Renardy, M. (2002). PROST: A Parabolic Reconstruction of Surface Tension for the Volume-of-Fluid Method. *Journal of Computational Physics*, 183, 400-421.
- Rhee, M., & Burns, M. A. (2008). Drop Mixing in a Microchannel for Lab-on-a-Chip Platforms. *Langmuir*, 24, 590-601.
- Roache, P. J. (1997). Quantification fo uncertainty in Computational Fluid Dynamics. *Annual Reviews in Fluid Mechanics*, 29, 123-60.
- Sackmann, E. K., Fulton, A. L., & Beebe, D. J. (2014). The present and future role of microfluidics in biomedical research. *Nature*, 507, 181-189.
- Sang, L., Hong, Y., & Wang, F. (2009). Investigation of viscosity effect on droplet formation in T-shaped microchannels by numerical and analytical methods. *Microfluidics and Nanofluidics*, 6(5), 621-635.
- Sarrazin, F., Bonometti, T., & Prat, L. (2008). Hydrodynamics structures of droplets engineered in rectangular micro-channels. *Microfluidics and Nanofluidics*, 5, 131-137. doi:10.1007/s10404-007-0233-9
- Sarrazin, F., Loubiere, K., & Prat, L. (2006). Experimental and numerical study of droplet hydrodynamics in microchannels. *AIChE Journal*, 52(12), 4061-4070.
- Sarrazin, F., Prat, L., & Di Miceli, N. (2007). Mixing characterization inside microdroplets engineered on a microcoalescer. *Chemical Engineering Science*, 62, 1042-1048.

References

- Schneider, T., Burnham, D., Van Orden, J., & Chiu, D. (2011). Systematic investigation of droplet generation at T-junctions. *Lab on a Chip*, 11(12), 2055-2059.
- Shahzad, K., Van Aeken, W., Kazemi Kamyab, V., Mottaghi, M., & Kuhn, S. (2017). Numerical investigation of rigid microparticles dynamics: Aggregation and clogging phenomena in microfluidics by discrete element method (DEM) and CFD coupling. *Advanced Materials-TechConnect Briefs*, 3(1), 166-169.
- Song, H., Chen, D. L., & Ismagilov, R. F. (2006). Reactions in droplets in microfluidic channels. *Angewandte Chemie*, 45, 7336-7356.
- Song, H., Tice, J. D., & Ismagilov, R. F. (2003). A microfluidic system for controlling reaction networks in time. *Angewandte Chemie*, 115(7), 791-796.
- Steiner, T., Cupelli, C., Zengerle, R., & Santer, M. (2009). Simulation of advanced microfluidic systems with dissipative particle dynamics. *Microfluidics and Nanofluidics*, 7(3), 307-323.
- Stone, Z. B., & Stone, H. A. (2005). Imaging and quantifying mixing in a model droplet micromixer. *Physics of Fluids*, 17, 063103 1-11.
- Stroock, A. D., Dertinger, S. K., Ajdari, A., Mezic, I., Stone, H. A., & Whitesides, G. M. (2002). Chaotic mixer for microchannels. *Science*, 295, 647-651.
- Sun, C.-l., & Hsiao, T.-h. (2013). Quantitative analysis of microfluidic mixing using microscale schlieren technique. *Microfluidics and Nanofluidics*, 15, 253-265.
- Sussman, M., Smereka, P., & Osher, S. (1994). A level set approach for computing solutions to incompressible two-phase flow. *Journal of Computational Physics*, 114, 146-159.

References

- Taha, T., & Cui, Z. F. (2006a). CFD modelling of slug flow inside square capillaries. *Chemical Engineering Science* 61, 61, 665 – 675.
- Taha, T., & Cui, Z. F. (2006b). CFD modelling of slug flow in vertical tubes. *Chemical Engineering Science*, 61, 676 – 687.
- Talimi, V., Muzychka, Y. S., & Kocabiyik, S. (2012). A review on numerical studies of slug flow hydrodynamics and heat transfer in microtubes and microchannels. *International Journal of Multiphase Flow*, 39, 88-104.
- Tanthapanichakoon, W., Aoki, N., Matsuyama, K., & Mae, K. (2006a). Design of mixing in microfluidic liquid slugs based on a new dimensionless number for precise reaction and mixing operations. *chemical Engineering Science*, 61, 4220-4232.
- Tanthapanichakoon, W., Matsuyama, K., Aoki, N., & Mae, K. (2006b). Design of microfluidic slug mixing based on the correlation between a dimensionless mixing rate and a modified Peclet number. *Chemical Engineering Science*, 61(1), 7386 – 7392.
- Taylor, G. I. (1953). Dispersion of soluble matter in solvent flowing slowly through a tube. *Proceedings of the Royal Society of London A: Mathematical, Physical and Engineering Sciences*, 219(1137), 186-203.
- Taylor, G. I. (1961). Deposition of a viscous fluid on the wall of a tube. *Journal of Fluid Mechanics*, 10, 161-165.
- Teh, S.-Y., Lin, R., Hung, L.-H., & Lee, A. P. (2008). Droplet microfluidics. *Lab on a Chip*, 8, 198-220.
- Tice, J. D., Lyon, A. D., & Ismagilov, R. F. (2004). Effects of viscosity on droplet formation and mixing in microfluidic channels. *Analytica Chimica Acta*, 73–77, 507.
- Tice, J., Song, H., Lyon, A., & Ismagilov, R. (2003). Formation of droplets and mixing in multiphase microfluidics at low values of the Reynolds and the capillary numbers. *Langmuir*, 19(22), 9127-9133.

References

- Tryggvason, G., Bunner, B., & Esmaeeli, A. (2001). A front-tracking method for the computations of multiphase flow. *Journal of Computational Physics*, 169(2), 708-759.
- Tung, K. -Y., Li, C. -C., & Yang, J. -T. (2009). Mixing and hydrodynamic analysis of a droplet in a planar serpentine micromixer. *microfluidics and Nanofluidics*, 7, 545-557.
- Van der Graaf, S., Nisisako, T., Schroen, C., Van Der Sman, R., & Boom, R. (2006). Lattice Boltzmann simulations of droplet formation in a T-shaped microchannel. *Langmuir*, 22(9), 4144-4152.
- Versteeg, H., & Malalasekera, W. (1995). *Computational fluid dynamics: the finite volume method*. Harlow, England: Longman Scientific & Technical.
- Vyawahare, S., Griffiths, A. D., & Merten, C. A. (2010). Miniaturization and parallelisation of biological and chemical assays in microfluidic devices. *Chemistry & Biology*, 17, 1052-1065.
- Walker, E. D. (2016). *Numerical studies of liquid-liquid segmented flows in square microchannels using a front-tracking algorithm*. PhD Thesis: Louisiana State University.
- Wang, Y., & Dimitrakopoulos, P. (2012). Low-Reynolds-number droplet motion in a square microfluidic channel. *Theoretical and Computational Fluid Dynamics*, 26(1), 361-379.
- Wautelet, M. (2001). Scaling laws in the macro-, micro- and nanoworlds. *European Journal of Physics*, 22, 601-611.
- White, F. M. (2006). *Viscous fluid flow* (3rd ed.). Boston: McGraw Hill.
- Whitesides, G. M. (2006). The origins and the future of microfluidics. *Nature*, 442, 368-373.
- Wilkes, J. O. (2006). *Fluid mechanics for chemical engineers, with microfluidics and CFD* (2nd ed.). Cape Town: Prentice Hall PTR.

References

- Williams, S. J., Park, C., & Wereley, S. T. (2010). Advances and applications on microfluidic velocimetry techniques. *Microfluidics and Nanofluidics*, 8, 709-726.
- Wörner, M. (2012). Numerical modeling of multiphase flows in microfluidics and micro process engineering: a review of methods and applications. *Microfluidics and Nanofluidics*, 12, 841-886.
- Yang, C.-G., Xu, Z.-R., & Wang, J.-H. (2010). Manipulation of droplets in microfluidic systems. *Trends in Analytical Chemistry*, 29(2), 141-157.
- Youngs, D. L. (1982). Time-dependent multi-material flow with large fluid distortion. *Numerical methods for fluid dynamics*, 24 , 273-285.
- Zahedi, S., Kronbichler, M., & Kreiss, G. (2012). Spurious currents in finite element based level set methods. *International Journal for Numerical Methods in Fluids*, 69, 1433–1456.
- Zhang, J. (2011). Lattice Boltzmann method for microfluidics: models and applications. *Microfluidics and Nanofluidics*, 10(1), 1-28.
- Zienkiewicz, O. C., & Taylor, R. L. (2000). *The Finite Element Method - Fluid Dynamics* (5th ed., Vol. 3). Oxford: Butterworth-Heinemann.
- Zienkiewicz, O. C., Taylor, R. L., & Zhu, J. Z. (2005). *The Finite Element Method - Its Basis & Fundamentals* (6th ed.). London: Butterworth Heinemann.
- Zimmerman, W. B. (2006). *Multiphysics modeling with finite element methods* (Vols. 18 of Series on stability, vibration and control systems). London: World Scientific Publishing Company.

Appendix A: Velocity profiles in rectangular microfluidic channels

Planar microfluidic devices fabricated using soft lithography techniques, generally exhibit microchannels with rectangular cross-sections. The pressure differential is the typical mechanism for flow actuation. The velocity profile of the flow is influenced by the aspect ratio, which is described by as the ratio of the channel width (w) to the channel height (h). Figure C.1 illustrates the relationship between the flow and the pressure differential in a microchannel with a rectangular cross-section. The velocity profile in the direction on the flow is given by (Bruus, 2008)

$$u_x(y, z) = \frac{4h^2\Delta p}{\pi^3\mu L} \sum_{n, odd}^{\infty} \frac{1}{n^3} \left[1 - \frac{\cosh(n\pi\frac{y}{h})}{\cosh(n\pi\frac{w}{2h})} \right] \sin(n\pi\frac{z}{h}) \quad (A1)$$

Equation is obtained from the solution of the Stokes equation has a parabolic profile, as illustrated in Figure A1. The volumetric flow rate can be approximated from

$$Q \approx \frac{h^3w\Delta p}{12\mu L} \left[1 - 0.63 \frac{h}{w} \right], \text{ for } w > h \quad (A2)$$

For an aspect ratio of 1, Equation has an 87% accuracy, which improves as $w \gg h$ (Bruus, 2008).

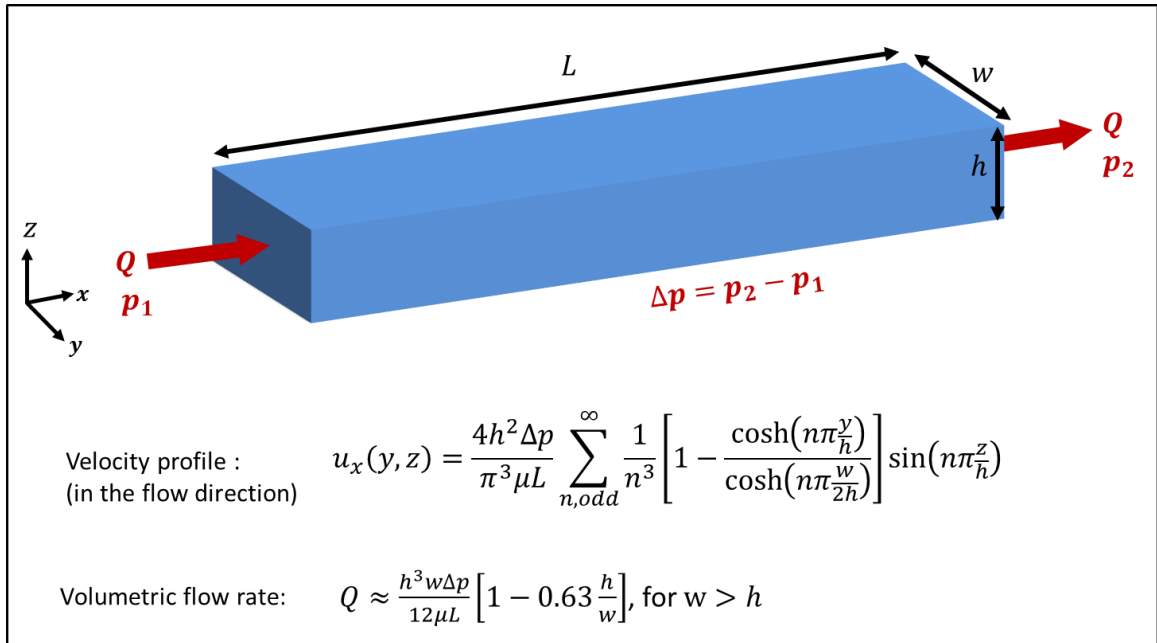


Figure A1 Pressure-driven flow in a rectangular microchannel.

Figure A.1 shows the velocity profiles at different aspects ratios for the same volumetric flowrate. The CFD models for the velocity profiles in Figure A2.

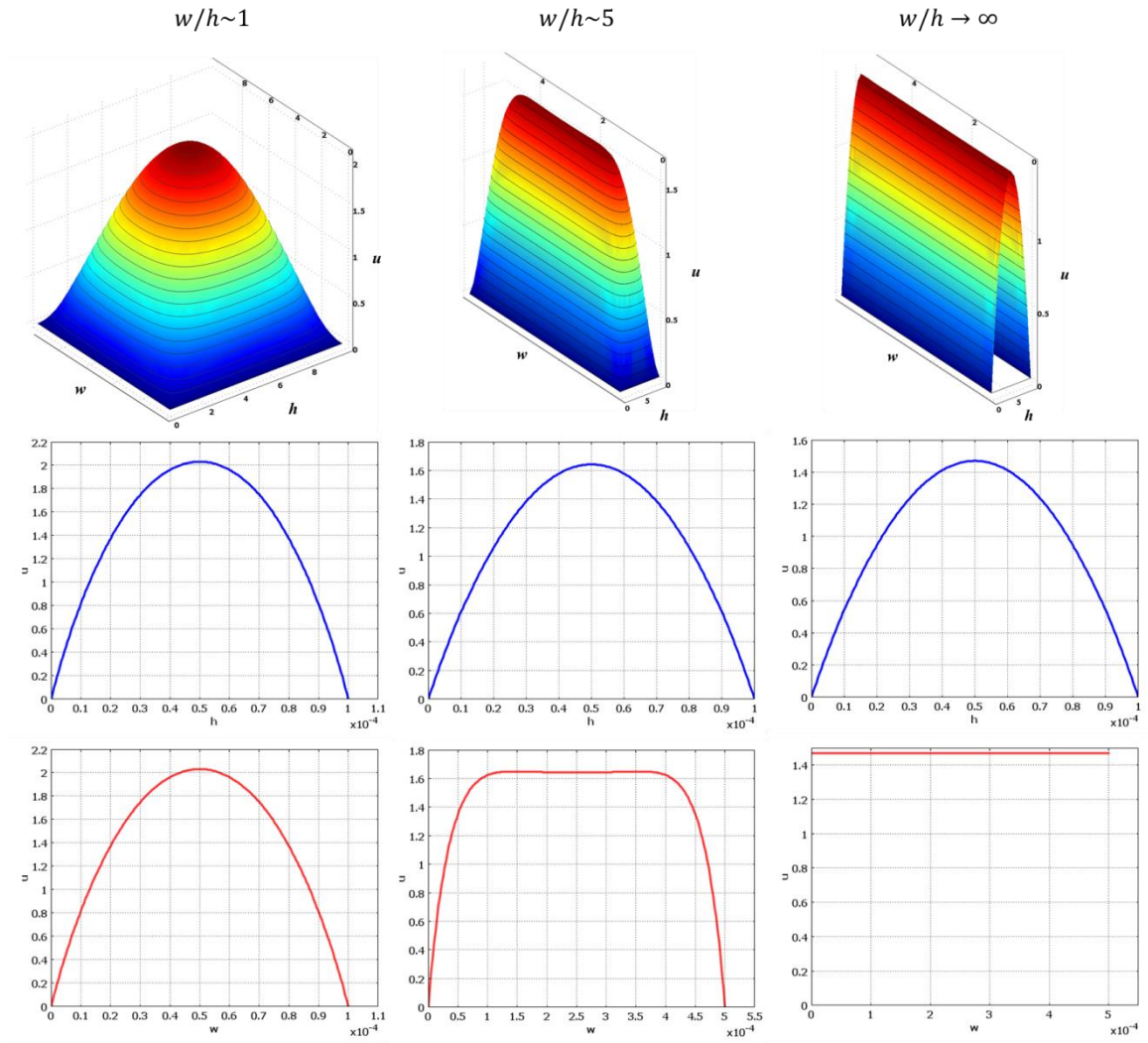
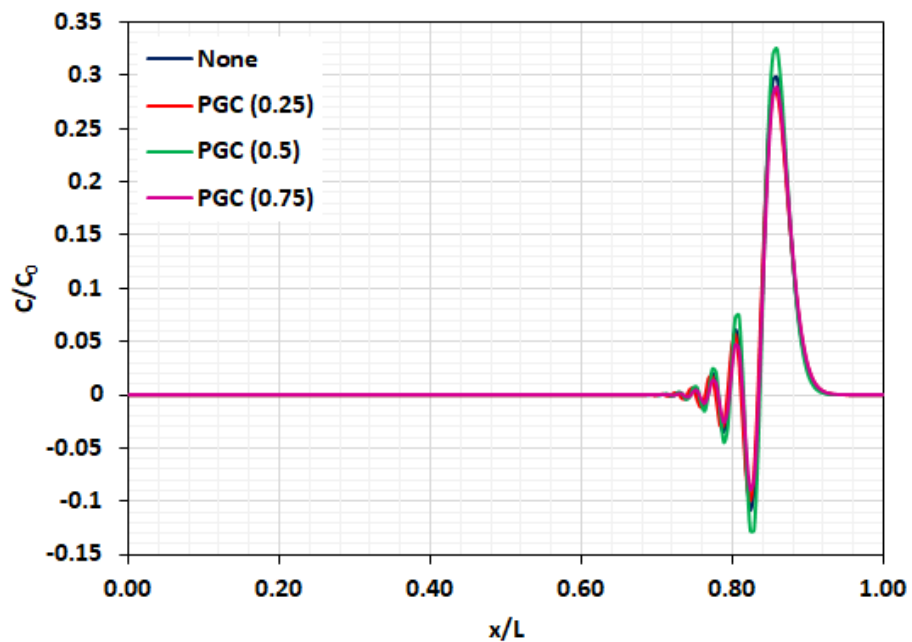
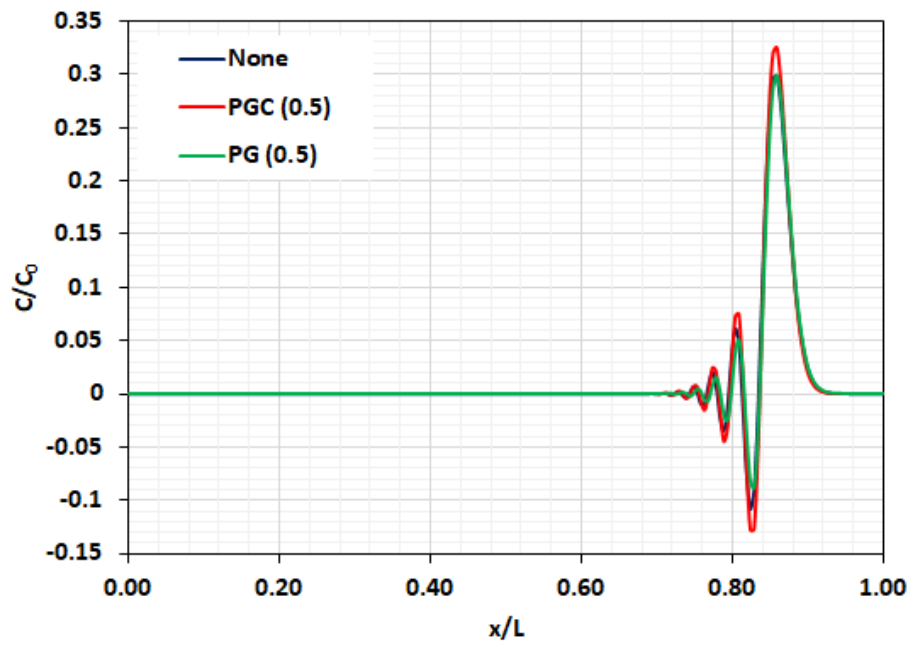
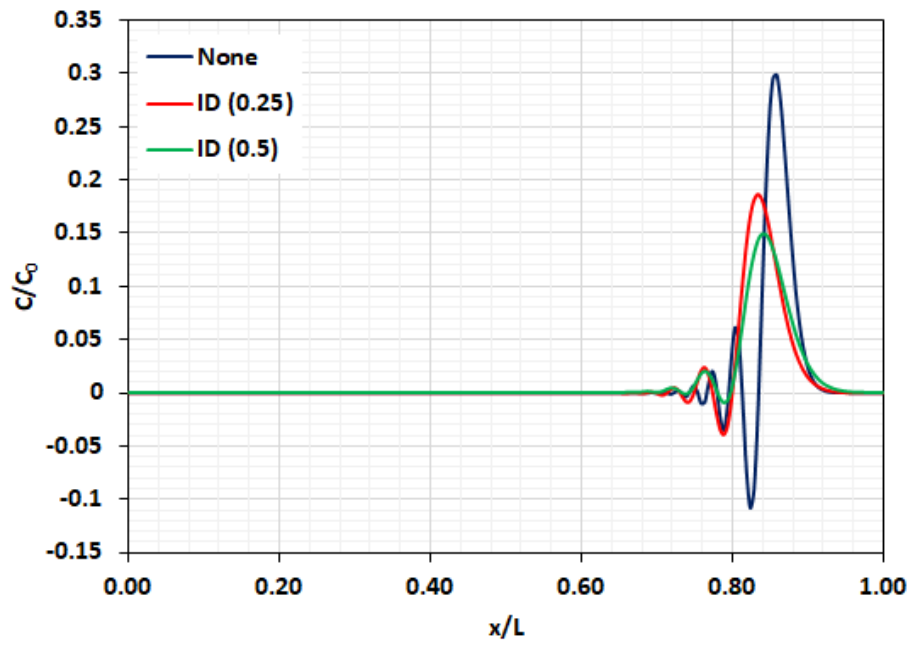


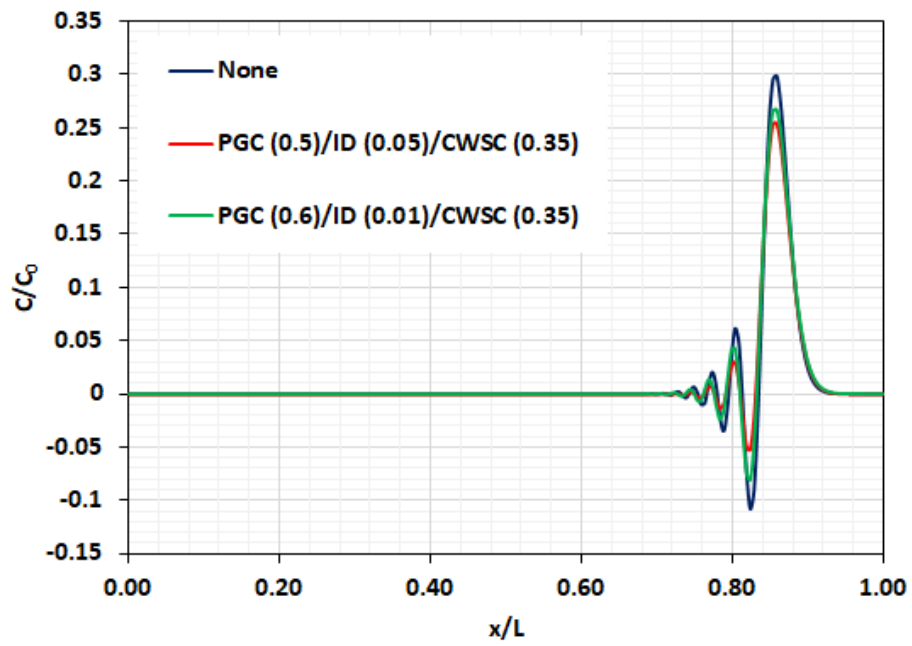
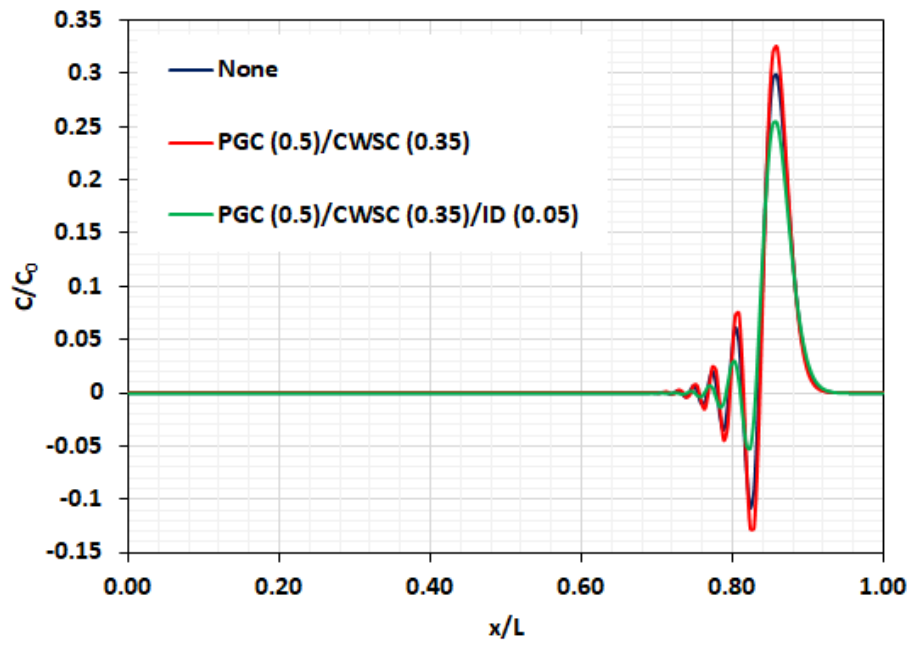
Figure A.2 FEM-modelled velocity profiles in rectangular microchannels of varying aspect ratios.

Appendix B: Evaluation of artificial diffusion parameters

This section shows plots of normalised concentration profiles obtained from various artificial diffusion parameters for the case of axial dispersion at $Pe = 500$. The artificial diffusion methods that were iteratively tested are Petrov-Galerkin (PG), Petrov-Galerkin compensated (PGC), isotropic (ID), anisotropic (AI) and crosswind shock capturing (CWSC). The respective tuning parameters are shown in brackets in each of the plots.







Appendix C: Modified Peclet numbers as function of the capillary number for different plug sizes

Ca	h		2h		5h	
	L_d/U_{sv}	Pe_m	L_d/U_{sv}	Pe_m	L_d/U_{sv}	Pe_m
0.013	1.08	0.09	2.17	0.05	5.42	0.02
0.022	0.64	0.16	1.29	0.08	3.22	0.03
0.046	0.31	0.32	0.63	0.16	1.57	0.06
0.075	0.19	0.52	0.38	0.26	0.96	0.10
0.10	0.14	0.70	0.29	0.35	0.72	0.14
0.15	0.09	1.06	0.19	0.53	0.47	0.21
0.21	0.07	1.50	0.13	0.75	0.33	0.30

Appendix D: A basic benchmarking of the computational cost between two-phase MFR and the two-phase FFR approaches

The aim of the was to demonstrate the advantage of the two-phase moving-frame-of-reference (MFR) over the conventional two-phase fixed-frame-of-reference (FFR) modelling approach. Two forms of benchmarks were evaluated: (1) The first determined the CPU time taken in each of approaches to obtain a transient solution of the droplet transport across the microchannel. (2) The advantage of the two-phase MFR in modelling of a moving droplet due to its fixed computational domain is illustrated.

The problem of mixing in a droplet travelling in a straight microchannel is the benchmark case for the study. The numerical tests were conducted using COMSOL Mutliphysics™ (Version 3.5a) which is based on the finite element numerical (FEM). The conservative level set methods numerical scheme was implemented for modelling the interface coupled to the two-phase flow. The various parameters used are given the various tables labelled from D1 to D3.

Table D1: Fluid properties

Parameter	Value
Density, continuous phase (ρ_1)	1000 kg/m ³
viscosity, continuous phase (μ_1)	0.002 Pa·s
Density, droplet phase (ρ_2)	1000 kg/m ³
viscosity, droplet phase (μ_2)	0.002 Pa·s
Interfacial tension (σ)	14 mN/m

Table D2: Flow parameters

Parameter	Value
Capillary number (Ca)	0.21
Viscosity ratio (λ)	1
Superficial velocity (U_{sv})	1.44 m/s
Microchannel width (h)	100 μ m

Table D3: Computer hardware & Operating System

Parameter	Details
Computer type	Desktop
Processor	Intel® Core™ i7-7700 CPU @ 3.6GHz
Number of CPUs	1
Number of cores	4 (Quadcore)
Number of threads	8
Random access memory (RAM)	32 GB (4x 8G DDR4, 2400 MHz)
Operating System (OS)	Windows 10
System type	64-bit operating system, x64-based processor

Benchmark Case 1: Comparison of performance between Two-phase MFR and Two-phase FFR in obtaining a transient solution of a moving droplet.

In this benchmark case, the performances of both the performance-phase MFR and two-phase in obtaining a transient flow solution at a given time.

For simplicity, the comparison was limited to CPU time as the performance indicator for the solutions obtained utilising the same or similar computer resources (hardware & operating system), with all else being equal. There are more rigorous techniques that can be used, the simple case is considered to suffice.

For both cases, the model geometry, the mesh properties and solver parameters are the kept the same. The differences between the two cases lies only in boundary conditions.

Table D4: Model geometry properties:

Parameter	Value
Space dimension	2D
Microchannel width (h)	100 μm
Microchannel length (L)	400 μm
Initial droplet/plug width (w_0)	$0.8h$
Initial droplet/plug width (L_0)	$2h$
Distance of droplet tail to channel back end (X_t)	h

Table D5: Mesh properties

Parameter	Value
Mesh type	Triangular
Maximum element size (domain)	10^{-6} m
Maximum element size (boundary)	$5 \cdot 10^{-7}$ m
No of mesh elements	175 918
No of mesh points	88 869
Degrees of freedom (Flow + level set equations)	1 149 835

Table D6: Boundary Conditions

Boundary	Two-phase MFR	Two-phase FFR
Back edge boundary	Laminar outflow [$P = 0; L_{exit} = 10^{-2} \text{ m}$]	Laminar inflow [$U = 1.44 \text{ m/s}$]
Front edge boundary	Laminar inflow [$U = 0.134 \text{ m/s}$]	Laminar outflow [$P = 0; L_{exit} = 10^{-2} \text{ m}$]
Wall boundaries	Moving wall [$u_w = -0.858 \text{ m/s}$]	Wetted wall [$\theta = 120^\circ$]
Internal boundaries	Initial fluid interface	Initial fluid interface

Table D7: Flow solution parameters

Parameter	Value
Solution mode	Transient
Linear solver	PARDISO
Time-dependent solver	Generalised alpha
Maximum time step (Δt_{max})	$5 \cdot 10^{-7} \text{ s}$

In the case of the two-phase FFR, the flow velocity was increased using a time-based Heaviside ramp function, going from zero to maximum in $2 \cdot 10^{-5} \text{ s}$.

Table D8: Benchmark 1 results

Parameter	Two-phase MFR	Two-phase FFR
Solution (fluid flow) time	$4.3 \cdot 10^{-4}$ s	$1.4 \cdot 10^{-4}$
Clock (CPU) time (to solution)	4587 s	7842 s
Total core hours	5.1 hours	8.7 hours
Average time per time step at Δt_{max}	5.33 s per core	28.0 s per core

The results demonstrate that in the current test the two-phase MFR performed better than the two-phase FFR. The convection of the interface across the domain with moving droplet, is heavier computationally, compared to the MFR case which at quasi steady state there is little interface movement. The results, do not take into account iterative tests to determine the quasi steady state parameters; These were pre-determined.

Benchmark Case 2: Illustration of the computational advantage of two-phase MFR by maintaining a fixed computational domain for mixing in a moving droplet.

Consider a case where mixing takes place within a droplet travelling in a straight microchannel with a certain width. The time and the distance travelled by the droplet are amongst the most important factors which influence the extent of mixing. In the case where the mixing within the droplet is fast, the time and distance required to achieve complete mixing are short. However, when the rate of mixing is slow, the time and distance required to achieve complete mixing are relatively long. From the point of view of FFR modelling the computational domain increases with the increased travel time and distance of the droplet. The advantage of the two-phase MFR is that under the steady state condition there is no requirement to change the size of the computational domain to cater for increased mixing and distance travelled by the droplet.

Based on the two-phase MFR (quasi steady state) solution in the previous benchmark case, a droplet mixing solution was obtained utilising the same computational domain with 175 198 mesh elements. The speed of the droplet at quasi steady state was 1.77 m/s. The mixing index of 0.9 was achieved in a mixing time of 11.5 ms.

However, in the case of two-phase FFR, the, increased mixing time and travelling requires a proportional (based on droplet speed) increase in the microchannel length, hence a bigger domain. Table D9 shows the relation between the mixing time, microchannel and corresponding computational cost proxies (number of mesh elements and degrees of freedom (DOF) based on the LS two-phase equations). The case illustrated is based on the changing microchannel length but keep the channel width constant.

Table D9: Relation between the mixing time, mixing length, number of mesh elements and degrees of freedom (DOF) for two-phase FFR.

Mixing time [ms]	Microchannel length [mm]	No of mesh elements	DOF
0.23	0.4	175 918	1 149 835
0.56	0.4	517 038	3 403 606
0.85	1	607 658	4 316 000
2.82	1.5	2 200 042	14 371 041
5.65	5	4 396 908	28 720 670
11.30	10	8 792 936	57 434 852

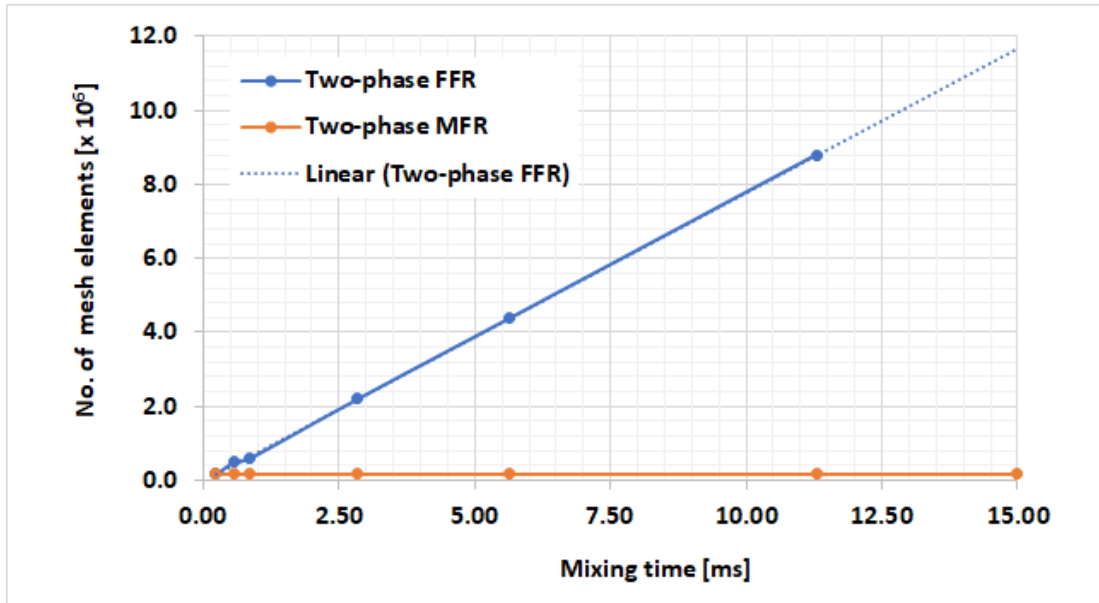


Figure D1: Illustration of the increase in number of computational mesh elements with increased mixing time (and computational domain) for a droplet travelling at 1.77 m/s.

"It always seems impossible until it's done." -- Nelson R. Mandela